An Investigation of a Strongly Driven Multi-Level Atomic System

by

Peter John Manson

A thesis submitted for the degree of Doctor of Philosophy of the Australian National University.

December 1987

Statement of authorship

The contents of this thesis, except where indicated by reference, are entirely my own work.

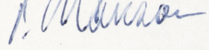

Acknowledgements

I would like to thank my supervisors, Dr. John Sandeman and Dr. Hans Bachor, for their guidance and encouragement during the course of this work.

I would also like to thank Dr. Sandeman, Dr. Carl Dahlstrom and Dr. Peter Fisk for their careful proof reading and criticism of this thesis. Thanks also to Dr. Don Bone for his painstaking work in type setting many of the equations and to my sister, Hilary, for typing the reference list.

Abstract

The non-linear interaction between two laser fields and a multi-level, Doppler broadened system was investigated, using modified saturated absorption and polarisation spectroscopy on the D_1 transition of sodium.

The modifications to standard experiments involved using a co-propagating geometry for the two lasers and a fixed pump laser frequency during the scans. Profiles were recorded as the probe laser frequency was scanned through resonance with the transition for a number of pump laser frequencies in the vicinity of the same transition. Sets of profiles were recorded for various combinations of laser polarisation and analyser orientation (in the polarisation spectroscopy experiments).

Simple theoretical descriptions of Doppler broadening and optical pumping in the profiles were given. However, a more sophisticated treatment based on a solution of the Liouville equation using an irreducible tensor basis in Liouville space was also necessary. Doppler broadening was treated using a Fourier transform technique. The signal was derived from the density matrix using an operator formalism for the analyser.

Good agreement between the theoretical and experimental profiles was demonstrated. Based on this agreement, it is possible to conclude that a multi-level Doppler broadened

atomic system can be modelled reasonably accurately, although the Doppler broadening calculation requires large amounts of computer time and storage.

Table of Contents

List of figures

List of Tables

Chapter 3. Experimental Results

Chapter 1. Introduction

The interaction of a near-resonant light field with an atomic system has been extensively studied both experimentally and theoretically. More recently, the availability of intense, narrow band dye lasers has stimulated interest in the non-linear interaction between light and atoms. Examples of such non-linear interaction include the A.C. Stark effect, power broadening and saturated absorption spectroscopy. The fundamental processes that cause these and other effects are now well understood. Verification of this understanding has come from comparison of theoretical calculations with corresponding experimental results.

In order to compare theoretical predictions with experimental results in detail, most workers have been obliged to take special steps in the experiment to allow the theory to be simplified. Theoretical treatments have typically been restricted to the simplest atomic systems such as a two- or three-state stationary atom. These systems allow the most important physical processes to be clearly described. Some examples of the steps taken in earlier experimental investigations include preparation of the atoms in an atomic beam to limit atomic motion effects, hyperfine optical pumping of sodium before the interaction to produce a two state atom, and mixing of the hyperfine levels of sodium (using a high buffer gas pressure or strong magnetic field) to produce an effective j=1/2 to 1/2 transition.

Now that the basic processes involved in the non-linear interaction have been understood as a result of pioneering investigations, it is worth considering whether the same degree of understanding can be achieved for the more common experiment which does not employ such careful precautions. Is it possible, for example, accurately to model a multi-level atom in a Doppler broadened sample interacting with a strong pump field? The work described in this thesis is an attempt to produce a theoretical treatment of an experiment in a more complicated atomic system. The theoretical model and the experiment are presented and the results compared.

1.1 Summary of this work

Saturated absorption and polarisation spectroscopy experiments in a vapour of sodium were chosen as examples of a typical experimental system. These techniques are described briefly in Chapter 2. Sodium is frequently used to investigate non-linear interactions because it is readily evaporated to form an atomic beam or vapour and the D lines are easily accessible with stable laser dyes. However, it is far from the simple two- or three-state atom usually assumed in theoretical calculations. Hyperfine structure and Zeeman degeneracy mean that the simpler of the two D lines involves a total of sixteen states. Figure 4.1 shows the structure of the D_1 transition used in this work. Atomic motion adds an additional complication to the model.

Three modifications to the usual saturated absorption or polarisation spectroscopy experiments were made. Firstly, the intensity of the pump beam was not kept to a minimum. This ensured that non-linear interaction with the pump field was important. Secondly, different lasers were used for the pump and probe beams, so the frequency of the pump beam could be kept fixed during a probe laser frequency scan. This allowed a more thorough examination of the detuning dependence of the interaction. Finally, a co-propagating geometry was used since it is necessary for observation of the Autler-Townes effect in this sort of Doppler broadened system.

Before proceeding to the sophisticated theoretical calculations, the experimental results were examined using simple theories for the Doppler effect and optical pumping. Although restricted in accuracy, the optical pumping model allows a clear understanding of the general features of the profiles. The treatment of the Doppler effect uses a straight forward graphical technique to identify the origins of features in the Doppler broadened profiles.

A theoretical model that described the system as well as possible was also developed. The standard description using the density matrix was extended to include the multiple levels (and degenerate Zeeman sub-levels) of the sodium transition. The vector nature of the fields was included in the calculation to allow any combination of pump and probe polarisations and analyser orientation to be modelled.

Because of the extended atomic system used, it was necessary to use a computer to calculate the results. Doppler broadening was included using a Fourier transform technique to perform the necessary convolution integrals numerically.

The validity of the model can be judged from the degree of agreement between theoretical and experimental profiles for various combinations of polarisations and pump intensities.

1.2 Review of previous work

There is a substantial volume of previous work on the interaction of a strong laser field with an atomic system. In summarising this literature, it is useful to separate the contributions into those that consider the dynamic Stark effect and those that treat saturation effects with regard to the operation of gas lasers and high resolution spectroscopy. The latter category is more relevant to the experiments performed here, but the A.C. Stark effect can also be important. Although the two categories are related, they will be summarised separately, while other aspects of non-linear interaction, such as four wave mixing and bistability, will not be included because they are not related to the present work. At the end of this section, earlier work treating extended atomic level systems will be summarised.

Autler and Townes (1955) first observed splitting of transitions in the microwave region induced by strong coherent radiation. In the optical and infra-red range,

there has been interest in the spectrum of resonance fluorescence from a strongly driven system, as well as the direct optical analogue of the Autler-Townes experiment.

A number of theoretical calculations predicted a three-peaked spectrum in resonance fluorescence from a strongly driven two level atom (Newstein 1968, Mollow 1969, 1970 and 1972a, Stroud 1971, Hassan and Bullough 1975, Smithers and Freedhoff 1975, Carmichael and Walls 1976, Kimble and Mandel 1976, Cohen-Tannoudji 1975, Cohen-Tannoudji and Reynaud 1977a). If the driving laser is exactly on resonance, the separation of the two sidebands from the central peak at the laser frequency is equal to the Rabi frequency.

The Rabi frequency, β, is given, in angular frequency units, by

$$\beta = (\underset{\sim}{\mu}.\underset{\sim}{E})/\hbar$$

where the amplitude of the incident electric field is $\underset{\sim}{E}$ and $\underset{\sim}{\mu}$ is the electric dipole moment of the transition. The Rabi frequency therefore characterises the strength of the interaction through the strengths of both the field and the transition.

Early experimental work on the dynamic Stark effect in sodium confirmed the three-peak structure of the spectrum (Schuda et al 1974, Walther 1975, Wu et al 1975). However, detailed comparison with the theoretical profiles was not

possible due to experimental limitations such as the presence of other hyperfine levels and the non-uniformity of the laser beams. Hartig et al (1976) and Grove et al (1977) obtained better agreement by using circularly polarised light and by optically pumping the population into a single Zeeman sub-level before the interaction region.

An alternative way of observing the influence of a strong laser on an atom is to use a second, weak laser to probe the interaction. Measurements can be made of the total fluorescence intensity or the absorption of the probe laser as it is scanned through resonance with a third level. The two-laser, three-level system was treated theoretically by Mollow 1972a, Feneuille and Schweighofer 1975, and Whitley and Stroud 1976. For the case of the strong beam on resonance, a symmetric doublet with spacing equal to the Rabi frequency (the Autler-Townes doublet) is expected.

The Autler-Townes doublet was observed experimentally using atomic beams (Picque and Pinard 1976, Gray and Stroud 1978, Delsart et al 1981). It was also found theoretically (Feneuille and Schweighofer 1975, Delsart and Keller 1978a) that the doublet could be observed in a Doppler broadened medium if certain conditions on the frequencies of pump and probe fields were met. Several such experiments were carried out (Schabert et al 1975a, 1975b, Cahuzac and Vetter 1976, Delsart and Keller 1976, 1978a). Although the effects were observed, very little detailed comparison with theoretical profiles was presented due to limits on both types of

experiment.

Alternatively, the absorption of the probe in the vicinity of the strongly driven transition may be measured. The absorption spectrum of such a two-laser, two-level system was predicted to have features symmetrically placed about the frequency of the driving field (Mollow 1972b, Cohen-Tannoudji and Reynaud 1977a, Agarwal 1979). At certain frequencies the probe laser is amplified by transfer of energy from the pump beam. Using a sodium atomic beam prepared as a two-level system by optical pumping, Wu et al (1977) were able to demonstrate good agreement with this theory.

Work included in the second category started with the invention of the gas laser. There was substantial interest in the interaction of strong light waves with Doppler broadened media, with application to the operation of lasers (e.g. Dienes 1968a, 1968b, Stenholm and Lamb 1969, Feldman and Feld 1970, Hansch and Toschek 1970). Similar theoretical techniques were later applied to saturated absorption and polarisation spectroscopy (Schlossberg and Javan 1966, Feld and Javan 1969, Baklanov and Chebotaev 1971, 1972, Holt 1972, Skribanowitz et al 1972, Haroche and Hartmann 1972, Shirley 1973, Borde et al 1976, Sargent et al 1976a, 1976b, Kaftandjian et al 1979) which are of greater interest to this work.

Although there have been many publications on the use of saturated absorption and polarisation spectroscopy as techniques in high resolution spectroscopy, investigations of the fundamental processes are of more interest here. Sargent (1976) considered the influence of the polarisations of pump and probe beams on saturated absorption profiles and early papers on polarisation spectroscopy (Wieman and Hansch 1976, Delsart and Keller 1977, 1978b, Keller and Delsart 1977, Stert and Fischer 1978) gave basic treatments of the process in terms of the induced refractive indices and absorption coefficients for different polarisation components of the probe beam.

Early treatments generally considered only the saturation of the two levels involved in the transition. However it was later realised that Zeeman coherences (Colomb and Dumont 1977, Rinneberg et al 1980) and redistribution of population between lower levels (Anderson et al 1978) were important in saturated absorption. The importance of optical pumping in saturated absorption and polarisation spectroscopy was emphasised by the introduction of velocity selective optical pumping (Pinard et al 1979, Aminoff et al 1983, Nakayama 1984a) which gave sub-Doppler resolution with pump laser powers well below saturation levels.

Series and co-workers (Gawlik and Series 1979, Nakayama et al 1980, Nakayama 1981a, 1981b, 1984b, 1985) pointed out the importance of optical pumping in polarisation spectroscopy of alkali atoms and Nakayama (1981) was able to

achieve good agreement between polarisation spectroscopy profiles of the D_1 line of sodium and a theory based on a single cycle of optical pumping. Similar conclusions were drawn by Murnick et al (1979) and Pappas et al (1980) regarding saturated absorption in barium.

Optical pumping is possible in atomic systems that are more complicated than the simple two- or three-state system usually considered. There have been a number of treatments of the strong interaction of light with atoms that have included all relevant states (Zeeman sub-levels or hyperfine structure) in the calculation. These treatments are of more direct relevance to the work presented in this thesis. Cohen-Tannoudji and Reynaud (1977b) and Cooper et al (1980) considered the spectrum of resonance fluorescence from a strongly driven atom.

Delsart and Keller (1980) considered the optical Autler-Townes effect in a three-level ladder system with Zeeman degeneracy and obtained reasonable agreement between an experiment in neon gas and the theory. Feuillade and Berman (1984) gave a detailed account of a solution of the equation of motion for the density matrix of a three-level system with Zeeman degenerate sub-levels. In addition to optical pumping effects, these systems have several Rabi frequencies because of the differing dipole matrix elements between sub-levels. This means that the two peaks of the Autler-Townes doublet are replaced by several pairs. The number of peaks depends on the polarisations of the beams and the angular momentum

quantum numbers of the levels.

The work described in this thesis follows on from an investigation of the dynamic Stark effect in a three-level system in barium carried out earlier (Fisk 1985, Fisk et al 1986a, 1986b, 1986c). The barium level system used was simpler than that of sodium and although the same basic theoretical technique was employed in this work, it was extended to account for the four levels that make up the hyperfine structure of the D_1 transition and for the Zeeman structure of each. In addition, since the experiments were performed in a vapour cell, the Doppler effect was included in the model.

1.3 Structure of this thesis

The experimental side of the investigation is presented in Chapters 2 and 3. Chapter 2 describes the experimental apparatus, referring to Appendix A for some details. This chapter also describes some features of the experiment that were relevant to the comparison with theory. The experimental results are presented and discussed in terms of the Doppler broadening and optical pumping theories in Chapter 3.

The theoretical side is presented in Chapters 4 and 5. Chapter 4 describes the solution of the Liouville equation and its application to the atomic system used in the experiment. After interpreting some parts of the theoretical solution, comparisons of the theoretical and experimental

results are presented in Chapter 5. Finally, the work is summarised in Chapter 6.

Chapter 2. The Experiment

Polarisation spectroscopy and saturated absorption were chosen for the experimental investigation of the non-linear interaction between laser fields and atoms in this work. In these standard techniques, a Doppler-broadened medium is pumped with a saturating beam, and the effect on the intensity (saturated absorption) or polarisation (polarisation spectroscopy) of a weak, counter-propagating probe beam of the same frequency is measured. By modulating the intensity of the pump laser and detecting the signal with a lock-in amplifier, sub-Doppler resolution may be achieved.

However, as mentioned in Chapter 1, there were some significant differences from standard polarisation or saturated absorption spectroscopy experiments. Firstly, the pump beam intensity was not restricted to avoid power broadening. Secondly, the pump and probe beams were produced by different lasers and the pump beam frequency was fixed during scans of the probe frequency. Thus, although both lasers were tuned in the vicinity of the same transition, the two frequencies were not necessarily equal as they are in the standard techniques. In addition, the two laser beams were arranged in a co-propagating geometry.

This chapter describes the experimental work. It begins with a description of the experimental apparatus and the signals recorded. Section 2.2 indicates some important characteristics and difficulties of the experiment which are

relevant to a meaningful comparison of the results with theory.

2.1 Description of the experiment

In order to compare theory and experiment in detail it is necessary to design an experiment where the environment for the atoms is well known and controlled, with no interaction processes that are external to the model. Similarly, the states of the radiation fields interacting with the atoms must be well known and controlled and the detection process must be linear. These principles were applied as much as possible in the design of the experiment.

Figure 2.1 is a schematic diagram of the experimental apparatus used in this work. It consisted essentially of a sodium vapour cell, the two laser beams with polarising and focussing optics, and a photomultiplier for intensity measurement.

The low density sodium vapour (approximately 10^{-6} Torr) was contained in a heated vacuum cell, without buffer gas and with a background pressure of 10^{-6} Torr. Appendix A describes the cell in greater detail. A set of Helmholtz coils was used to reduce stray magnetic fields in the cell to less than 10 mG.

The optical arrangement was set up to produce a strong pump beam and a weak probe beam, propagating in the cell as close to parallel as possible and both in carefully

controlled polarisation states. The pump powers used in the experiments ranged from 0.07 mW to 66 mW.

The beams were focussed into the cell, and crossed in the centre. Focal lengths and positions of the focussing lenses were chosen to make the pump beam waist larger than that of the probe. Both waist sizes were measured using a method based on the technique outlined by Khosrofian and Garetz (1983). The measured waist diameters were:- pump beam 860 μm and probe beam 220 μm. These values correspond to the points where the intensity is 1/e of the central intensity. The corresponding values of the w_0 parameter defined by Kogelnik and Li (1966) are 610 μm and 150 μm respectively. For this pump beam size, the Rabi frequencies (averaged over the Gaussian beam profile) used in the experiment ranged from 10 MHz to 300 MHz.

For comparisons with the theoretical calculations to be valid, the probe field must be weak enough for the interaction with the atoms to be linear in the probe intensity. This was checked experimentally by observing the variation of saturated absorption profiles with probe intensity. For each of a series of decreasing pump powers, the probe intensity was reduced until the linewidth of the profile remained constant. The reduction in both laser powers was continued until noise started to mask the signal. In this manner, it was possible to achieve linewidths of approximately 15 MHz.

This compares favourably with the natural width of 10 MHz, with the difference assumed to be due to residual power broadening by the pump laser. Hence it can be assumed that the probe was weak enough to allow the atomic interaction with the probe field to be linear. This means that the probe Rabi frequency was less than the spontaneous emission rate of the upper level.

The beams were either linearly polarised (using high extinction ratio crystal polarisers) or circularly polarised (using quarter-wave plates after the polarisers) before entering the cell. After interacting with the strongly pumped vapour, the probe beam was passed through an analyser (another high extinction ratio polariser) and then to a photomultiplier to measure the transmitted intensity. The analyser was not used in the saturated absorption experiments.

The pump laser was tuned near resonance with the D_1 line (589.6 nm) of sodium, and the probe laser was scanned through resonance with the same transition. The D_1 transition was chosen because the excited state hyperfine structure is simpler than that of the D_2 line, making the theoretical calculations simpler. As in standard saturated absorption and polarisation spectroscopy measurements, the pump laser was chopped with a mechanical chopper and the signal was processed by a phase sensitive detector. The scans were repeated for a number of different pump frequencies in the vicinity of the transition, and sets of scans were made for

various combinations of pump and probe polarisation and analyser orientation.

An auxiliary saturated absorption experiment was used to measure the probe frequency to within 10 MHz during the scans. By mixing the two lasers on a high speed photodiode and generating a beat signal, the pump frequency could also be measured for each scan. Frequency calibration of the laser scans was provided by recording the transmission of a 300 MHz confocal etalon. The intensities of the two laser beams were also recorded during the scans. Appendix A gives more detail on the generation of these signals.

The intensity of the transmitted probe beam was recorded by a computer, along with the signals needed to measure the laser frequencies and intensities. The recorded information was later transmitted to a mainframe computer for comparison with calculated profiles. Figure 2.2 shows the signals recorded during a typical probe laser frequency scan. It also indicates how the beat signal and auxiliary saturated absorption experiment were used to measure the laser frequencies.

2.2 Important features of the experiment

The design considerations mentioned earlier were followed as closely as possible, and the resulting experiment achieved most of these goals. However, there were some problems and these, along with the advantageous features of the apparatus, are discussed below.

The sodium cell was a satisfactory atomic source for this experiment because it met the requirements for a well controlled environment for the atoms. Because the windows were heated, it was not necessary to introduce a buffer gas into the cell to prevent sodium from condensing on the windows. The mean free path between Na-Na collisions was calculated to be much greater than 10 metres, which was much larger than the dimensions of the cell. It is therefore reasonable to assume that the contribution from collisional processes to the homogeneous linewidth was negligible.

The Helmholtz coils also played an important part in ensuring that the environment of the atoms was well known and controlled. Stray fields of the order of 10 mG are small enough to ensure that Zeeman splitting is negligible. However, Zeeman splitting is not the only possible perturbation caused by magnetic fields. Rinneberg et. al. (1979) observed changes in the amplitude of one of the crossover resonances in standard saturated absorption profiles with magnetic fields below 100 mG. The calculated results shown in this paper suggest that at fields of 10 mG or less, there is little disturbance of the amplitude. This was confirmed by saturated absorption experiments carried out with varying magnetic fields in this range.

Both the probe and pump laser polarisers and the analyser were mounted in a separate vacuum cell sealed onto the main cell (see Appendix A for details). Any influence on the polarisation of the probe beam between the initial

polariser and the analyser could mask the signal in a polarisation spectroscopy experiment. Similarly, a perturbation to the pump beam polarisation would disrupt the control over the driving fields in the interaction. Stress-induced birefringence in the windows of the main vacuum cell could have caused these undesirable effects. By enclosing the polarisers, the analyser and the main cell windows in a vacuum, atmospheric stress was eliminated from the main cell windows.

In order to reduce the angle between the propagation directions of the two beams, a small right-angle prism was used to reflect one beam from a side entry port (holding the initial polariser) onto the axis of the cell (see Figure 2.1). Total internal reflection was used for this purpose because the amplitude reflection coefficients for the field components perpendicular and parallel to the plane of incidence are equal (see, for example, Hecht and Zajac 1974, Chap 4.3).

The intensity of the reflected light is therefore independent of polarisation. The phase change upon total internal reflection is, however, different for the two polarisation components and the prism therefore acts as a wave-plate, with retardation dependent on the angle of incidence. As mentioned above, this sort of disturbance to the polarisation after the initial polariser is unacceptable. It was eliminated by ensuring that the polarisation of the incident beam was perpendicular to the plane of incidence.

Since a retarder between the polariser and analyser would reduce the extinction ratio by creating a circularly polarised component, this was done simply by optimising the extinction ratio with respect to rotation of the initial polariser.

Obviously it was only possible to treat linearly polarised light in this manner, so the propagation arrangement of the beams had to be chosen accordingly. Since the probe beam was always linearly polarised, it was sent through the prism; while the pump, which was circularly polarised for some experiments, was sent straight into the cell. After interacting with the pumped atoms, the probe beam was potentially no longer linearly polarised, so it could not be sent through the second prism to the analyser. However, the polarisation of the pump beam was of no concern after the interaction, so it was reflected away from the photomultiplier by the second prism. This combination ensured that both pump and probe beam initial polarisations were well known, and that the probe polarisation was only affected by the pumped atoms.

An ideal experiment of this nature would use exactly co- or counter-propagating beams, with no angular displacement between the beams. Such an arrangement maximises the signal (by maximising the overlap volume of the beams where the signal is generated) and, more importantly, eliminates residual Doppler-broadening.

However, if the pump and probe beam wavelengths are equal and the two beams are not necessarily in orthogonal polarisation states, they may only be separated before the photomultiplier using a spatial separation. This necessitates an angular separation between the beams, the size of which was determined (in this experiment) by the distance between the interaction region at the centre of the cell and the prisms. The angle between the two beam directions was approximately 1.5°.

In some earlier experiments, it was necessary to increase this angle in an attempt to prevent partial reflections of the pump beam from the main cell windows from creating additional (reduced intensity) pump beams of the opposite propagation direction. In later experiments, the window mounts were altered to deflect these spurious beams away from the interaction region.

Because the pump and probe beams are not exactly parallel, Doppler broadening of the signals is not completely eliminated. The residual Doppler broadening is calculated from the relative propagation angle to be 25 MHz (Letokhov 1976, p. 125). Ideally, it should be less than the natural width of the transition (10 MHz in the case of the D_1 line of sodium). It was not possible to reduce this angle because of the short distance from the interaction region in the centre of the cell to the right angle prisms used to separate the beams. This distance could only be increased by removing the secondary vacuum chamber for the polarisers.

As described above, the linearity of the probe interaction was verified by observing the linewidths of saturated absorption profiles. Residual Doppler broadening could have masked probe power broadening since it was larger than the natural width and independent of probe intensity. This would have erroneously indicated a linear interaction with the probe field. To avoid this possibility, the probe linearity checks were made without using the secondary vacuum chamber, allowing the angular separation to be reduced.

Because the pump beam could be many times more intense than the probe, a small proportion of the pump intensity scattered into the photomultiplier was enough to mask the signal. Because the pump beam was chopped, the phase sensitive detector was very sensitive to scattered pump light. For this reason a spatial filter, aligned for maximum transmission of the probe beam, was set up in front of the photomultiplier. However, pump scattering still caused a deterioration of the signal to noise ratio at higher pump laser intensities.

The ideal arrangement of uniform pump intensity over the interaction region could have been achieved if the probe beam had been focussed to a substantially smaller waist than the pump and the two beams had been exactly parallel and superimposed. Under these circumstances, the interaction region would be restricted to the central portion of the Gaussian intensity profile of the pump beam, where the intensity variation is smallest.

However, despite a tighter probe focus, this was not possible because of the angle between the beam directions. Consideration of the geometry of the cell and polariser chamber, and the sizes of the two beam waists indicates that, in the interaction region, the probe beam propagated through approximately 80% of the possible range of pump intensity. If the cell had been shorter, this range would have been reduced because some of the overlap volume between the two beams would have been outside the vapour. This large range may cause discrepancies between theory and experiment since the experimental profiles represent an average over the range of pump laser intensities while the theoretical calculations are restricted to a single intensity.

To finish this chapter, some important experimental parameters are collected together.

Sodium number density	5×10^{15} m^{-3}
Cell length	10 cm
Transition	D_1 (589.6 nm)
Natural width	10 MHz
Doppler width	1600 MHz
Residual Doppler width	25 MHz
Pump beam diameter	860 μm
Probe beam diameter	210 μm

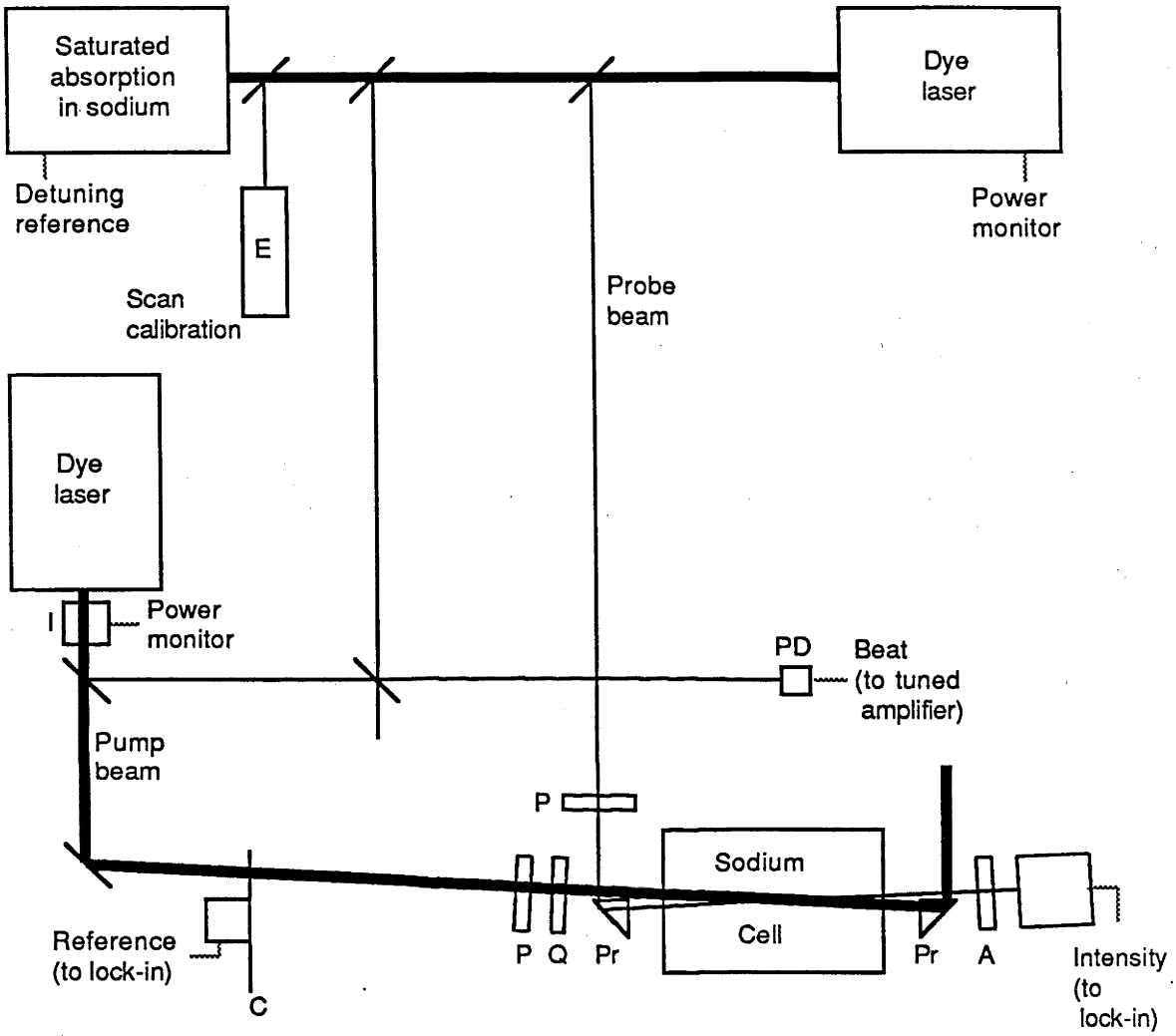

Figure 2.1 Schematic diagram of the experiment. Intense laser beams are shown as heavy lines, while weak beams are represented by fine lines. The angle between the propagation directions of the beams has been exaggerated for clarity. The analyser was used in polarisation spectroscopy experiments only, and the quarter-wave plate was used for a circularly polarised pump beam. Abbreviations used: E, 300 MHz etalon; I, intensity stabiliser; PD, fast photo-diode; C, mechanical chopper; P, polariser; Q, quarter-wave plate; Pr, prism; A, analyser; PMT, photo-multiplier tube.

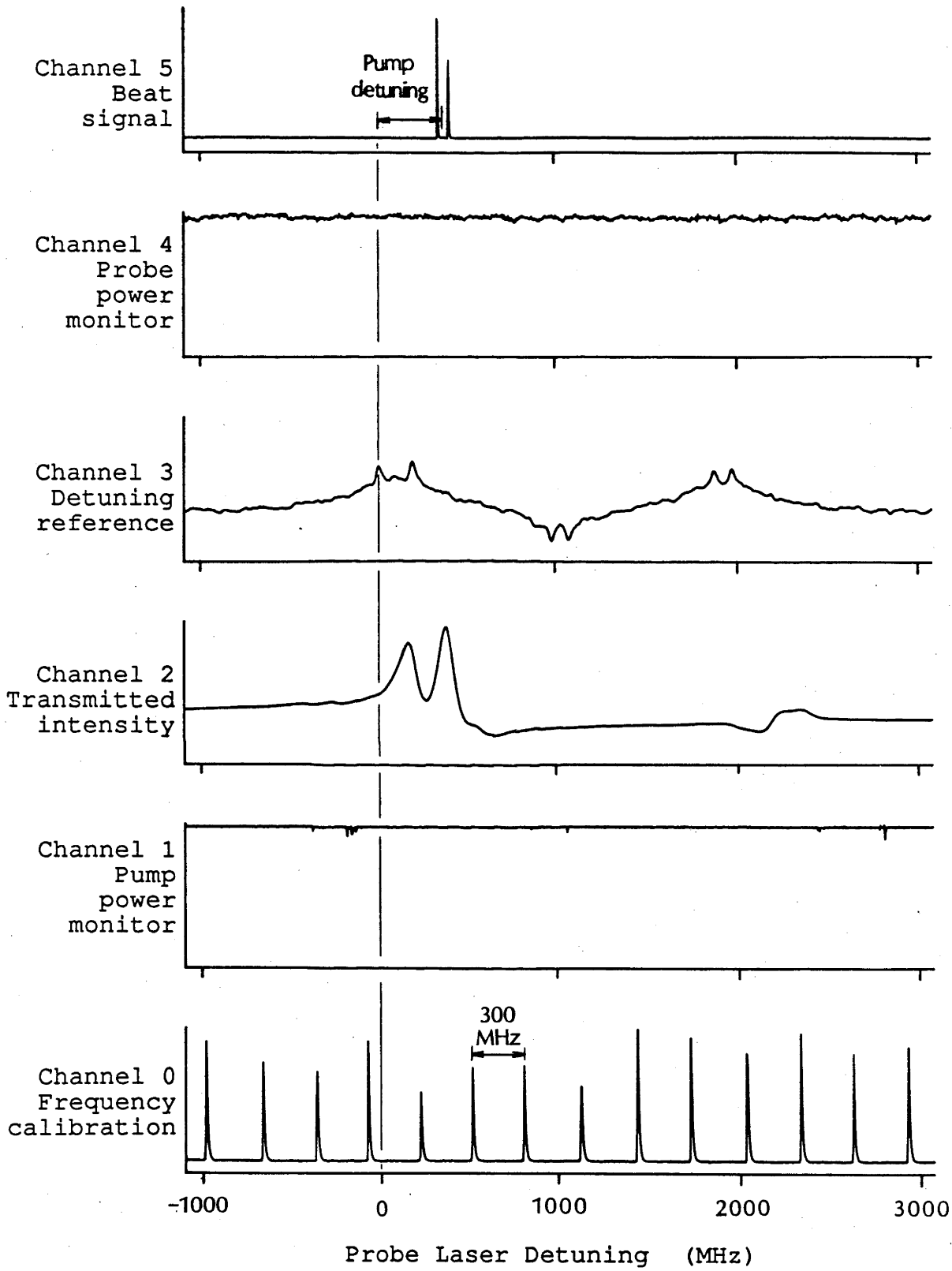

Figure 2.2 The signals recorded in a typical scan. The use of the secondary saturated absorption experiment (Channel 3) to fix the probe laser detuning origin and the beat signal (Channel 5) to measure the pump detuning are shown.

Chapter 3. Experimental Results

The results of the experiments described in the previous chapter are presented in this chapter. It is possible to gain a general understanding of the results without using the sophisticated theoretical treatment presented in Chapter 4. In addition to presenting the experimental results, this chapter includes discussions of the processes which determine the form of the profiles. An understanding of the mechanism of Doppler broadening can explain the combinations of pump and probe detunings that produce resonances. Similarly, the amplitudes and polarities of the features can be explained in terms of hyperfine and Zeeman optical pumping.

The possible experimental configurations may be divided into three categories. Section 3.1 presents experimental results obtained in the first category: saturated absorption. The formation of the profiles from the possible Doppler free resonances is also discussed in detail in this section, although it applies equally to all three categories of experiment. Sections 3.2 and 3.3 present results in the two polarisation spectroscopy categories: linearly polarised and circularly polarised pump beams respectively. A simple optical pumping theory is used to explain general features of the results in the three cases. Finally, results for higher pump intensities are shown.

3.1 Saturated absorption

The results of a set of probe frequency scans are shown in Figure 3.1. The pump and probe lasers were linearly polarised in the same direction and were co-propagating. The intensity of the probe laser after transmission through the vapour was measured without using an analyser. These profiles are therefore standard saturated absorption profiles with the modifications mentioned in Chapter 1. The complete set of profiles has been combined into one three-dimensional plot to indicate clearly the variation of the profiles with pump laser detuning. The pump laser was weak enough to allow the individual features of the profiles to be resolved. At higher intensities many of the peaks could not be resolved due to power broadening.

The laser detunings indicated in Figure 3.1 (and used in the rest of this thesis) are relative to the lowest frequency hyperfine transition in the D_1 line, as shown in Fig. 3.2. Figure 3.2 also shows the hyperfine levels involved and indicates the labelling system used in the discussion. The detunings are given by

$$\delta_\eta = \nu_\eta - \nu_{ca} = \nu_\eta - \nu(3p\ ^2P_{1/2}\ F=1 \rightarrow 3s\ ^2S_{1/2}\ F=2)$$

where $\eta = 1$ designates the probe laser and $\eta = 2$ designates the pump laser. It can be seen from Figure 3.2 that a laser detuned by, for example, 1772 MHz is resonant with the bc hyperfine transition. The vertical line from the baseline of each profile in Figure 3.1 to the curve indicates the

position where pump and probe laser detunings are equal.

The first point to establish in discussing these profiles is the origin of the various features. In a Doppler free atomic system a feature would be expected whenever the lasers were both resonant with a transition. Detunings of 0 MHz, 189 MHz, 1772 MHz or 1961 MHz for either laser would be expected to produce a feature corresponding to resonance with the ac, ad, bc and bd transitions respectively. There would be 16 peaks within the range of detunings of Figure 3.1. Clearly, there are many more peaks and they are not restricted to these values of laser detuning.

The configuration of features in Fig. 3.1 is due to the Doppler effect. To determine the origin of each peak, consider the apparent frequencies of the lasers in the rest frame of the atoms of a particular velocity sub-group. The Doppler shifted detunings of the two lasers are

$$\begin{aligned} \delta_1' &= \delta_1 - \varepsilon\delta_D = \delta_i \\ \delta_2' &= \delta_2 - \delta_D = \delta_f \end{aligned} \qquad (3.1)$$

where δ_1 and δ_2 are the probe and pump laser detunings respectively in the laboratory frame and δ_D is the Doppler shift for the velocity sub-group. The parameter ε indicates the relative propagation directions of the pump and probe fields by

ε = 1 co-propagating fields

-1 counter-propagating fields

For a resonance to occur, the two Doppler shifted frequencies must both coincide with a transition. This is expressed by the second equality in each of Eqs. 3.1 where δ_i and δ_f are detunings corresponding to a resonance. The possible values of δ_i and δ_f are 0 MHz, 189 MHz, 1772 MHz and 1961 MHz as listed above. Eliminating the Doppler shift from Eqs. 3.1 gives the condition on the laboratory frame detunings, δ_1 and δ_2, of the two fields for the production of a feature in the Doppler broadened profile

$$\delta_2 - \varepsilon\delta_1 = \delta_f - \varepsilon\delta_i \qquad (3.2)$$

since $1/\varepsilon = \varepsilon$.

When plotted in the δ_1,δ_2 plane this equation represents a set of straight lines inclined at ±45° to the δ_1 and δ_2 axes. Points on these lines are combinations of δ_1 and δ_2 for which there exists at least one velocity sub-group with both pump and probe lasers Doppler shifted into resonance with a transition. There are nine different values of $\delta_f - \varepsilon\delta_i$ so there are nine lines in the set. These lines are plotted in Figure 3.3 for the co-propagating case corresponding to Fig. 3.1. The Doppler effect converts the sixteen peaks in the Doppler free plane into nine "ridges" in the Doppler broadened plane.

Although the three dimensional plotting distorts the orientation of the axes and makes it difficult to see the 45° lines in the data, Fig 3.1 shows the same positioning of peaks along nine different 45° lines. Since the line from the baseline of each profile to the curve is drawn at the position of equal pump and probe detuning, these lines must all fall on line I of Fig. 3.3. Therefore, the largest peak in each profile of Fig. 3.1 lies on one of the expected 45° lines. Since the separations of individual peaks are maintained as the pump detuning is changed, all other peaks lie along 45° lines as described above.

Some further information about the formation of the peaks can be obtained by considering the particular combinations of δ_i and δ_f that generate each of the nine possible lines. Table 3.1 shows the combinations of resonances that produce the lines as labelled in Fig. 3.3. In this table, resonances for the probe laser (values of δ_i) are indicated in lower case letters while upper case letters are used for the pump laser. This convention will be followed in the rest of this thesis.

The table can be used to identify the resonances which contribute to any peak on the 45° lines in Fig. 3.3. For example, any peak on line I is due to the four velocity subgroups for which the pump and probe lasers are Doppler-shifted into resonance with the same transition. This can be seen from Table 3.1 because all line I entries occur on the diagonal. In contrast, a peak on line III is due to two

velocity sub-groups: one for which the pump laser is resonant with the AD transition and the probe is resonant with ac, and the other with the pump tuned to BD and the probe to bc.

From Table 3.1 and Fig. 3.2 it can be seen that the various 45° lines are made up of "I systems" (line I), "V systems" (lines II and III), "Λ systems" (lines IV and V) and "N systems" (lines VI, VII, VIII and IX). "I systems" are those for which the pump and probe lasers are resonant with the same transition. This sort of system produces the "principal resonances" of standard saturated absorption and polarisation spectroscopy.

The pump and probe lasers share a common lower state in "V systems" and a common upper state in "Λ systems". An "N system" resonance is one with no common state. For an "N system" resonance, the influence of the pump laser on the probe (necessary for generating a signal in saturated absorption or polarisation spectroscopy) is due to spontaneous emission from the upper state of the pump transition to the lower state of the probe. Peaks due to "V system", "Λ system" and "N system" resonances are known as crossover resonances.

When describing a combined pump and probe laser resonance, levels common to both lasers will be written in underlined lower case letters. Thus $\underline{ac}$ is an example of an "I system" resonance, with both the pump and probe lasers Doppler shifted into resonance with the ac transition. A$\underline{c}$b

is a "Λ system" resonance with the pump laser resonating with ac and the probe with bc. This notation system has the advantage of emphasising the type of resonance by indicating the number of levels involved in the transition by the number of characters in the designation. Using this notation, the contributing resonances for each line are shown in Fig. 3.3.

The signal at any given combination of pump and probe detuning is due to the sum of the contributions from all velocity sub-groups that generate a resonance. However, the terms in the sum are weighted by the relative numbers of atoms in the velocity sub-groups. This number is derived from the usual Maxwellian velocity distribution, although it is more convenient in this context to express it in terms of the Doppler shift, δ_D

$$W(\delta_D) = \frac{2}{\Delta_D}\sqrt{\frac{\ln 2}{\pi}}\exp\left[\frac{-4\ln 2\ \delta_D^2}{\Delta_D^2}\right] \qquad (3.3)$$

where Δ_D is the full width at half maximum of the Doppler profile (Corney 1977, Chap. 8). In Fig. 3.3, the Doppler shift of a resonant velocity sub-group is equal to the distance along either axis from the point (δ_1,δ_2) to the resonance position. For the point marked by the dot on line II, the two Doppler detunings are indicated as $\delta_D(C\underline{b}d)$ and $\delta_D(C\underline{a}d)$.

The width of the Doppler profile in the experimental results (Fig. 3.1) was 1.6 GHz which is comparable to the ground state hyperfine splitting of 1.772 GHz. Eq. 3.3 shows that the Cbd resonance is therefore weighted substantially more strongly than the Cad resonance. It thus makes a greater contribution to the signal recorded at the example point.

Because the ground state hyperfine splitting is comparable to the Doppler width, it is possible to distinguish different lower levels in the experimental profiles. This is demonstrated most obviously in Fig. 3.1 by peaks along line II. At low pump detunings they are produced predominantly by the Cad resonance and are negative going. However, at high pump detunings, the Cbd resonance is more important and the signal is positive. The ability to separate different lower levels will help in determining mechanisms responsible for various features in the profiles.

The upper level hyperfine splitting (189 MHz) is substantially smaller than the Doppler width. This means that it is not possible to distinguish between contributions from different upper level resonances. A similarly placed example point on line I, for example, would experience approximately equal contributions from bc and bd resonances.

Fig. 3.3 also explains why the signal on lines IV, VI and VII in Fig. 3.1 falls as the pump detuning increases. This is simply because the Doppler shifts of the resonances

producing the signal are increasing so the Doppler weight factor is decreasing. Similar arguments explain the reduction in signal with decreasing pump detuning along lines V, VIII and IX. The same reductions would occur along lines I, II and III but at pump detunings beyond the range shown in Fig. 3.1.

It is worthwhile carrying out a similar analysis for standard saturated absorption experiments where the pump and probe frequencies are equal and the two beams are counter-propagating. Figure 3.4 shows the combinations of pump and probe frequencies which produce resonances for the counter-propagating case, $\varepsilon = -1$. Because the two laser frequencies are equal, a standard saturated absorption profile is represented by a scan along a line at $+45^\circ$ to the axes and passing through the origin. Features are expected whenever this line intersects one of the -45° lines in Fig. 3.4.

It can be seen from the identification of the sources of the various lines in Fig. 3.4 that, in contrast to the co-propagating case, the four possible "I system" resonances appear as separate features. This geometry is therefore more directly suited to high resolution spectroscopy where the separations of levels are of interest, although the same information can be obtained from the co-propagating geometry. The "I system" resonances are combined into one peak in the co-propagating case whereas the four possible "N system" resonances are separated.

Figure 3.5 shows a standard saturated absorption profile from the same experimental apparatus and three of the profiles from Fig. 3.1. The standard saturated absorption profile was taken during the initial set-up of the sodium cell before the Helmholtz coils were installed. For comparison, pump detunings of -60 MHz, 883 MHz and 1804 MHz were chosen from Fig. 3.1.

The most obvious difference between the two types of profile is the apparent scaling of the probe detuning axis. This is because a probe frequency scan is represented by a horizontal line in Fig. 3.3 (for a fixed pump detuning) and by a line at +45° in Fig. 3.4 (if the two laser detunings are equal). The probe detuning scan range required to intercept all three triplets of lines in the fixed pump detuning case is twice that required in the standard saturated absorption case, resulting in the larger separation of features.

The second major difference is in the sizes of the peaks. This is largely due to the different combinations of resonances in the two geometries that produce each peak. Using Figs. 3.3 and 3.4 to identify the origins it can be seen that the two types of profiles are consistent. For example, the negative going peak in the centre of the standard saturated absorption profile is due to all "N system" resonances. These appear on lines VI, VII, VIII and IX in the fixed pump detuning case. Fig. 3.1 shows all these features as negative going peaks. However, comparison of Figs. 3.3 and 3.4 shows that corresponding resonances in

the two types of experiment can be weighted differently by the Doppler effect. This causes further differences in the amplitudes of some peaks.

Having identified the resonances that contribute to the features in the profiles, it is worthwhile to attempt to identify the processes that determine the amplitudes of the peaks.

The signal measured in this experiment was the intensity of the probe laser transmitted by the pumped atomic medium. However, the pump laser was chopped and the transmitted intensity measured with a phase sensitive detector. This means that the signal was proportional to the difference between the transmitted intensity with and without the pump laser. This is the reason for the absence from the profiles of any Doppler broadened absorption of the probe beam. It is also the reason for the generation of negative going peaks in some profiles.

To understand the polarities of the peaks in general terms, consider a simplified four state system where Zeeman degeneracy is ignored (Fig 3.2). Although Zeeman optical pumping is expected to be important, in most cases it is possible to explain the polarity of the peaks by considering only hyperfine optical pumping.

First, consider the "I system" resonances. When the pump laser is present the lower state population is reduced by saturation and hyperfine optical pumping. The vapour therefore exhibits higher transmission in this half of the cycle and the signal is positive. In contrast, all peaks due to "Λ system" or "N system" resonances (lines IV, V, VI, VII, VIII and IX) in Fig. 3.3 are negative going. This is because the population of the lower state of the probe transition in each case is increased by hyperfine optical pumping when the pump laser is present. This causes a reduction in the transmitted intensity during this half of the chopper cycle and therefore negative peaks.

Zeeman optical pumping becomes more important in the "V system" resonances of lines II and III. Consider first the Dac and Dbc resonances that contribute to line III. In both cases, all Zeeman sub-level populations of the probe transition are depleted by the pump laser, causing a positive going signal. The same argument applies to the Cbd transition that is the major contributor to line II at large pump detunings. For these resonances, the same conclusion would be drawn if Zeeman degeneracy were ignored.

However the Cad resonance behaves differently. Figure 3.6 shows that optical pumping by the π polarised pump beam increases the populations of the $m_a = \pm 2$ Zeeman sub-levels as well as of level b. The π polarised probe beam causes transitions from all five Zeeman sub-levels, some of which ($m_a = \pm 2$) experience increased absorption and some

($m_a = 0,\pm1$) reduced. The magnitude and sign of the resultant peak arise from a balance between the degree of Zeeman optical pumping and the strengths of the individual Zeeman transitions.

The role of optical pumping in these profiles can be examined more closely with the aid of a theory developed by Nakayama (1981b, 1985). For all possible Zeeman transitions of the probe laser, modifications to the ground state populations due to one cycle of optical pumping by the pump laser are calculated. The amplitude of each resonance is the sum of contributions from the constituent Zeeman transitions.

The amplitude is calculated from the susceptibility, $\chi_{pp}^{(q)}(\omega)$, of the medium experienced by each polarisation component, p, of the probe beam in the presence of a pump beam of polarisation, q. The polarisation components indicate π polarisation by p = 0, $\sigma_{\pm}$ polarisation by p = $\pm$ and σ_+ or σ_- polarisation by p = + or p = - respectively.

A π polarised field is linearly polarised in the direction of the z axis and propagates along either the x or y axes. For a beam propagating in the same direction, a component of polarisation perpendicular to the z axis is described as $\sigma_{\pm}$, or alternatively linear σ. In the case of circular polarisation, the z axis is defined to be in the direction of propagation and the polarisation is described as σ_+ (left circularly polarised) or σ_- (right circularly polarised). In this case, linearly polarised light

propagating in the same direction is a mixture of σ_+ and σ_- components.

The expression for the susceptibility is (Eq. 1 Nakayama 1985)

$$\chi_{pp}^{(q)}(\omega) \propto \sum_{i,j} -I_{pp}^{(q)} \, D(\omega_i, \omega_j, \Delta_D)\,(\omega-\omega_{ij}-i\gamma)^{-1} \qquad (3.4)$$

where the pump and probe beams are Doppler shifted into resonance with transitions at frequencies ω_i and ω_j respectively. $D(\omega_i,\omega_j,\Delta_D)$ is the Doppler weight factor for the velocity subgroup and $\omega_{ij} = (\omega_i+\omega_j)/2$. The summation in Eq. 3.4 is taken over all Zeeman sub-levels that can interact with the two lasers. The amplitude, $I_{pp}^{(q)}$, is calculated in terms of the transition probabilities of the individual Zeeman transitions of the pump and probe lasers. It includes the effect of spontaneous emission between levels involved in the pump and probe transitions and therefore accounts for optical pumping between Zeeman sub-levels.

Nakayama does not include the negative sign in the expression for the susceptibility (Nakayama 1985). However, comparison of the expression for the amplitude factor (Eq. 2 Nakayama 1985) with Eq. 23 in his earlier paper where it was first derived (Nakayama 1981b), shows that it was originally present. This sign is necessary in explaining some features of polarisation spectroscopy profiles.

Because of the different combinations of resonances that make up each peak, it was not possible to use the values in Table 1 of Nakayama's 1985 paper for the current experiment. That table refers only to the standard saturated absorption geometry and the calculations were therefore repeated to include the co-propagating experiment.

The signal in a saturated absorption experiment with parallel linear polarisations is given by (Nakayama 1985)

$$\mathrm{Im}\left[\chi_{00}^{(0)}\right] \propto \sum_{i,j} -I_{00}^{(0)}\, D(\omega_i, \omega_j, \Delta_D)\, \frac{\gamma}{(\omega-\omega_{ij})^2+\gamma^2} \qquad (3.5)$$

since both beams have only π polarisation components. Table 3.2 shows the calculated contribution from each resonance and indicates the lines of Figs. 3.3 and 3.4 on which each resonance is located. Using the Doppler shift for each resonance, the amplitude of each peak can be calculated. These calculated amplitudes have been marked on all the peaks in Fig. 3.5.

It can be seen that this simple theory predicts the general form of the profiles. The signs of all peaks are correctly predicted and the amplitudes are approximately correct. The discrepancies in Fig. 3.5 are presumably due to the intensity of the pump laser. If the pump field is strong enough, the assumption of a single cycle of optical pumping may be invalidated, and coherences may also become important. In a more sophisticated calculation, Rinneberg et. al. (1980)

have shown that atomic alignment must be included. They demonstrate (experimentally and theoretically) that magnetic fields have a substantial influence on the amplitudes of the peaks, particularly the combined Dac and Cad crossover. This may be a contributing factor to the poor agreement for this peak in the standard saturated absorption profile of Fig. 3.5.

Despite the slight discrepancies shown in Fig. 3.5, this theory can be used to show the importance of Zeeman optical pumping in the Cad resonance. Table 3.3 shows the calculated contribution of each Zeeman transition to the amplitude. Note that it includes "N system" combinations of Zeeman sub-levels where the pump and probe transitions do not share a common state. This sort of combination is the only type that can produce a contribution for the m = ±2 transitions of the probe beam.

It can be seen from Table 3.3 that probe transitions between m = ±2 sub-levels produce a strong negative contribution to the signal. Probe transitions between m = ±1 sub-levels produce a positive contribution (adding the "N system" and "V system" values). However the negative contribution from m = ±2 transitions swamps this positive contribution. This example shows that the amplitudes and signs of the peaks in these experiments are due to a balance between Zeeman and hyperfine optical pumping processes. In many cases it may be possible to predict the sign of a peak by considering only hyperfine pumping within the simplified

four state system, but in general it is necessary to include the Zeeman sub-levels in order to predict the amplitude.

It is known that the polarisations of the two lasers influence saturated absorption spectroscopy profiles (Sargent 1976, Pappas et. al. 1980). Fig. 3.7 shows co-propagating saturated absorption profiles for four different combinations of pump and probe polarisation. Figs 3.7b to 3.7d are earlier results without the slight tilt on the windows of the cell to deflect reflected pump beams away from the probe beam (see Chapter 2). Features marked with an asterisk are due to these spurious reflections and should be ignored.

Fig. 3.7 shows that the pump polarisation influences the relative heights of the "I system" (line I) and "V system" (lines II and III) resonances more than the "Λ systems" (lines IV and V) and "N systems" (lines VI, VII, VIII and IX).

As mentioned earlier, Zeeman optical pumping is more important in the "V system" resonances. As the probe polarisation is rotated from being parallel to the pump polarisation to perpendicular, it changes from pure π polarisation through a mixture of π and $\sigma_{\pm}$ to pure $\sigma_{\pm}$. This means that different Zeeman transitions are excited by the probe laser. Since the pump is linearly polarised in all cases, the lower level population distribution induced by the pump will be the same in Figs. 3.7a to 3.7c. The changing amplitude of the "V system" peaks therefore reflects the

differing strengths of the Zeeman transitions that contribute to the probe transition. In particular, the Cad resonance is only negative going when the probe laser is π polarised. Note that this cannot be seen directly from Fig. 3.7. This is because the line II peak at the pump detuning shown contains a significant contribution from the Cbd resonance. However, profiles taken at lower pump detuning show a positive peak on line II.

For the case of a circularly polarised pump laser (Fig. 3.7d), Zeeman optical pumping is again important for the "V system" peaks. The population of the $m_a = 1,2$ sub-levels is increased by a σ_+ pump laser. Some of the Zeeman transitions that contribute to the absorption of the probe laser experience increased absorption and some reduced. The sign of the resultant peak is again due to the relative strengths of the individual transitions.

3.2 Polarisation spectroscopy: linearly polarised pump

Figure 3.8 shows a series of polarisation spectroscopy profiles with linearly polarised, co-propagating beams. Since the two lasers were co-propagating, the same identification of the peaks (Fig. 3.3) can be made. However, the amplitudes of corresponding peaks are obviously substantially different.

Amplitudes and signs of the peaks in polarisation spectroscopy are not as easy to understand qualitatively as in saturated absorption profiles. The polarisation

spectroscopy signal for this combination of laser polarisations is proportional to

$$\frac{\pi^2 l^2}{4\lambda^2} |\chi_{00}^{(0)} - \chi_{\pm\pm}^{(0)}|^2 - \frac{\pi\theta l}{\lambda} \mathrm{Im}(\chi_{00}^{(0)} - \chi_{\pm\pm}^{(0)}) \qquad (3.6)$$

(Nakayama 1985) where $\chi_{00}^{(0)}$ and $\chi_{\pm\pm}^{(0)}$ are the susceptibilities experienced by the π and $\sigma_{\pm}$ components respectively of the probe beam in the presence of the π polarised pump beam. The $\sigma_{\pm}$ components represent the component of the linearly polarised probe beam perpendicular to the pump polarisation. θ (assumed small) is the angle through which the analyser is rotated from the crossed orientation and l is the length of the medium. The signal is due to differences between the absorption coefficients and refractive indices for π and $\sigma_{\pm}$ polarised components of the probe beam.

Again, Nakayama's theory can help to explain the amplitudes of the features. Table 3.4 shows values of the amplitudes, $I_{00}^{(0)}$ and $I_{\pm\pm}^{(0)}$, of the susceptibilities for the 16 possible resonances. Both terms in Eq. 3.6 produce Lorentzian shaped peaks from Eq. 3.4. The amplitude of a peak in the crossed analyser case ($\theta = 0$) is proportional to the square of the entry in the difference column $(I_{00}^{(0)} - I_{\pm\pm}^{(0)})$.

The most striking features of Fig. 3.8 are the reduction in the signal at high pump detuning and the almost total absence of "Λ system" and "N system" crossovers. As

mentioned earlier, the signal on line I at low pump detuning is almost entirely due to the ac and ad resonances. Table 3.4 shows that, in both cases, there is a strong disparity between the susceptibilities for the π ($\chi_{00}^{(0)}$) and σ ($\chi_{\pm\pm}^{(0)}$) components of the probe beam. The probe beam thus experiences a polarisation rotation (since the difference in absorption coefficient changes the relative amplitudes of the two components) and becomes elliptically polarised (since the two types of component become dephased due to the difference in refractive index). These two effects cause a strong polarisation spectroscopy signal.

In contrast, the signal at high pump detuning is predominantly due to bc and bd resonances. As can be seen from Table. 3.4, both types of polarisation component of the probe beam experience a small effect from the bc resonance, while the bd resonance produces strong effects. However, since the two susceptibilities are approximately equal in this case, there is little effect on the polarisation of the probe laser, resulting in a small signal. This highlights the importance of the detection technique in the profiles. Table 3.2 shows that the bd resonance produces a strong signal in a saturated absorption experiment. However, the polarisation spectroscopy signal is small, causing the reduction in signal at high pump detuning.

Table. 3.4 also predicts the reduced amplitudes of the "Λ system" and "N system" peaks. In particular, the line V, VIII and IX crossovers are shown to be larger than

corresponding peaks on lines IV, VI and VII.

Polarisation spectroscopy experiments are often carried out with the analyser slightly rotated from the crossed position, transmitting a small proportion of the probe beam. This light behaves as a local oscillator, mixing with the scattered signal beam. Negative going peaks are possible due to this heterodyning effect, whereas Eq. 3.6 shows that only positive signals are expected with a crossed analyser. Figure 3.9 shows co-propagating polarisation spectroscopy profiles for a range of analyser orientations.

As the analyser is rotated away from the crossed position, it can be seen that the differences between the sizes of the central peaks (principal resonances and "V system" crossovers) and the outlying crossovers ("Λ system" and "N system" resonances) are reduced. Eq. 3.6 shows that as θ increases, the heterodyned term becomes more important. Compared with the linear dependence on the susceptibility difference of this term, the quadratic dependence of the first term magnifies the range of peak heights due to the range of values of the susceptibility difference.

As the analyser is rotated, the heterodyned term causes significant changes to the profiles. However, if it is rotated beyond a limiting position, no further changes to the form of the profiles occur because the heterodyned term completely masks the quadratic term. The analyser

orientation that gives a predominantly heterodyned signal can only be determined from the experiment. This is because only relative values of the amplitudes, $I_{pp}^{(q)}$, of the susceptibility are calculated. It is therefore not possible to determine the relative importance of the heterodyned and quadratic terms for any particular value of θ.

The other dramatic effect of the analyser rotation is the change in polarity of some peaks. Eq. 3.6 indicates a dependence of the signal on the sign of the rotation of the analyser. Because of the negative sign in Eq. 3.4, if θ is positive, the heterodyned term takes on the same sign as the difference term listed in Table 3.4. Figure 3.9 shows that, as the analyser is rotated, certain peaks become negative.

Using Fig. 3.3 the most obvious negative peaks may be identified as lying on lines I and V. The largest negative entries in the difference column of Table 3.4 correspond to resonances contributing to these lines. If the analyser rotation is positive, the optical pumping theory has therefore correctly predicted the polarities of the features.

Examination of the derivation of Eq. 3.6 (Nakayama 1981b) shows that the angle θ is defined to be positive if the analyser is rotated clockwise while looking in the direction of propagation of the probe beam. As mentioned in Appendix A, the orientation of the analyser was adjusted using a micrometer attached to an arm on the polariser vacuum chamber. From the geometry of the adjustment arm, it was

confirmed that θ was positive. The entries in Table 3.4 therefore correctly predict the polarity of the peaks in Fig. 3.9.

3.3 Polarisation spectroscopy: circularly polarised pump

When polarisation spectroscopy was first introduced (Wieman and Hansch 1976), a circularly polarised pump beam was used. Figure 3.10 shows a set of co-propagating polarisation spectroscopy profiles using a circularly polarised pump beam and a linearly polarised probe beam with the analyser rotated by 1.6° from the crossed orientation.

For this configuration, the signal can be expressed in a similar fashion to Eq. 3.6 (Nakayama 1985).

$$\frac{\pi^2 l^2}{4\lambda^2} \left|\chi_{++}^{(+)} - \chi_{--}^{(+)}\right|^2 + \frac{\pi\theta l}{\lambda} \mathrm{Re}\left(\chi_{++}^{(+)} - \chi_{--}^{(+)}\right) \qquad (3.7)$$

The real part of the complex Lorentzian in the susceptibility (Eq. 3.4) produces a dispersion shaped profile which becomes important when the analyser is no longer crossed. Figure 3.10 confirms this feature. As in the linearly polarised pump case, if the analyser is in the crossed position only positive peaks are expected, and the contrast between the large and small peaks is increased. This was also observed in the experiment.

Table 3.5 shows the calculated amplitudes of the two susceptibilities that contribute to the signal (Eq. 3.7). In a similar fashion to the linearly polarised case, the values in the table can be seen to match the general trends in the amplitudes of the features. In particular, the reduction of the principal resonance peak with increasing pump detuning occurs because the bc and bd resonances have a much smaller contribution than the ac resonance.

Another notable feature of Fig. 3.10 is the sign of the dispersion shaped profiles. Features on line II at high pump detuning and on line IV have opposite sign to the other features. These features correspond to entries in Table 3.5 that have positive values of $I_{++}^{(+)} - I_{--}^{(+)}$, in contrast to the other resonances. Inverted crossover resonances in polarisation spectroscopy of sodium have been observed (Gawlik and Series 1979, Nakayama et. al. 1980) and explained in terms of this theory by Nakayama (1981a).

3.4 Increased pump intensity

Having demonstrated that optical pumping is extremely important in saturated absorption and polarisation spectroscopy profiles in this atomic system, it is worthwhile to consider the A.C. Stark effect since it is another important aspect of the behaviour of strongly driven atoms. A.C. Stark splitting has been observed in Doppler broadened media. Delsart and Keller (1976, 1978a) used three-level cascade systems in a neon discharge while Cahuzac and Vetter (1976) used a three-level "V system" in a xenon discharge.

Gawlik and Series (1979) observed first decoupling of the hyperfine structure followed by A.C. Stark splitting as the pump power was increased in a polarisation spectroscopy experiment on the D_2 line of sodium.

Using a graphical technique, Delsart and Keller (1978a) derived conditions on the frequencies and relative propagation directions of the pump and probe lasers for the observation of the Autler-Townes effect in Doppler broadened three-level systems. For "Λ systems" and "V systems" the pump and probe lasers must be co-propagating and the probe frequency must be less than that of the pump laser. In the case of a two-level "I system" resonance, a similar analysis indicates that splitting can be observed with co-propagating beams. These analyses were the reason for using the co-propagating geometry in these experiments.

Because of the complicated Zeeman structure of the sodium levels, any particular resonance may be made up of various combinations of the four possible system types. This makes it difficult to establish which, if any, of the peaks in the experiments discussed here might exhibit the Autler-Townes effect. However, since the possible three-level resonances are in the folded configuration (i.e. "Λ systems" or "V systems"), the co-propagating geometry is the better arrangement to use in attempting to observe the Autler-Townes effect in this system.

Figure 3.11 shows a set of saturated absorption profiles with co-propagating beams for a range of pump laser powers. The most obvious effect of the increased pump intensity is to power broaden the profiles, destroying the resolution of the excited state hyperfine structure. The signal to noise ratio is also degraded by increased scattering of the pump laser into the photomultiplier.

It is difficult positively to identify any Autler-Townes splitting in Fig. 3.11. It may be present in the crossover resonances at low probe detuning. The development of these three features is qualitatively similar to the appearance of the Autler-Townes effect as observed by Gawlik and Series (1979). The central peak of this set is due to the Bca and Bda resonances which are "Λ system" resonances with a probe frequency that is less than the pump frequency. This configuration satisfies the conditions for observation of the Autler-Townes effect in a Doppler broadened system mentioned above. The possible "V system" resonances have a smaller difference between the pump and probe frequencies which makes Autler-Townes splitting more difficult to observe.

However, "I system" resonances would also be expected to exhibit splitting and there is no evidence of it in Fig. 3.11. Because the splitting of the crossover resonance is inconclusive and there is no splitting of the principal resonance, it must be concluded that the Autler-Townes effect was not observed in these experiments. If the pump intensity was increased, the uncertainty over the behaviour of the

crossover resonance might be resolved. However, this would require substantial improvements to the signal to noise ratio.

Improvements to the geometry to reduce the range of pump intensities in the interaction region would also be beneficial. As mentioned in Chapter 2, the probe experiences 80% of the range of possible pump intensities as it propagates through the vapour, resulting in 55% of the possible pump Rabi frequency range. The observed profiles are an average over the interaction region and therefore include contributions from this range of pump Rabi frequencies. Since these contributing profiles would have a range of splittings, the resultant splitting could be masked. This effect would cause A.C. Stark split profiles (that might be observed in a better geometry) to appear power broadened, as those in Fig. 3.11 are.

It can be seen from the experimental results presented in this chapter, and their comparison with the simple optical pumping theory, that Zeeman and hyperfine optical pumping is of paramount importance in this sort of experiment. In atomic systems with several lower states which have substantially longer lifetimes than the upper states, changes of the lower level population distribution due to optical pumping are more important than saturation effects at moderate pump power.

For most of the experimental profiles presented here, the simple optical pumping theory is capable of qualitatively predicting the general features. However, it cannot be expected accurately to predict the details since it ignores coherences and accounts for only one cycle of optical pumping. It is obvious from the power broadening in the profiles (see, for example, Fig. 3.8) that the intensity of the pump laser was sufficient to cause additional non-linear effects. Although these effects are not included in this theory, it is useful in understanding the physical processes involved.

Chapter 4 describes a more sophisticated theoretical treatment that attempts to include these higher order effects.

Table 3.1

Table showing the resonances that contribute to the nine lines of Eq. 3.2 (co-propagating case).

δ_f \ δ_i	ac	ad	bc	bd
AC	I	II	IV	VI
AD	III	I	VII	IV
BC	V	VIII	I	II
BD	IX	V	III	I

Table 3.2

Calculated amplitudes of the components of the susceptibility relevant to saturated absorption. The line on which each resonance lies and the type of level system are also shown.

Resonance	$-I_{00}^{(0)}$	Resonance Position counter-propagating	co-propagating	System Type
$\underline{ac}$	194	I	I	I
$\underline{ad}$	246	II	I	I
$\underline{bc}$	22	III	I	I
$\underline{bd}$	194	IV	I	I
$\underline{D}\bar{a}c$	-6	V	III	V
$C\bar{a}\underline{d}$	-114	V	II	V
$\underline{D}\bar{b}c$	46	VI	III	V
$C\bar{b}\underline{d}$	58	VI	II	V
$\underline{B}\bar{c}a$	-26	VII	V	Λ
$\underline{A}\bar{c}b$	-14	VII	IV	Λ
$\underline{B}\bar{d}a$	-78	VIII	V	Λ
$\underline{A}\bar{d}b$	-186	VIII	IV	Λ
AC,bd	-66	IX	VI	N
AD,bc	-54	IX	VII	N
BC,ad	-54	IX	VIII	N
BD,ac	-162	IX	IX	N

Table 3.3

Calculated contributions to the $C\bar{a}d$ resonance of each possible combination of pump and probe Zeeman transition.

Pump Transition m_c	m_a	Probe Transition m_d	m_a	Resonance Type	$-I_{00}^{(0)}$
-1	-1	-2	-2	N	-72
-1	-1	-1	-1	V	27
-1	-1	0	0	N	0
0	0	-1	-1	N	-12
0	0	0	0	V	0
0	0	1	1	N	-12
1	1	0	0	N	0
1	1	1	1	V	27
1	1	2	2	N	-72
				Total	-114

Table 3.4

Calculated amplitudes of the components of the susceptibility relevant to polarisation spectroscopy with linearly polarised pump beam. The line on which each resonance lies and the type of level system are also shown.

Resonance	$I_{00}^{(0)}$	$I_{\pm\pm}^{(0)}$	$I_{00}^{(0)} - I_{\pm\pm}^{(0)}$	Position (co-propagating)	Type
$\underline{ac}$	-194	37	-231	I	I
$\underline{ad}$	-246	-57	-189	I	I
$\underline{bc}$	-22	-9	-13	I	I
$\underline{bd}$	-194	-203	9	I	I
$D\underline{a}c$	6	-183	189	III	V
$C\underline{a}d$	114	-117	231	II	V
$D\underline{b}c$	-46	-37	-9	III	V
$C\underline{b}d$	-58	-71	13	II	V
$B\underline{c}a$	26	47	-21	V	Λ
$A\underline{c}b$	14	13	1	IV	Λ
$B\underline{d}a$	78	141	-63	V	Λ
$A\underline{d}b$	186	207	-21	IV	Λ
$AC,\underline{bd}$	66	67	-1	VI	N
AD,bc	54	33	21	VII	N
BC,ad	54	33	21	VIII	N
BD,ac	162	99	63	IX	N

Table 3.5

Calculated amplitudes of the components of the susceptibility relevant to polarisation spectroscopy with circularly polarised pump beam. The line on which each resonance lies and the type of level system are also shown.

Resonance	$I_{++}^{(+)}$	$I_{--}^{(+)}$	$I_{++}^{(+)} - I_{--}^{(+)}$	Position (co-propagating)	Type
$\underline{ac}$	-236	79	-315	I	I
$\underline{ad}$	-194	-109	-85	I	I
$\underline{bc}$	-22	-9	-13	I	I
$\underline{bd}$	-236	-161	-75	I	I
$D\underline{a}c$	-216	39	-255	III	V
$C\underline{a}d$	-54	51	-105	II	V
$D\underline{b}c$	-34	-49	15	III	V
$C\underline{b}d$	-32	-97	65	II	V
$B\underline{c}a$	14	59	-45	V	Λ
$A\underline{c}b$	16	11	5	IV	Λ
$B\underline{d}a$	72	147	-75	V	Λ
$A\underline{d}b$	234	159	75	IV	Λ
AC,bd	54	79	-25	VI	N
AD,bc	36	51	-15	VII	N
BC,ad	36	51	-15	VIII	N
BD,ac	18	243	-225	IX	N

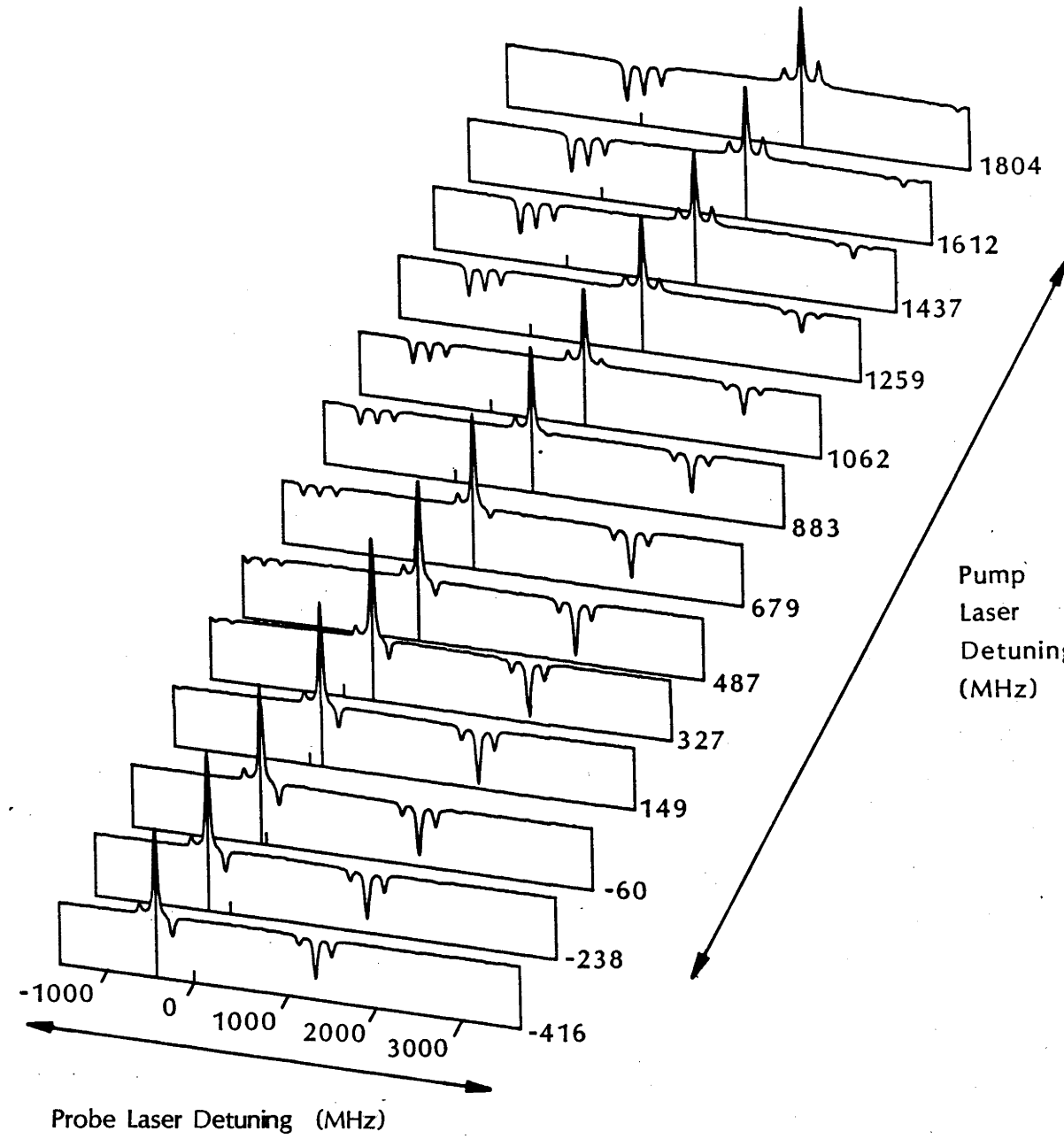

Figure 3.1 A series of co-propagating saturated absorption profiles. Lasers were linearly polarised, with parallel polarisation. The pump power was 0.07 mW giving a calculated Rabi frequency of 10 MHz. The small vertical tic marks on the baseline of each profile indicate the position of zero probe laser detuning. The longer lines from each baseline to the profile indicate the positions of equal pump and probe detuning. The ends of these lines are on a line at 45° to the detuning axes.

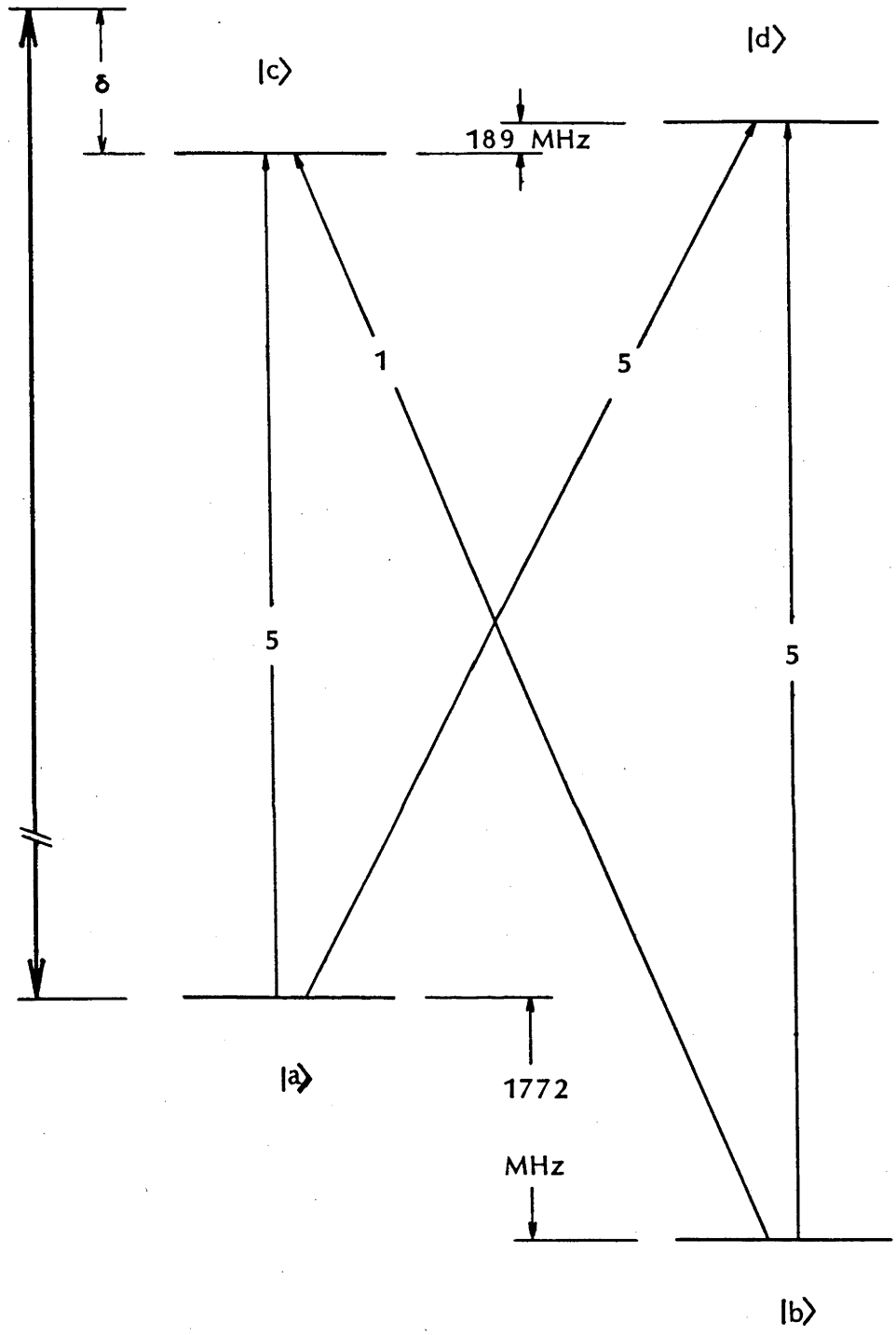

Figure 3.2 Simplified diagram of the Na D_1 transition. The hyperfine splittings of the lower and upper levels are shown to scale, with the level labelling arrangement used throughout this thesis. The relative strengths of the hyperfine transitions are shown. The heavy vertical line represents a laser with a (positive) detuning, δ.

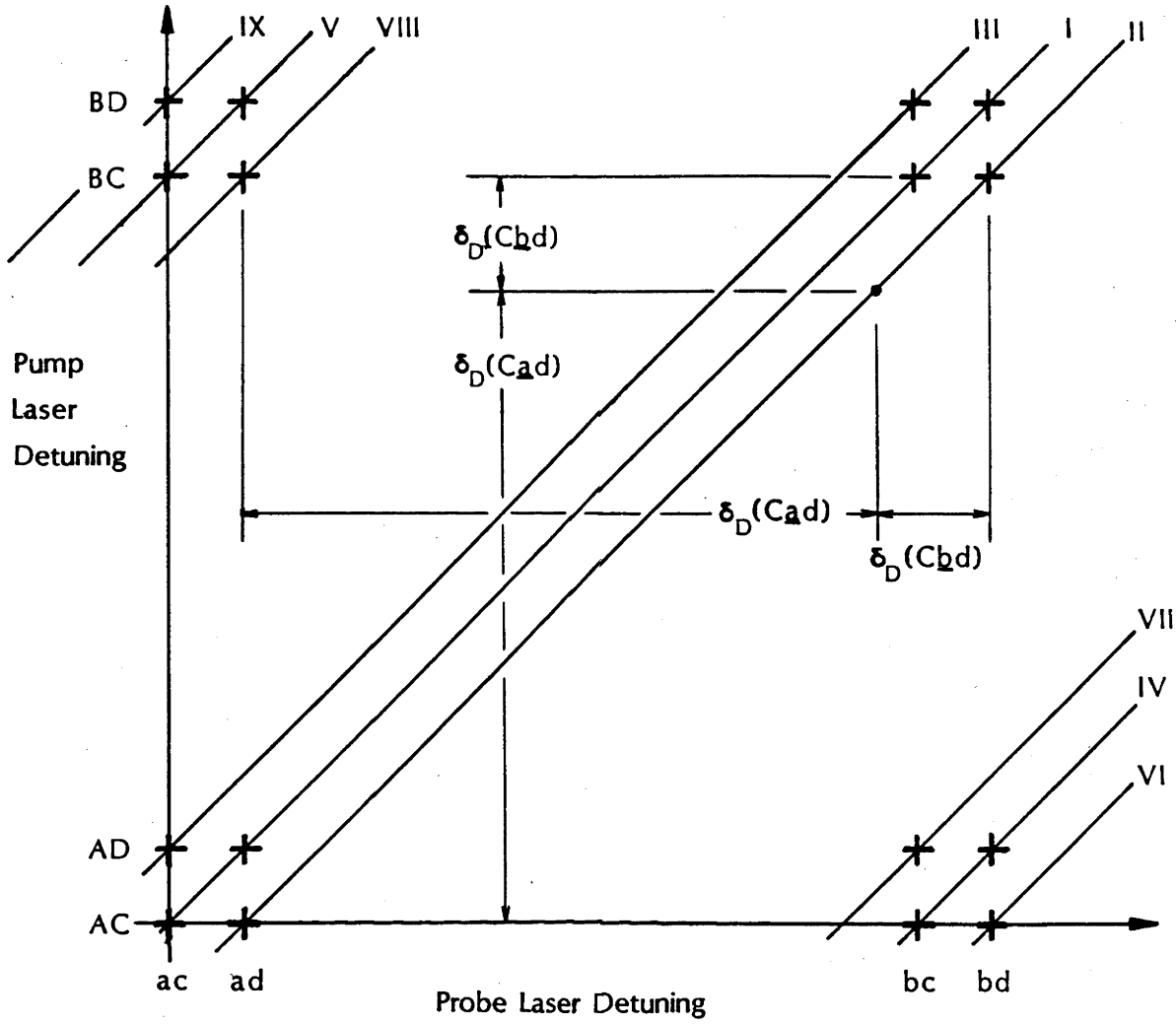

Line	Contributing Resonances	System Type
I	$\underline{ac}$ $\underline{ad}$ $\underline{bc}$ $\underline{bd}$	I
II	$C\underline{a}\bar{d}$ $C\underline{b}\bar{d}$	V
III	$D\underline{a}\bar{c}$ $D\underline{b}\bar{c}$	V
IV	$A\underline{c}\bar{b}$ $A\underline{d}\bar{b}$	Λ
V	$B\underline{c}\bar{a}$ $B\underline{d}\bar{a}$	Λ
VI	$\bar{A}C,\bar{b}d$	N
VII	$A\bar{D},\bar{b}c$	N
VIII	$B\bar{C},\bar{a}d$	N
IX	$B\bar{D},\bar{a}c$	N

Figure 3.3 Origin of features: co-propagating case. Plot of Eq. 3.2 showing the origins of features in the co-propagating profiles. The crosses indicate the positions of resonances in Doppler free profiles and the 45° lines show the pump and probe detunings with at least one velocity sub-group Doppler shifted into resonance. The Doppler detunings of velocity sub-groups contributing to a feature at the position of the dot are also shown, as are the labelling arrangement and contributing system types for the lines.

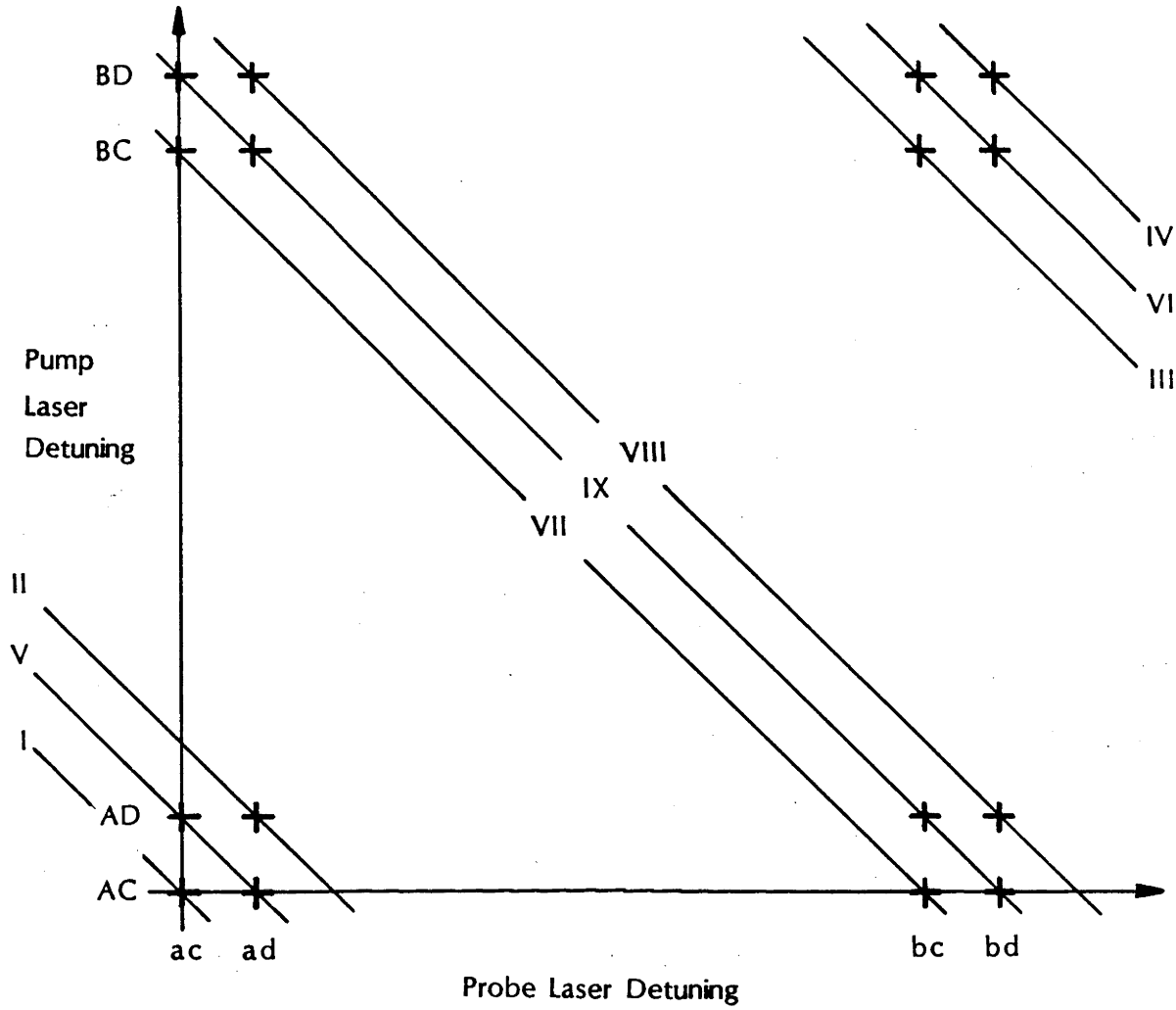

Line	Contributing Resonances	System Type
I	$\underline{ac}$	I
II	$\underline{ad}$	I
III	$\underline{bc}$	I
IV	$\underline{bd}$	I
V	$D\underline{ac}$ $C\underline{ad}$	V
VI	$D\underline{\bar{b}c}$ $C\underline{\bar{b}d}$	V
VII	$B\underline{\bar{c}a}$ $A\underline{\bar{c}b}$	Λ
VIII	$B\underline{\bar{d}a}$ $A\underline{\bar{d}b}$	Λ
IX	BD,ac BC,ad $\bar{A}$D,bc AC,bd	N

Figure 3.4 Origin of features: counter-propagating case. Plot of Eq. 3.2 showing the origins of features in counter-propagating profiles. The crosses indicate the positions of resonances in Doppler free profiles and the -45° lines show the pump and probe detunings with at least one velocity sub-group Doppler shifted into resonance. A standard saturated absorption experiment is represented by a scan along a line at +45°, passing through the origin. The labelling arrangement and contributing system types for the lines in the counter-propagating geometry are shown.

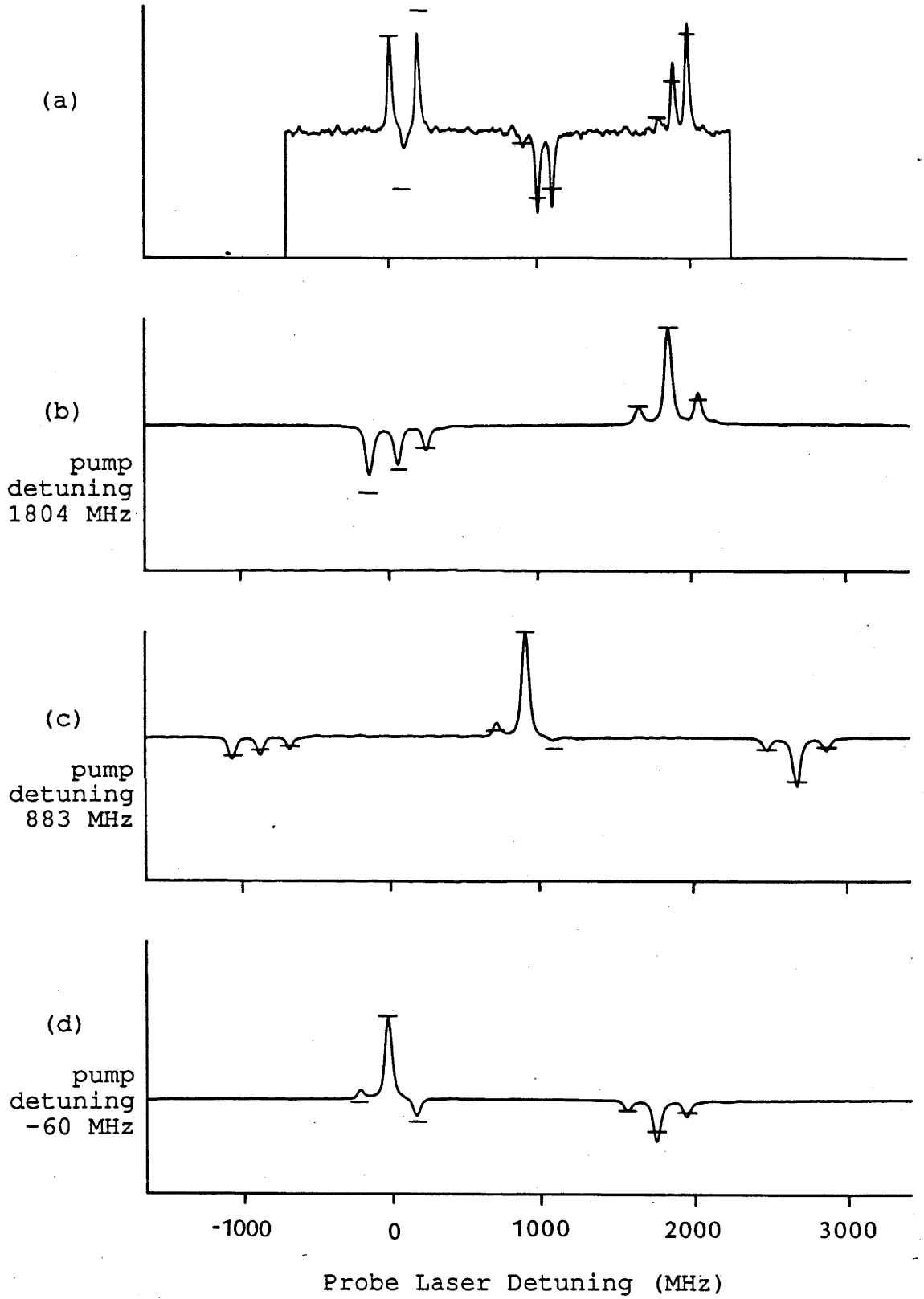

Figure 3.5 Comparison of types of saturated absorption. A standard saturated absorption profile, (a), and co-propagating saturated absorption profiles for various pump laser detunings, (b) to (d). The probe laser detuning range used in the standard saturated absorption experiment was smaller than for profiles (b) to (d) so only the limited range of data is plotted.

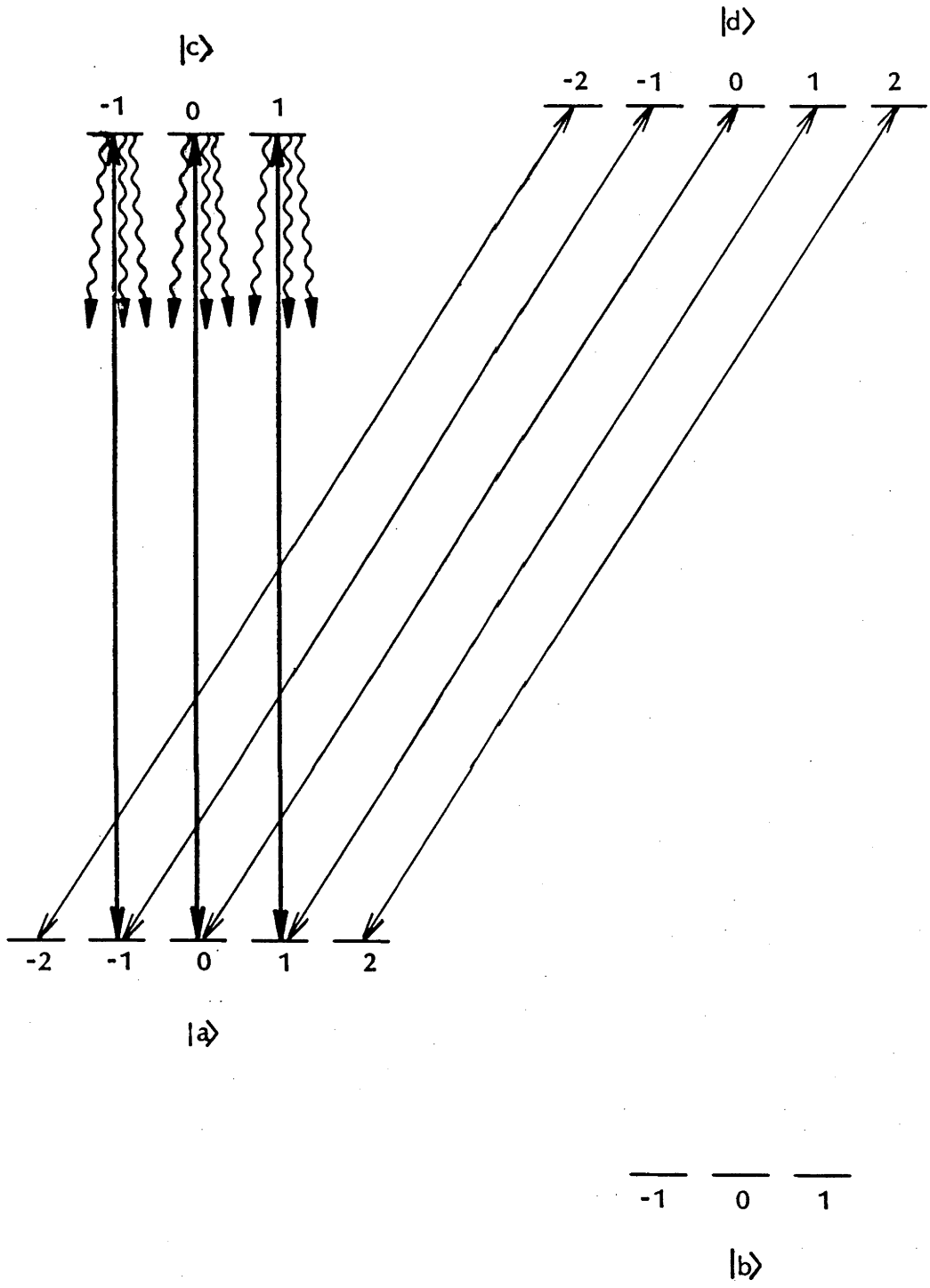

Figure 3.6 Zeeman optical pumping in the Cad resonance. Diagram showing the Zeeman optical pumping action of the linearly polarised pump laser (heavy lines) tuned to the ac transition. Optical pumping increases the populations of the $m_a = \pm 2$ sub-levels. Absorption on the $m = \pm 2$ transitions of the probe laser (fine lines) is enhanced.

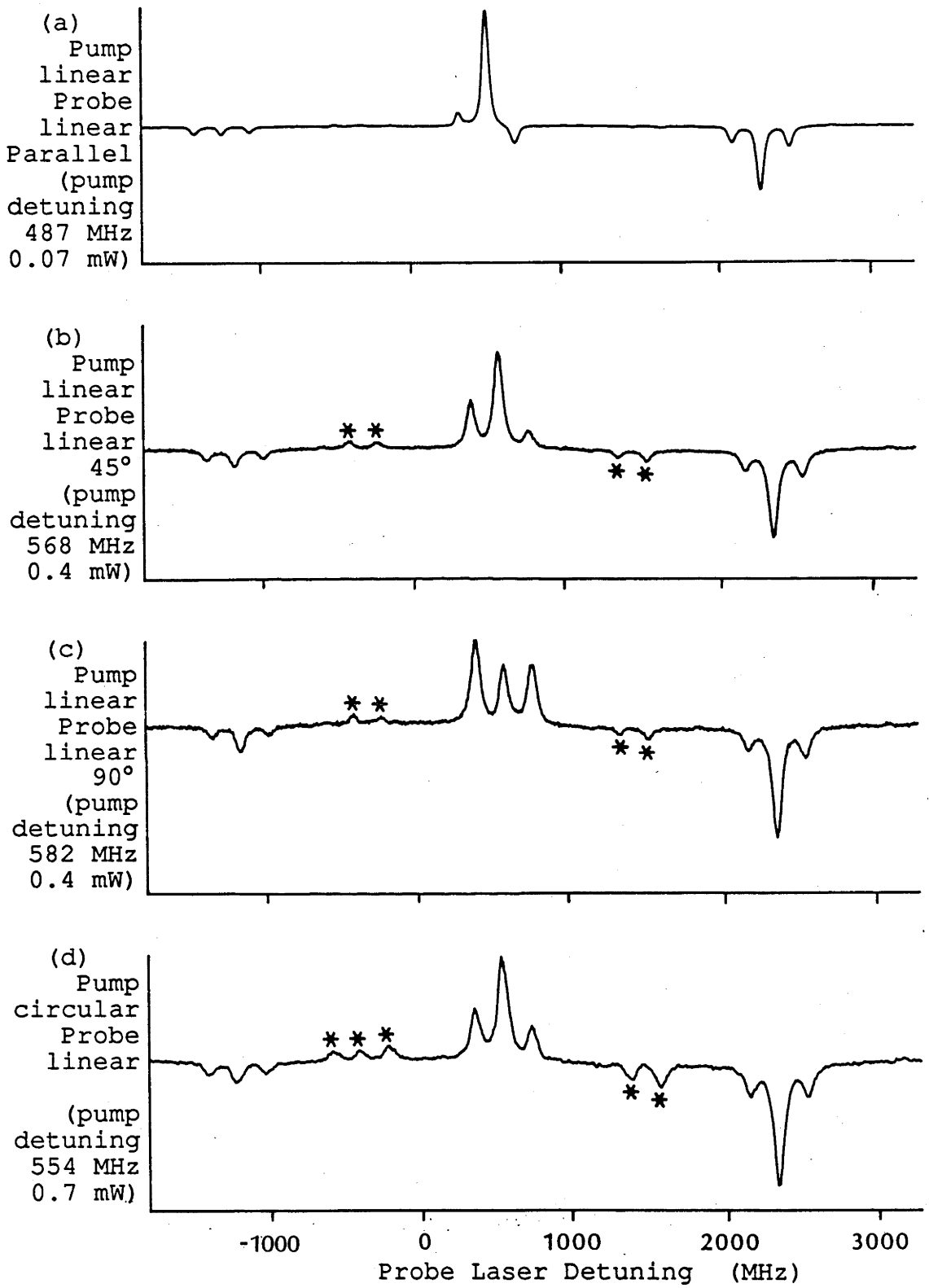

Figure 3.7 Dependence of co-propagating saturated absorption profiles on pump polarisation. The angles between the directions of polarisation for the linearly polarised cases are shown. Features marked with an asterisk in profiles (b) to (d) are due to reflection of a portion of the pump beam from the window back into the vapour. Pump powers are shown.

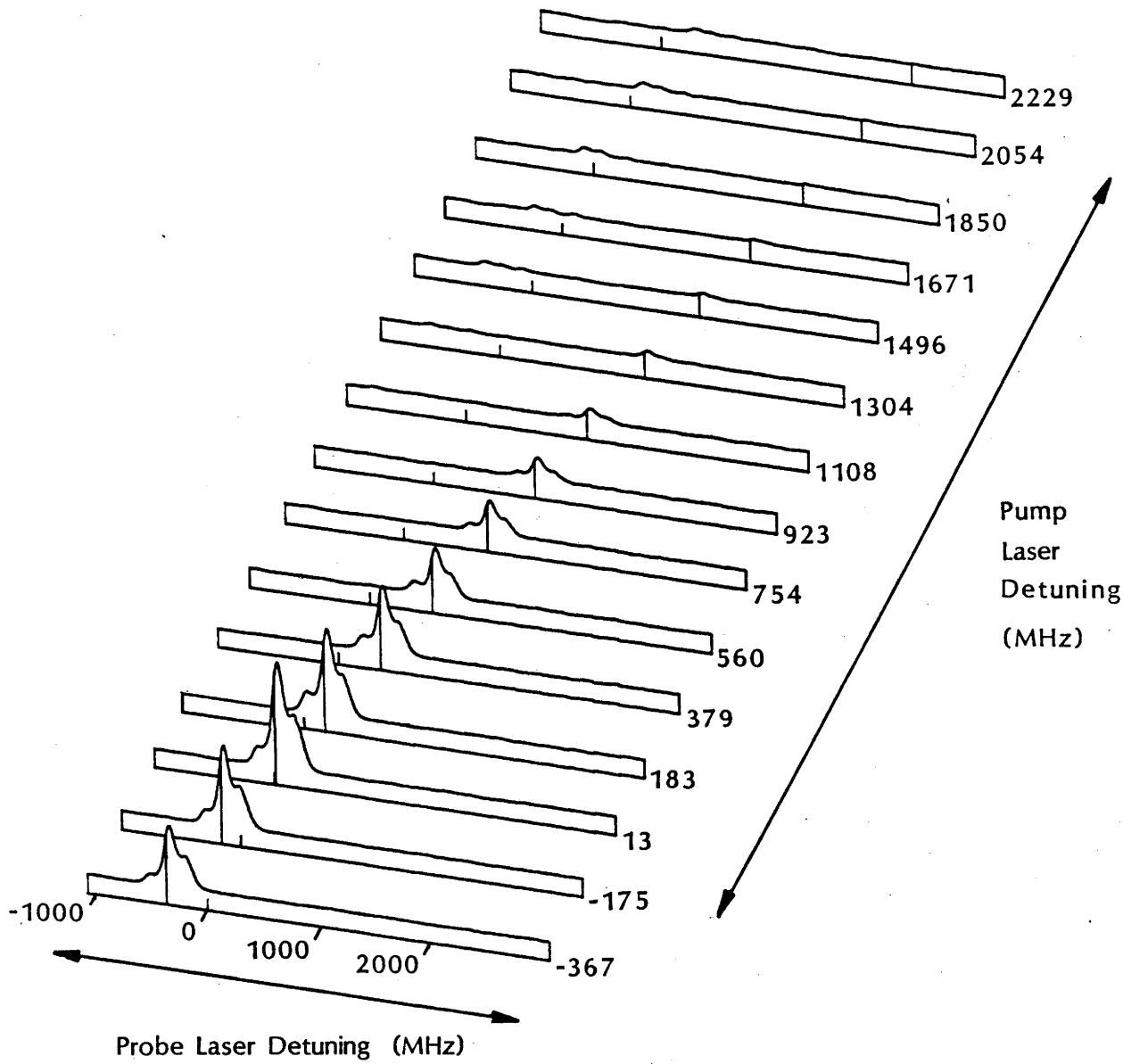

Figure 3.8 A series of co-propagating polarisation spectroscopy profiles: linearly polarised pump. The pump power was 0.6 mW giving a calculated Rabi frequency of 28 MHz. Lasers were both linearly polarised, with 45° between polarisation directions, and the analyser was in the crossed position. The small vertical tic mark on the baseline of each profile indicates the position of zero probe laser detuning. The longer line from each baseline to the profile indicates the position of equal pump and probe detuning. The ends of these lines are on a line at +45° to the detuning axes.

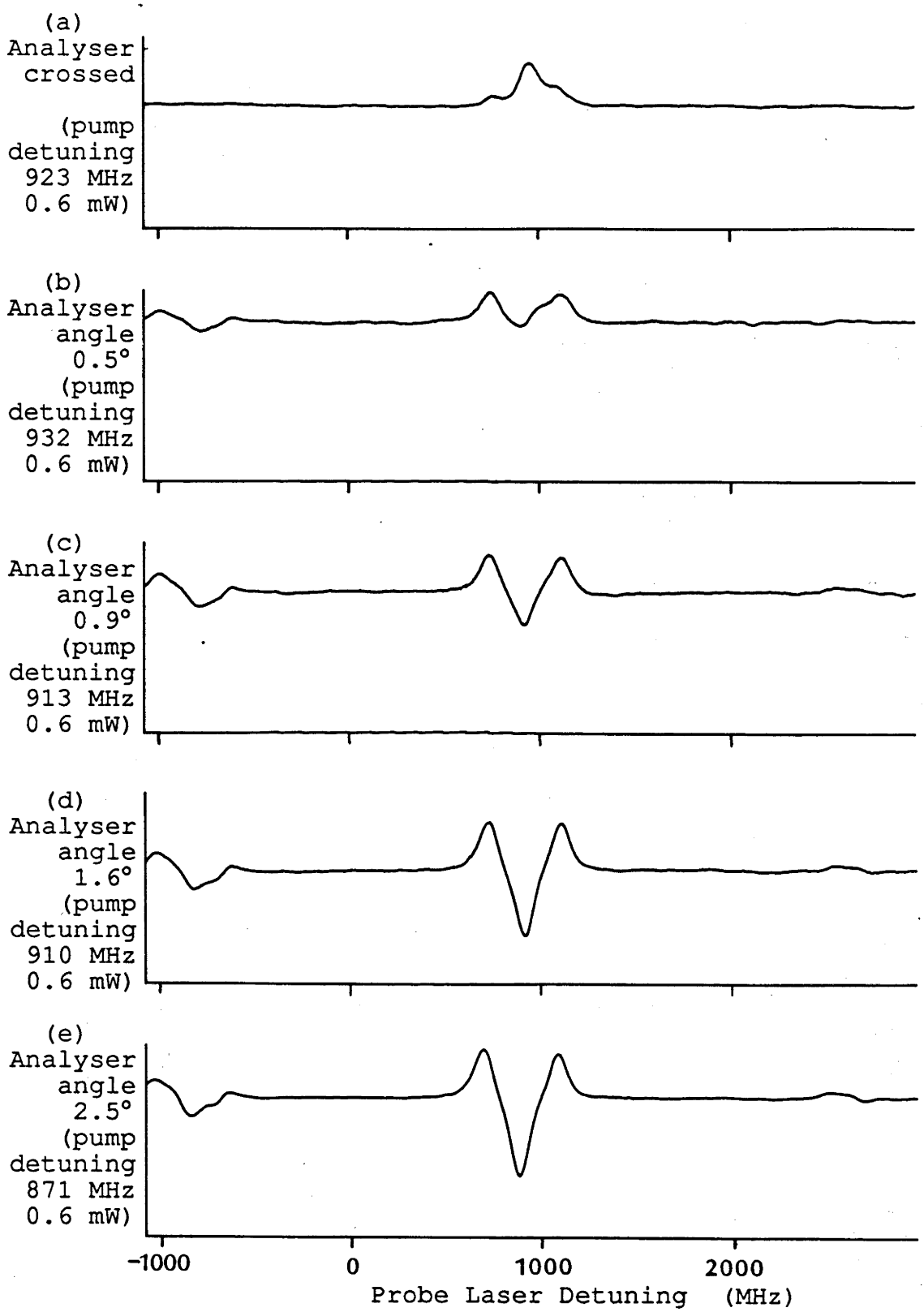

Figure 3.9 Variation of polarisation spectroscopy profiles with analyser orientation. A series of polarisation spectroscopy profiles with linearly polarised lasers with 45° between polarisation directions. Orientations of the analyser are shown relative to the crossed position.

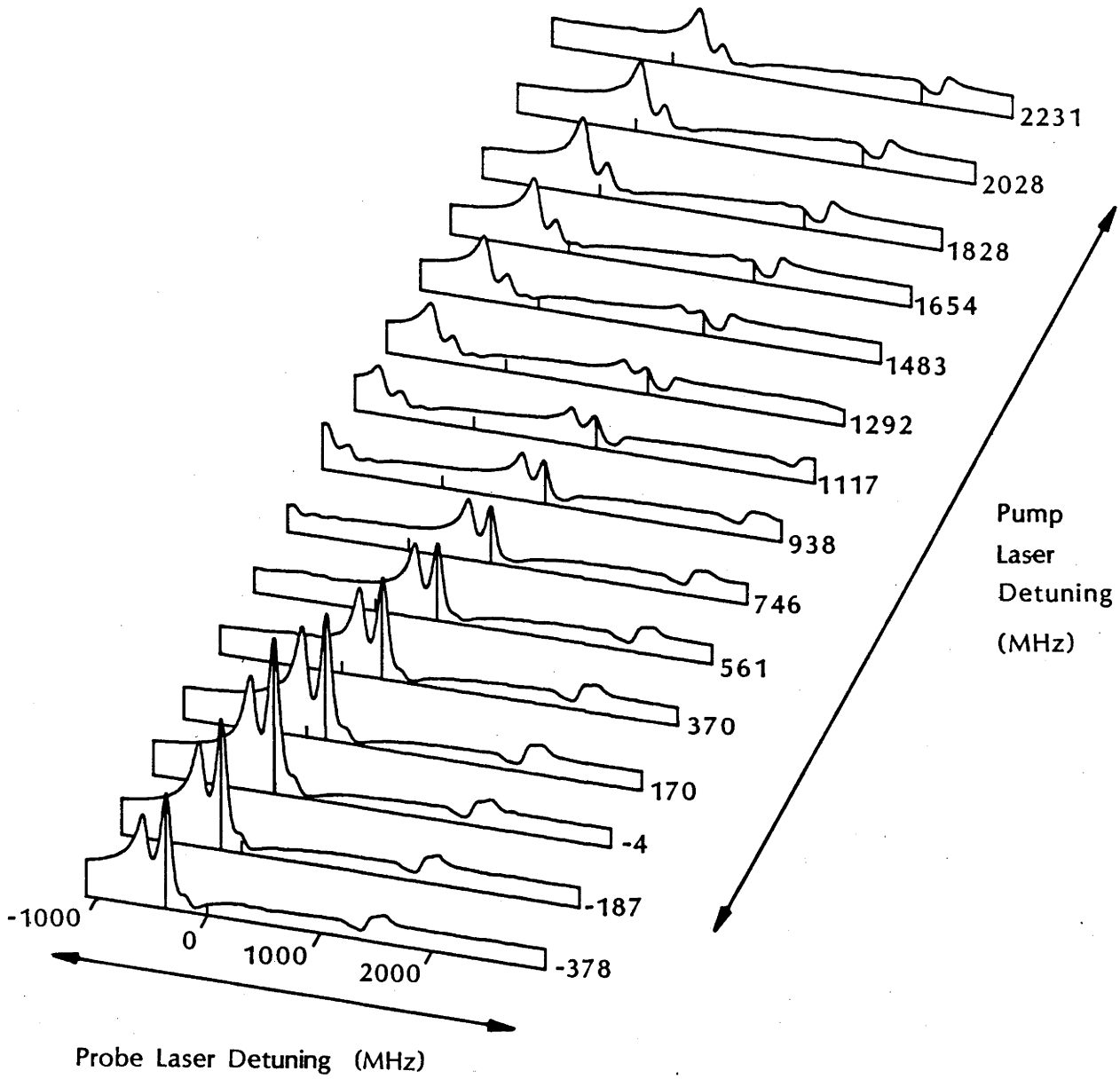

Figure 3.10 A series of co-propagating polarisation spectroscopy profiles: circularly polarised pump. The pump laser was circularly polarised and the probe was linearly polarised, and the analyser was rotated by 1.6° from the crossed position. The pump power was 1.1 mW giving a calculated Rabi frequency of 38 MHz. The small vertical tic mark on the baseline of each profile indicates the position of zero probe laser detuning. The longer line from each baseline to the profile indicates the positions of equal pump and probe detuning. The ends of these lines are on a line at 45° to the detuning axes.

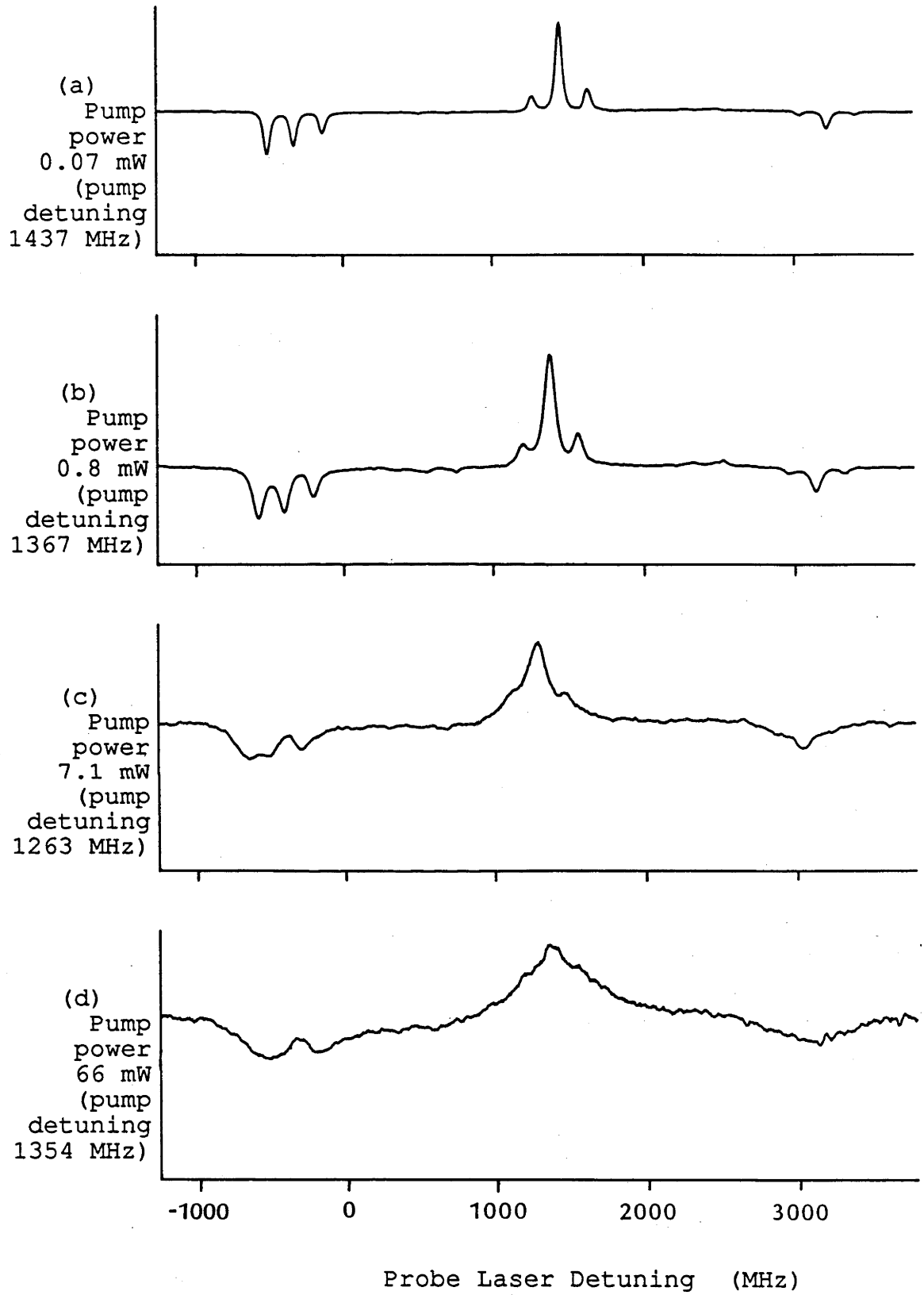

Figure 3.11 Dependence of saturated absorption profiles on pump power. Co-propagating saturated absorption profiles for a range of pump laser powers. Laser powers are estimates accounting for attenuation and scattering in the initial polariser and the windows. The lasers were linearly polarised with parallel polarisation.

Chapter 4. Theoretical Treatment

In common with many theoretical treatments of the interaction of radiation with atoms, a solution of the equation of motion for the density matrix (Liouville equation) is used here.

$$i\hbar \frac{d\rho}{dt} = \left[H,\rho\right] + \text{relaxation terms} \qquad (4.1)$$

where ρ is the density matrix and H is the Hamiltonian. The forced evolution of the density matrix is described by the commutator bracket (i.e. $[H,\rho]$) and all relaxation effects are included in a separate term. The solution of this equation is then used to calculate the polarisation of the atomic medium induced by the fields. The signal detected in the experiment is calculated from the influence of the induced atomic polarisation on the probe laser.

Because of the hyperfine and Zeeman structure of the levels involved, the atomic system is significantly more complicated than the two- or three-state atom commonly assumed in theoretical treatments of this type. However, since the purpose of the work is to attempt to develop an understanding of an extended system such as this, no simplifying assumptions about the level system are made.

The atomic medium used in the experiment was a Doppler broadened vapour. Atomic motion effects are therefore included in the theoretical treatment. This is done by

dividing the velocity distribution into velocity sub-groups which are assumed to be independent. The Doppler effect can be included at the end of the calculation by summing the weighted contributions of the velocity sub-groups, accounting for the Doppler shifted detunings of the two laser fields.

The theoretical treatment begins with a derivation of the solution of the Liouville equation in Section 4.1. This derivation is kept as general as possible. The diagrammatic representation of the power series solution is also described, along with the assumptions made in treating the two laser problem. Application of the solution to the extended atomic level system is outlined in Section 4.2, while the treatment of the Doppler effect and calculation of the signal are presented in Sections 4.3 and 4.4 respectively. Results of the calculations are presented in the following chapter.

4.1 Solution of the Liouville equation

Figure 4.1 shows the hyperfine levels and Zeeman sub-levels that make up the D_1 transition of sodium. The level labelling convention introduced in Chapter 3 is also shown, along with the hyperfine splitting in both upper and lower levels. Natural linewidths and cross-relaxation rates that are necessary in the description of relaxation effects are included.

There are sixteen states in the level system so there are 256 components of the density matrix. Clearly, a solution of the Liouville equation that takes all states into account will require extensive computer calculations as an analytical solution will be intractable. To keep the computer time requirements to a minimum, the solution must be extremely efficient.

The diagrammatic solution of Ben-Reuven and Klein (Ben-Reuven and Klein 1971, Klein et al 1974, Rabin and Ben-Reuven 1979) is chosen here. A simple expression for the component of the density matrix oscillating at the frequency of the probe field is derived in terms of operators representing field interaction and atomic relaxation. The expression can be evaluated numerically using matrix representations of the operators on the chosen basis.

The complete density matrix of the system comprises an atomic part and a field part and a basis is chosen that represents the two components in an outer product form. Interaction between the fields and a single atom is assumed to have negligible effect on the fields. With this assumption, the field component of the density matrix can be treated by considering only the small changes to the photon number of each mode during the interaction. Since the fields are generated by lasers well above threshold, this assumption is expected to be well satisfied. Fisk (Fisk 1985, Fisk et al 1986b) has shown that when the fields are treated as coherent states, the same representation of the field

component is applicable.

The Liouville equation is solved by representing the density matrix in Liouville space (see Dalton 1982, Appendix 1 for a description of Liouville space). The elements of Liouville space are operators acting on states in Hilbert space and the basis for the Liouville space is defined in terms of the basis states $|i\rangle$ of the Hilbert space:

$$|if^{\dagger}\rangle\rangle = |i\rangle\langle f| \qquad (4.2)$$

The "double-ket" notation is used to emphasise that these are elements of a vector space. If the states i and f have parities π_i and π_f respectively, the Liouville space ket $|if^{\dagger}\rangle\rangle$ has parity $\pi_i\pi_f$ (Ben-Reuven 1966). This means that the Liouville space may be divided into even parity and odd parity sub-spaces. If, for example, states $|i\rangle$ and $|f\rangle$ are connected by electric dipole allowed transitions then $|if^{\dagger}\rangle\rangle$ is part of the odd parity sub-space. The scalar product in Liouville space is defined in terms of the trace in Hilbert space:

$$\langle\langle A|B\rangle\rangle = \mathrm{tr}(A^{\dagger}B) \qquad (4.3)$$

The nonlinear response of the system to the monochromatic driving fields is expected to be a series of harmonics of the driving frequencies. The density matrix is

therefore expanded in terms of these harmonics.

$$\rho(t) = \sum_{i,f} \sum_{\underset{\sim}{n}} \rho_{if}^{(\underset{\sim}{n})}(t) \; |if^{\dagger};\underset{\sim}{n}>> \; e^{-i\,\underset{\sim}{n}.\underset{\sim}{\omega}\,t} \tag{4.4}$$

The Liouville space basis Eq. 4.2 is extended to include the "harmonics number vector" $\underset{\sim}{n}$ which indicates the field harmonic since it is defined by

$$\underset{\sim}{n}.\underset{\sim}{\omega} = \Sigma n_{\eta}\omega_{\eta} \qquad n_{\eta} = 0,\pm1,\pm2,... \tag{4.5}$$

where ω_{η} is the frequency of field η. This means, for example, that $\underset{\sim}{n}$ = (0,2,0,0,...) represents the first harmonic (i.e. twice the fundamental) of field number two. Using this representation, the time derivative of the density matrix is given by

$$\begin{aligned}\dot{\rho}(t) = &\sum_{i,f} \sum_{\underset{\sim}{n}} \dot{\rho}_{if}^{(\underset{\sim}{n})}(t) \; |if^{\dagger};\underset{\sim}{n}>> \; e^{-i\,\underset{\sim}{n}.\underset{\sim}{\omega}\,t} \\ &-i\sum_{i,f} \sum_{\underset{\sim}{n}} \underset{\sim}{n}.\underset{\sim}{\omega}\,\rho_{if}^{(\underset{\sim}{n})}(t) \; |if^{\dagger};\underset{\sim}{n}>> \; e^{-i\,\underset{\sim}{n}.\underset{\sim}{\omega}\,t}\end{aligned} \tag{4.6}$$

To solve the Liouville equation it is written entirely in terms of operators in Liouville space. The commutator bracket with the Hamiltonian is expressed as the Liouvillian, L

$$L|X>> = \hbar^{-1}[H,X] \tag{4.7}$$

where X is any Hilbert space operator.

In an interaction picture with respect to the radiation fields, the Hamiltonian consists of an atomic part and an interaction part. The atomic part is given by

$$H_a|i> = E_i|i> \tag{4.8}$$

where E_i is the energy of atomic level $|i>$. The matrix elements of the atomic part of the Liouvillian on the basis Eq. 4.2 are atomic resonance frequencies. In the interaction picture under the dipole approximation the interaction part is

$$H_i = -\underset{\sim}{\mu}\cdot\underset{\sim}{E} = -\tfrac{1}{2}\,\underset{\sim}{\mu}\cdot\sum_{\eta}\left[\underset{\sim}{E}_{\eta}^{(+)}\, e^{-i\omega_\eta t} + \underset{\sim}{E}_{\eta}^{(-)}\, e^{i\omega_\eta t}\right] \tag{4.9}$$

where the vector $\underset{\sim}{\mu}$ is the atomic dipole moment. The electric field, $\underset{\sim}{E}$, has been divided into positive and negative frequency parts and the factor of 1/2 included to allow the amplitudes of the two components to equal the amplitude of the total field.

It can be seen from Eq. 4.4 that the interaction Hamiltonian changes the harmonics number vector by ±1 for each field. The operation of the interaction Hamiltonian is expressed by its effect on the basis vectors $|if^{\dagger};\underset{\sim}{n}>>$ which

includes the change of the harmonics number vector in addition to the effects on the atomic components. Using this change to $\underset{\sim}{n}$ to keep track of the field harmonics, the explicit time dependence of the interaction term can be eliminated.

The positive and negative frequency parts of the field are associated with absorption and stimulated emission respectively. This can be seen most easily from the expression for the quantised electromagnetic field where the positive frequency part contains a photon destruction operator and the negative frequency part a photon creation operator (see, for example, Haken 1981, Chap. 5).

Through the interaction Hamiltonian (Eq. 4.9) and the harmonic expansion of the density matrix, the two parts are also associated with an increase and decrease respectively of a harmonics number vector component. The harmonics number vectors in the Liouville space basis states (Eq. 4.4) are therefore associated with the electric fields. They are used as the basis for the field space when the density matrix is separated into the field and atomic components. The harmonic expansion (Eq. 4.4) is the reason for the dual function of the harmonics number representation. The complete basis is written as an outer product of the atomic basis states and the harmonics number basis states.

$$|if^{\dagger};\underset{\sim}{n}>> = |if^{\dagger}>>\otimes|\underset{\sim}{n}>> \qquad (4.10)$$

The harmonics numbers keep track of photons absorbed from or added to the fields during the evolution of the density matrix.

The equation of motion for the density matrix now has the form:

$$i\frac{d}{dt}\left(\delta\rho(t)\right) + \left(\underset{\sim}{n}.\underset{\sim}{\omega}I - L_a - \Sigma - U\right)\delta\rho(t) = U\rho_e \qquad (4.11)$$

where I is the unit operator and U is the Liouville space equivalent of the interaction Hamiltonian. L_a is the atomic Liouvillian, derived from Eq.4.8. The relaxation terms have been incorporated into the "self energy insertion" (Rabin and Ben-Reuven 1979) represented by the operator Σ. Expressions for these operators are given later in this chapter, when this technique is applied to the extended level system used to describe the sodium D_1 line.

The density matrix has been split into the equilibrium value, ρ_e, and the time dependent part, $\delta\rho(t)$, induced by the driving fields. This is done to allow a homogeneous boundary condition, anticipating the solution using Green's functions. The equilibrium density matrix satisfies the Liouville equation, Eq. 4.1, in the absence of the driving fields. This has been used to eliminate several terms from Equation 4.11.

Using Green's functions, the solution of this equation is written as

$$\delta\rho(t) = \int_{t_0}^{t_1} \hat{g}(t,t')\, U \rho_e \, dt' \qquad t_0<t<t_1 \tag{4.12}$$

where the Green's function satisfies the equation and boundary condition

$$i\frac{d\hat{g}(t,t')}{dt} + (\underset{\sim}{n}\cdot\underset{\sim}{\omega}I - L_a - \Sigma - U)\,\hat{g}(t,t') = \delta(t-t')$$

$$\hat{g}(t_0,t') = 0 \tag{4.13}$$

The time dependent Green's function has been written as a lower case letter so the frequency dependent version may be written as the more common G. The solution of this equation is

$$\hat{g}(t,t') = -i\theta(t-t')e^{i(\underset{\sim}{n}\cdot\underset{\sim}{\omega}I - L_a - \Sigma - U)(t-t')} = \hat{g}(t-t') \tag{4.14}$$

Because of the step function $\theta(t-t')$ in the Green's function, the upper limit of integration in Eq. 4.12 can be set to ∞. To evaluate the integral, the initial time, t_0, is set to $-\infty$. This implies that the system is assumed to have reached steady state because the beginning of the interaction was sufficiently long ago that any transient effects that occurred have died out. Using this approximation, the

integral in Eq. 4.12 is given by (Rabin and Ben-Reuven 1979)

$$\int_{-\infty}^{\infty} \hat{g}(t-t')\,dt' = (\underset{\sim}{n}\cdot\underset{\sim}{\omega}I+i\varepsilon-L_a-\Sigma-U)^{-1} = \hat{G}(\underset{\sim}{n}\cdot\underset{\sim}{\omega}) \qquad (4.15)$$

where the limit $\varepsilon\rightarrow 0+$ is taken.

The expansion of the density matrix in terms of the field harmonics (Eq. 4.4) is now used to select the component oscillating at a particular harmonic frequency, $\underset{\sim}{m}\cdot\underset{\sim}{\omega}$. This is done by taking an inner product between the Liouville space bra representing the desired frequency and the Liouville space ket representing the density matrix. Using Equations 4.12 and 4.15 the component of the density matrix oscillating at frequency $\underset{\sim}{m}\cdot\underset{\sim}{\omega}$ is given by

$$|\rho(\underset{\sim}{m}\cdot\underset{\sim}{\omega})>> = <<\underset{\sim}{m}|\hat{G}U|\rho_e>> \qquad (4.16)$$

This component is essentially equivalent to one of the harmonics components of the expansion Eq. 4.4, although it represents the sum over all the atomic parts in one symbol.

The density matrix Eq 4.16 is expanded in a power series in the applied fields by expressing the Green's function, $\hat{G}(\underset{\sim}{n}\cdot\underset{\sim}{\omega})$, in terms of linear response Green's functions, $G(\underset{\sim}{n}\cdot\underset{\sim}{\omega})$, separating out the interaction operator, U

$$\hat{G}(\underset{\sim}{n}.\underset{\sim}{\omega}) = \left[G(\underset{\sim}{n}.\underset{\sim}{\omega})^{-1} - U\right]^{-1}$$
$$= \left[I - G(\underset{\sim}{n}.\underset{\sim}{\omega})U\right]^{-1} G(\underset{\sim}{n}.\underset{\sim}{\omega}) \qquad (4.17)$$
$$= G(\underset{\sim}{n}.\underset{\sim}{\omega}) + G(\underset{\sim}{n}.\underset{\sim}{\omega})UG(\underset{\sim}{n}.\underset{\sim}{\omega}) + G(\underset{\sim}{n}.\underset{\sim}{\omega})UG(\underset{\sim}{n}.\underset{\sim}{\omega})UG(\underset{\sim}{n}.\underset{\sim}{\omega}) + \ldots$$

The linear response Green's functions are given by

$$G(\underset{\sim}{n}.\underset{\sim}{\omega}) = (\underset{\sim}{n}.\underset{\sim}{\omega}I + i\varepsilon - L_a - \Sigma)^{-1} \qquad (4.18)$$

The harmonics number space can be separated into odd and even sub-spaces. A harmonics number ket $|\underset{\sim}{n}>>$ is considered to be an element of the even (odd) sub-space if Σn_η is even (odd). The field interaction operators, U_η, are made up of an harmonics number space part and an atomic space part. As mentioned earlier, the harmonics number part changes the harmonics number n_η of a Liouville space state by ± 1 and hence changes an element of the odd sub-space to the even and vice versa. Similarly, the atomic part of the interaction operator is the dipole moment which couples Liouville space states of opposite parity.

The combined atomic and field space kets may be considered as being even (odd) if they are made up of even (odd) atomic parity and harmonics number sub-space parts. Combinations of odd with even do not occur. This is because the equilibrium density matrix on which $\hat{G}U$ operates (Eq. 4.16) consists of an even parity atomic part (the equilibrium population distribution) and an even harmonics

number part ($|\underset{\sim}{0}>>$). Because the interaction operator links both harmonics number and atomic states from different sub-spaces, opposite combinations cannot be generated. The Green's functions in the power series solution Eq. 4.17 therefore alternate between the odd and even sub-spaces.

Equations 4.16 and 4.17 can be resummed with the help of a diagrammatic representation. A frequency component of the density matrix derived from these two equations is the sum of all possible GU pairs operating on the equilibrium density matrix on the right and ending at the desired harmonic on the left. Because the equilibrium density matrix has a harmonics number ket component, $|\underset{\sim}{0}>>$, and the $<<\underset{\sim}{m}|$ bra appears on the left, the expression is a harmonics number matrix element. The harmonics number matrix elements that appear at intermediate stages in the series can be easily written down. To see this, consider, for example, the expansion of the second term of the series

$$<<\underset{\sim}{m}|GUGU|\underset{\sim}{0}>> = \sum_{\underset{\sim}{n},\underset{\sim}{n}',\underset{\sim}{n}''} <<\underset{\sim}{m}|G|\underset{\sim}{n}''>><<\underset{\sim}{n}''|U|\underset{\sim}{n}'>><<\underset{\sim}{n}'|G|\underset{\sim}{n}>><<\underset{\sim}{n}|U|\underset{\sim}{0}>> \tag{4.19}$$

Since the linear response Green's functions are diagonal in the harmonics number space, $\underset{\sim}{n}=\underset{\sim}{n}'$ and $\underset{\sim}{n}''=\underset{\sim}{m}$ and since the interaction operators, U, change the harmonics number by ± 1 for each field mode, the possible values of $\underset{\sim}{n}$ are further restricted. The diagram is drawn to indicate explicitly the harmonics number matrix elements at each stage of the expansion.

Before drawing the diagram, it is necessary to consider the particulars of the physical system. The experiments considered here involved two field modes, a weak probe, $\underset{\sim}{E}_1$, and a strong pump field, $\underset{\sim}{E}_2$. The harmonics number vectors therefore have two components: $\underset{\sim}{n} = (n_1,n_2)$. The required frequency component of the density matrix is determined by the signal that is measured in the experiment. Modifications to the probe field polarisation or intensity are caused by the component that oscillates at the probe frequency and therefore $\underset{\sim}{m}$ is chosen to be (1,0) in this case. Since the probe field is weak, only one interaction with the probe field during the evolution of the density matrix is considered. This means that n_1 may only take values of 0 or 1 in the diagram.

If the transitions are assumed to be well separated (i.e. with separations much greater than linewidths) then only certain Green's functions need be considered. From Eq. 4.18 it can be seen that only Green's functions where $\underset{\sim}{n}.\underset{\sim}{\omega} - \omega_{ab}$ (where ω_{ab} is an atomic resonance frequency) is small are important. For the four level system shown in Figure 4.1 the resonant Green's functions are restricted to the set

$$n_1 + n_2 = 0 \text{ or } \pm 1$$

The diagrammatic representation, Figure 4.2, represents all possible combinations of GU that start at $|\rho_e;\underset{\sim}{0}>>$ on the right and end at $<<1,0|$ on the left, subject to the restraints on the harmonics numbers. Field interaction operators, U_1 and U_2, corresponding to the probe and pump fields respectively, are represented by straight lines and harmonics number matrix elements of Green's functions are represented by circles. The harmonics number matrix elements at each stage of the expansion (c.f. Eq. 4.19) are indicated by the number pairs inside the circles.

The diagram represents an operator on the atomic space since the harmonics number matrix elements have already been taken. Because the power series solution (Eq. 4.17) includes arbitrary numbers of GU pairs, the diagram must be interpreted as representing paths of all possible lengths that start at any (0,0) and end at (1,0). Thus, for example, the simplest path $G(1,0)U_1G(0,0)$ must be included.

The purpose of the diagram is to allow the density matrix (Eq. 4.16) to be expressed in a closed form. To do this, the repeating units labelled X, Y and Z in the diagram are identified. The possible paths through the diagram from right to left may be divided along the dashed line. Those below the line include the sum of all possible X units followed by a U_1

$$U_1(I+X+XX+XXX+\ldots) = U_1(I-X)^{-1} \qquad (4.20)$$

while the others represent arbitrarily many X units, followed by a Z and then all possible Y units followed by a U_2

$$U_2(I+Y+YY+YYY+...)Z(I+X+XX+XXX+...) = U_2(I-Y)^{-1}Z(I-X)^{-1} \tag{4.21}$$

The required expression for the density matrix is the sum of both paths

$$|\rho(\omega_1)>> = G(1,0)[U_1(I-X)^{-1} + U_2(I-Y)^{-1}Z(I-X)^{-1}]|\rho_e>> \tag{4.22}$$

The component of atomic polarisation oscillating at the frequency of the probe laser is derived from the density matrix

$$\begin{aligned} \underset{\sim}{P}(\omega_1) &= N/V \; tr(\underset{\sim}{\mu}\rho(\omega_1)) \\ &= N/V \; <<\underset{\sim}{\mu}|\rho(\omega_1)>> \end{aligned} \tag{4.23}$$

where N/V is the atomic number density and $\underset{\sim}{\mu}$ is the dipole moment operator.

The polarisation calculated in Eq. 4.23 is used as a source term in Maxwell's equations to find the influence of the medium on the probe field and subsequently the signal measured in the experiment. The wave equation for the electric field, $\underset{\sim}{E}$, in the medium is

$$\nabla^2 \underset{\sim}{E} - \frac{1}{c^2}\frac{\partial^2 \underset{\sim}{E}}{\partial t^2} = \mu_0 \frac{\partial^2 \underset{\sim}{P}}{\partial t^2} \tag{4.24}$$

Both the field and the polarisation are assumed to be complex time harmonic plane waves.

$$\begin{aligned} \underset{\sim}{E} &= E_x(z)e^{i(\omega t-kz)}\underset{\sim}{e}_x + E_y(z)e^{i(\omega t-kz)}\underset{\sim}{e}_y \\ \underset{\sim}{P} &= P_x(z)e^{i(\omega t-kz)}\underset{\sim}{e}_x + P_y(z)e^{i(\omega t-kz)}\underset{\sim}{e}_y \end{aligned} \tag{4.25}$$

Substituting into Eq. 4.24 and neglecting second derivatives with respect to z (since the field is assumed to vary slowly over distances comparable to the wavelength) gives a simple equation for the field

$$\frac{\partial \underset{\sim}{E}}{\partial z} = \frac{-i\mu_0 \omega c}{2}\ \underset{\sim}{P} \tag{4.26}$$

with boundary condition $\underset{\sim}{E}(0) = \underset{\sim}{E}_1$. The solution to this equation can be written in terms of a small "signal field", $\underset{\sim}{E}_s$, which is generated by the atomic polarisation and is added to the probe field (see Levenson 1982 Chap. 2).

4.2 Application to the extended system

To evaluate the induced atomic polarisation (Eq. 4.23) a basis for the atomic space is required. The Liouville space operators and states are then expressed as matrices and vectors respectively and the necessary calculations are performed by computer. Because the relaxation processes are spherically symmetric, irreducible tensor components are used

for the basis. For a review of irreducible tensor components of the density matrix see Omont (1977). To emphasise that they are basis vectors in Liouville space the double ket notation is retained (Ben-Reuven 1966) in preference to the more commonly used ${}_{if}\rho^{k}_{q}$ notation (Ducloy 1973).

$$
\begin{aligned}
|if^{\dagger};K,Q>> &= \sum_{m_i m_f} (-1)^{F_f - m_f} <F_i,F_f,m_i,-m_f|K,Q> \; |i,m_i\,(fm_f)^{\dagger}>> \\
&= \sum_{m} (-1)^{F_f + Q - m} <F_i,F_f,m,Q-m|K,Q> \; |i,m\,(f,m-Q)^{\dagger}>>
\end{aligned}
\tag{4.27}
$$

Messiah's (1961) notation for Clebsch-Gordan coefficients has been used. The labels i and f indicate atomic levels and represent the principal quantum numbers, while F is the total angular momentum quantum number of the level and m is the projection along the quantisation axis. K=0 components are proportional to populations, the K=1 components are standard components of orientation and K=2 components are the standard components of alignment. Components of the form $|ii^{\dagger};K,0>>$ are related to the populations of Zeeman sub-levels and $|ii^{\dagger};K,Q>>$ (Q non-zero) depend on Zeeman coherences.

To treat laser fields of arbitrary polarisation, the vector nature of both the fields and the atomic dipole moment must be retained. Since the interaction Liouvillian consists of a dot product between the dipole moment and the field, it is necessary to use a vector expansion that is compatible with the irreducible tensor representation used for the Liouville space states. Vectors are therefore expanded in

terms of the spherical basis vectors

$$\underset{\sim}{e}_{\pm} = \frac{\mp 1}{2}\left(\underset{\sim}{e}_x \pm i\underset{\sim}{e}_y\right)$$
$$\underset{\sim}{e}_0 = \underset{\sim}{e}_z \qquad (4.28)$$

where $\underset{\sim}{e}_x$, $\underset{\sim}{e}_y$ and $\underset{\sim}{e}_z$ are Cartesian basis vectors. This representation is used both for the fields and the dipole moment operator.

Having chosen the basis sets, it is now necessary to expand the operators, states and vectors in terms of the respective basis elements. From Eq. 4.22 it can be seen that expressions for the equilibrium density matrix, $|\rho_e>>$, the linear response Green's functions, $G(n_1,n_2)$, the field interaction operators, U_η, and the dipole moment, $<<\underset{\sim}{\mu}|$, are required.

If all Zeeman sub-levels of the two lower levels, $|a>$ and $|b>$, are assumed to be equally populated at equilibrium, $|\rho_e>>$ is given by

$$|\rho_e>> = (2F_a+1+2F_b+1)^{-1}[\sqrt{2F_a+1}\,|aa^\dagger;0,0>>+\sqrt{2F_b+1}\,|bb^\dagger;0,0>>]\otimes|0,0>> \qquad (4.29)$$

The Green's function matrix elements, $G(n_1,n_2)$, are also easy to evaluate from Equation 4.18. The matrix elements of the Liouvillian, L, are resonance frequencies of the

transitions

$$<<if^{\dagger};K',Q'|L|kg^{\dagger};K,Q>> = \omega_{kg}\delta_{ik}\delta_{fg}\delta_{KK'}\delta_{QQ'}$$
$$= \hbar^{-1}(E_k-E_g)\delta_{ik}\delta_{fg}\delta_{KK'}\delta_{QQ'} \quad (4.30)$$

The matrix elements of Σ are relaxation and cross-relaxation rates of the atomic populations and coherences. Σ is diagonal in K and Q and independent of Q (Klein et al 1974) so the representation of Σ on the irreducible tensor basis is much simpler than it would be on the Zeeman sub-level basis, $|i,m_i(j,m_j)^{\dagger}>>$. Since collisions are absent, diagonal elements of Σ are related to the natural widths, γ, of the levels

$$<<if^{\dagger};K,Q|\Sigma|if^{\dagger};K,Q>> = -i\tfrac{1}{2}(\gamma_i+\gamma_f) \quad (4.31)$$

Off-diagonal elements for populations and Zeeman coherences are cross-relaxation rates i.e. the transfer rate from one level to another. For spontaneous emission with an irreducible tensor representation, these rates were derived by Ducloy and Dumont (1970)

$$<<ii^{\dagger};K,Q|\Sigma|ff^{\dagger};K,Q>> = -i(-1)^{F_i+F_f+K+1}(2F_f+1)\begin{Bmatrix} F_f & F_f & K \\ F_i & F_i & 1 \end{Bmatrix}\gamma_{fi} \quad (4.32)$$

where the symbol in braces is a 6j symbol and γ_{fi} is the probability per unit time of a transition from level f to i (and only downward transitions are considered). Note that,

as mentioned above, these matrix elements are diagonal in K and Q and independent of Q, but they are not independent of K. Cross relaxation of optical and hyperfine coherences is ignored (Rabin and Ben-Reuven 1979) which means that off-diagonal elements of the form $\langle\langle if^{\dagger};K,Q|\Sigma|kg^{\dagger};K,Q\rangle\rangle$ are zero.

The field interaction operators, U_η, in the irreducible tensor basis are not as simple as the relaxation terms. The derivation of the matrix elements of the U_η is left to an appendix (Appendix B) and only the result is stated here.

$$\langle\langle if^{\dagger};K',Q'|U_\eta|kg^{\dagger};K,Q\rangle\rangle = S(F_k,F_g,F_f,K,K',Q,Q')\beta^{(\eta)}_{gf}\varepsilon^{(\eta)}_{Q-Q'}\delta_{ki} - S(F_g,F_k,F_i,K,K',Q,Q')\beta^{(\eta)}_{ik}\varepsilon^{(\eta)}_{Q-Q'}\delta_{fg} \tag{4.33}$$

where $\varepsilon^{(\eta)}_{Q-Q'}$ is a component on the circular basis of the polarisation vector of the field η. The scaling functions, S, are given by

$$S(F_x,F_y,F_z,K,K',Q,Q') = (-1)^{K}(-1)^{Q-Q'}(-1)^{F_x+F_y}(2K'+1)^{1/2} \langle 1,K',Q'-Q,-Q'|K,-Q\rangle \begin{Bmatrix} 1 & K' & K \\ F_x & F_y & F_z \end{Bmatrix} \tag{4.34}$$

The β parameter is given by

$$\beta^{(\eta)}_{xy} = \hbar^{-1}\mu_{xy}E_\eta = -\hbar^{-1}(-1)^{J_x+I+F_y}(2F_x+1)^{1/2}(2F_y+1)^{1/2} \begin{Bmatrix} 1 & F_y & F_x \\ I & J_x & J_y \end{Bmatrix} \langle J_x\|\mu\|J_y\rangle E_\eta \tag{4.35}$$

where I is the nuclear spin quantum number. μ_{xy} is the reduced matrix element of the dipole operator ($\langle x \| \mu \| y \rangle$) and $E^{(\eta)}$ is the amplitude of the field η. β is therefore an average Rabi frequency for the transition. Previous authors (Shore 1978, Delsart and Keller 1976, 1980, Fisk 1985, Fisk et al 1986b) have used an expression for the Rabi frequency of a transition between individual Zeeman sub-levels, whereas here the effects of Zeeman degeneracy are included in the scaling factor, S, and the field polarisation is accounted for by the values of $\varepsilon^{(\eta)}_{Q-Q'}$.

The two Kronecker delta symbols (δ_{ki} and δ_{fg}) in the expression for the matrix elements of U (Eq. 4.33) show that the interaction operator changes only one of the two levels involved in a Liouville space basis state. Because β involves a dipole matrix element, the combination of Kronecker delta symbols and β parameters shows that the interaction operator transfers a Liouville space state between the even and odd parity atomic sub-spaces. Thus, for example, an optical coherence is created from a Zeeman coherence by one application of U.

The representation of the Liouville space bra, $\langle\langle \underset{\sim}{\mu} |$, representing the dipole moment is calculated from the matrix elements of the dipole operator in Hilbert space (see Appendix B).

$$\langle\langle \underset{\sim}{\mu} | = \frac{1}{\sqrt{3}} \sum_{i,f,Q} (-1)^{F_f - F_i} \mu_{fi} \underset{\sim}{e}_Q \langle\langle if^{\dagger}; 1, Q | \qquad (4.36)$$

where the summation over levels i and f is restricted to pairs of levels that are connected by electric dipole transitions.

Using the above expressions for the various Liouville space operators and vectors, the signal field can be calculated. As mentioned earlier, the matrices are too large for an analytical solution and the necessary calculations are performed by computer. Appendix C describes a programme that was written to predict the experimental results. The programme is capable of treating four levels with arbitrary angular momentum quantum numbers (restricted by the memory and CPU time requirements for large values) and any polarisation of the pump and probe fields.

4.3 Doppler broadening

Doppler broadening has so far been excluded from the theoretical description. However, as mentioned in Chapter 3, it has a substantial effect on the profiles. If the velocity sub-groups behave independently, the Doppler broadened signal field, $\underset{\sim}{E}_S^D(\delta_1, \delta_2)$, can be derived from the Doppler free signal field, $\underset{\sim}{E}_S(\delta_1, \delta_2)$, by adding the contribution from each sub-group, weighted by the number of atoms in that sub-group.

$$\underset{\sim}{E}_s^D(\delta_1,\delta_2) = \int_{-\infty}^{\infty} \underset{\sim}{E}_s(\delta_1-\varepsilon\delta_D,\delta_2-\delta_D)\,W(\delta_D)\,d\delta_D \qquad (4.37)$$

In calculating the contribution from a velocity subgroup, the probe and pump detunings, δ_1 and δ_2 respectively, have been converted to the detunings in the rest frame of the atom. δ_D is the Doppler shift of a field with wave vector $\underset{\sim}{k}$ for an atom moving with velocity $\underset{\sim}{v}$

$$\delta_D = |\underset{\sim}{k}.\underset{\sim}{v}| \qquad (4.38)$$

The Doppler shifts of the two fields are assumed to be equal since the frequency difference between the fields is much smaller than their frequency. The parameter ε in Equation 4.37 indicates the relative propagation directions of the pump and probe fields

ε = 1 co-propagating fields

-1 counter-propagating fields

so the arguments of $\underset{\sim}{E}_s$ in Equation 4.37 are the detunings of the two Doppler shifted fields in the rest frame of the atom. The weight function $W(\delta_D)$ is the Maxwellian velocity distribution expressed in terms of the Doppler detuning (Eq. 3.3).

Since Equation 4.37 is essentially a convolution of the functions $\underset{\sim}{E}_s$ and W, it can be expressed in a simpler form in terms of the Fourier transforms of $\underset{\sim}{E}_s^D$, $\underset{\sim}{E}_s$ and W (written $\underset{\sim}{d}$, $\underset{\sim}{s}$ and w respectively)

$$\underset{\sim}{d}(\varsigma_1,\varsigma_2) = \underset{\sim}{s}(\varsigma_1,\varsigma_2)w(\varsigma_1+\varepsilon\varsigma_2) \qquad (4.39)$$

where ς_1 and ς_2 are the Fourier transform variables. This is the basis of a separate computer programme (see Appendix C) that takes the Doppler free signal field calculated by the first programme for a range of pump and probe detunings and derives the Doppler broadened version.

4.4 Calculation of the signal

Adding the signal field to the probe field causes the changes in probe polarisation and amplitude that are observed in polarisation spectroscopy and saturated absorption experiments. The modified probe field passes through the analyser (in the case of polarisation spectroscopy) and falls on the photodetector which generates a signal proportional to the intensity. Since the pump beam intensity is modulated by a mechanical chopper and the signal is detected with a lock-in amplifier, the measured signal is proportional to the difference between the photo-detector signal with and without the pump field.

$$[A(\underset{\sim}{E}_S^D+\underset{\sim}{E}_1)].[A(\underset{\sim}{E}_S^D+\underset{\sim}{E}_1)]^*_{ON} - [A(\underset{\sim}{E}_S^D+\underset{\sim}{E}_1)].[A(\underset{\sim}{E}_S^D+\underset{\sim}{E}_1)]^*_{OFF}$$
$$= |A\underset{\sim}{E}_S^D|^2_{ON} - |A\underset{\sim}{E}_S^D|^2_{OFF} + 2Re[(A\underset{\sim}{E}_S^D).(A\underset{\sim}{E}_1)^*]_{ON} - 2Re[(A\underset{\sim}{E}_S^D).(A\underset{\sim}{E}_1)^*]_{OFF} \quad (4.40)$$

where any field $\underset{\sim}{E}$ is converted to $A\underset{\sim}{E}$ on transmission through the analyser. Subscripts "ON" and "OFF" refer to the state of the pump field.

The influence of the analyser on a field is treated using an operator technique. The operator A is chosen so that the product of its matrix representation and the column vector representing a field gives the field transmitted by the analyser. It is equal to an appropriate Jones matrix extended to three dimensions and converted to the spherical basis representation used in the calculations. The same formalism can be applied to a saturated absorption experiment if $A\underset{\sim}{E}$ is identical to $\underset{\sim}{E}$. A is therefore the unit operator in this case.

The signal (Eq. 4.40) consists of two components. The first has a quadratic dependence on the signal field. The second is due to the mixing of the signal field and the probe field on the detector, and is linear in the signal field. Since the probe field is substantially stronger than the signal field, it behaves as a local oscillator field, amplifying the signal. However, if the analyser blocks the probe field (as is the case for crossed polarisers in a polarisation spectroscopy experiment) the beat term is zero and the signal is entirely due to the quadratic term.

The computer calculation of the signal from the signal field is done by the Doppler broadening programme after the Fourier transform calculations. The resulting theoretical profiles are plotted in the same format as used for the experimental results in the previous chapter. Comparisons between the two types of profile are presented in Chapter 5. Chapter 5 also discusses details of the theoretical treatment and the importance of approximations made in the derivation.

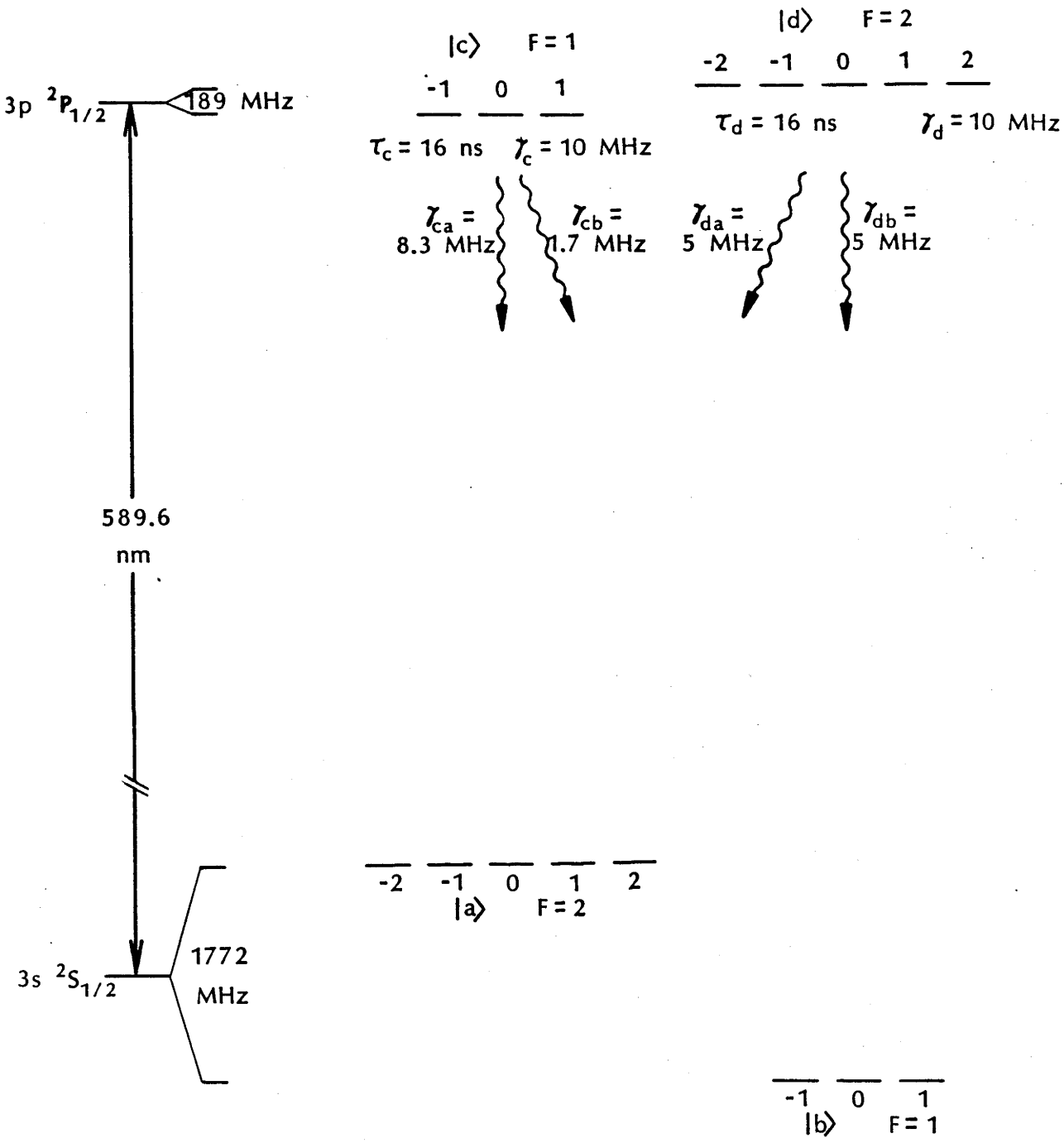

Figure 4.1 States involved in the D_1 transition of sodium. The hyperfine splitting and Zeeman degeneracy of the levels is shown, along with upper level lifetimes (τ_u), linewidths (γ_u) and the cross relaxation rates (γ_{ul}). The level labelling arrangement is also shown.

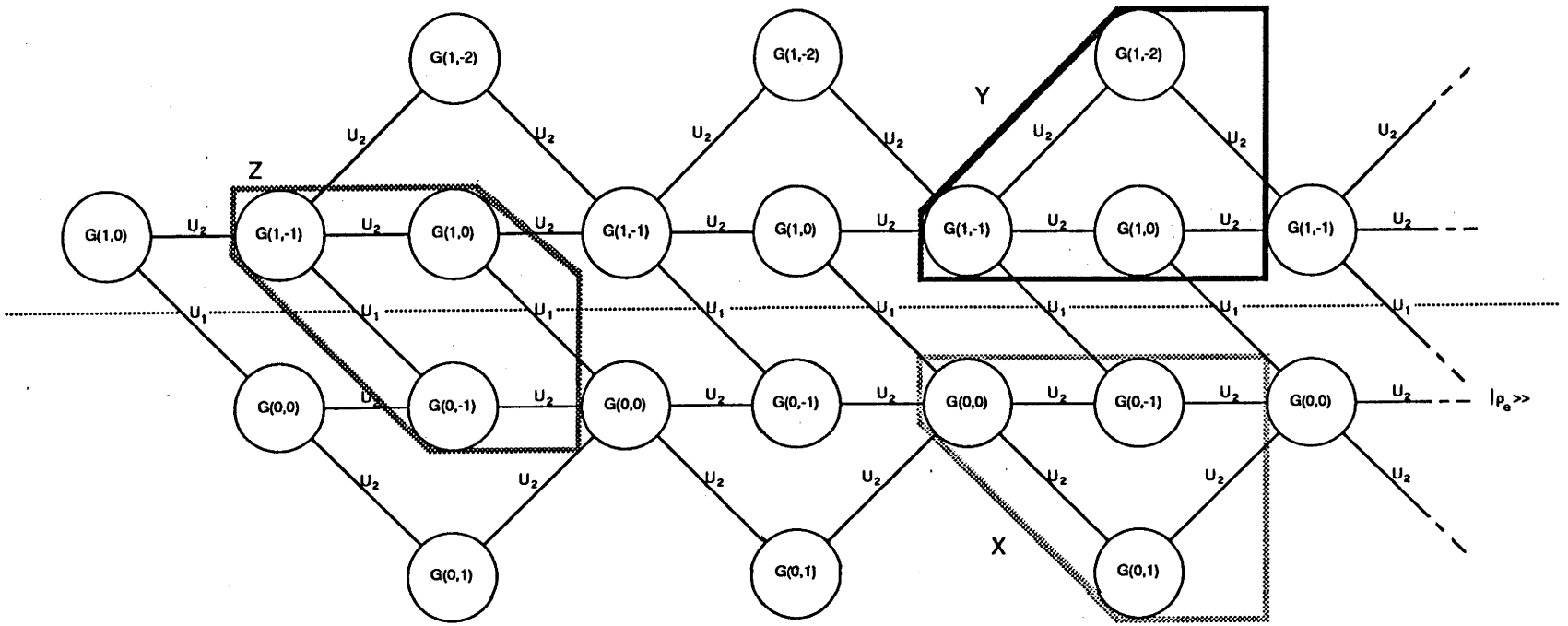

Figure 4.2 Diagrammatic representation of the power series for the density matrix. Harmonics number matrix elements of linear response Green's functions are represented by circles. The lines represent pump (U_2) or probe (U_1) field interaction operators. The repeating units labelled X, Y and Z are used to resum the equation for the density matrix. They are given by

$$X = G(0,0)U_2[G(0,-1)+G(0,1)]U_2$$
$$Y = G(1,-1)U_2[G(1,-2)+G(1,0)]U_2$$
$$Z = G(1,-1)[U_2G(1,0)U_1+U_1G(0,-1)U_2]$$

Chapter 5. Comparison of Theory and Experiment

Before comparing the results of the theoretical treatment described in the previous chapter with the experiments, there are several points that should be made about the theory. Since the technique used in the calculations is not commonly used, interpretations of some aspects will be given in Section 5.1. Sections 5.2 and 5.3 present comparisons between theoretical and experimental results for saturated absorption and polarisation spectroscopy with a linearly polarised pump beam. Calculations for the third category, polarisation spectroscopy using a circularly polarised pump laser, were not done due to prohibitive computer time requirements. Finally, Section 5.5 discusses possible causes of discrepancies found in the comparisons.

5.1 Important features of the theory

The solution of the Liouville equation (Eq. 4.1) used in this technique is different from the more common method where the time evolution of the density matrix is calculated from the Bloch equations. However, use of the current technique is worthwhile since it converts a set of coupled differential equations (the Bloch equations) into a simple algebraic expression (Eq. 4.22). The complexity of the atomic system is absorbed into the components of this expression which are operators on the atomic space. The complexity can be treated by computer using matrix representations of the operators.

It is of interest to compare the sizes of the matrices with those involved in a standard master equation solution for the same level system. Figure 4.1 shows that there are 16 states in the sodium D_1 transition, resulting in a density matrix with 256 elements. Because it is an Hermitian matrix, there are, at most, 136 independent elements. Since both upper levels are optically connected to both lower levels and the lasers may have arbitrary polarisations, all possible elements must be considered. An important simplification occurs when the lasers are both π polarised. In this case, there are 36 independent components.

As outlined in Chapter 4, the density matrix may be expressed in terms of irreducible tensor components (Eq. 4.27). Since this is purely a basis change, it does not reduce the dimensionality of the space and hence the size of the density matrix. The advantage of this representation arises because spontaneous emission exhibits much greater symmetry when expressed in terms of irreducible tensor components (see Chapter 4), simplifying the relaxation matrix.

During the derivation of the diagrammatic solution of the Liouville equation, even and odd parity sub-spaces were identified and it was noted that, because the interaction operators transfer a Liouville space ket from one parity sub-space to the other, the Green's functions in the power series solution Eq. 4.17 alternate between the odd and even sub-spaces. For this reason, the matrix representations of the

repeating units X, Y and Z of the diagram are of smaller dimensionality than the complete density matrix. The particular frequency component of the density matrix that is calculated is similarly from one or other sub-space and is reduced in size.

For the transition used in this experiment, the density matrix has 36 independent components if both lasers are π polarised and the Liouvillian matrix would be 36x36. In contrast, only 14 elements would be calculated with the current technique, and the matrices involved in the diagram would be 28x28 in size.

It is possible to gain some understanding of the Green's function solution used here, even though it is not as obvious as the alternative technique where the time evolution of the elements of the density matrix is calculated directly. The first point to note is the interpretation of the solution (Eq. 4.12) in terms of an integral equation. The Liouville equation (Eq. 4.11) was written in a form which simplified the derivation of the series solution (Eq. 4.17).

However, it could be written in the more usual form for solution using Green's functions.

$$i\frac{d}{dt}\left(\delta\rho(t)\right) + \left(\underset{\sim}{n}.\underset{\sim}{\omega}\underset{\sim}{I} - L_a - \Sigma\right)\delta\rho(t) = U\left(\rho_e + \delta\rho(t)\right) \qquad (5.1)$$

The driving terms, represented by the U operator, have been collected on the right hand side. This means that the linear

response Green's function replaces $\hat{G}$ in the integral equation solution.

$$\delta\rho(t) = \int_{-\infty}^{\infty} g(t,t')\ U[\rho_e + \delta\rho(t')]\,dt \qquad (5.2)$$

This form can be used to interpret the solution based on the physical interpretation of Green's functions (see, for example, Roach 1982). The Green's function represents the response of the system at time t to a unit driving impulse applied at time t'. The time dependent linear response Green's function, G (obtained by removing the U operator from Eq. 4.14), represents a sinusoidal oscillation damped by the relaxation operator. This is consistent with the interpretation of G as the response to an impulse.

The integral equations (either Eq. 5.2 or Eq. 4.12) therefore represent the combined response due to application of the driving force U at all possible times from the start of the interaction. The step function, $\theta(t-t')$, restricts the integral to times earlier than t, ensuring that only causal terms are included.

However, because the start of the interaction was set to $-\infty$ in order to evaluate the integral equation, the initial transient behaviour that occurs when the interaction starts makes a negligible contribution to the solution. Because the response is integrated over an infinite time, the initial transients, which are of finite duration, are insignificant

compared with the contribution from the period when the system has reached steady state.

The harmonics number representation of the density matrix (Eq. 4.4) is essentially a Fourier series expansion. As mentioned in Chapter 4, the non-linear response to the oscillatory driving fields is expected to be a set of harmonics of the applied fields. The connection between these harmonics and photon absorption and stimulated emission processes was also made.

The harmonics number representation is used to select the component of the density matrix that is oscillating at the frequency of the probe field. The diagrammatic solution of the Liouville equation, Fig. 4.2, gives a clear picture of the frequencies that contribute to this component. The circles representing Green's functions are labelled by harmonics number component, indicating the sequence of field harmonics generated by the non-linear interaction. The harmonics numbers in the diagram therefore show the possible density matrix frequency components. Selecting the component at the probe frequency fixes the left hand end of the diagram and therefore determines the possible Green's functions in the sequence from right to left.

The allowed frequency components are restricted both by the assumption that one interaction with the probe beam occurs and by the resonance condition. The resonance condition is equivalent to the rotating wave approximation.

Under this approximation, terms that do not conserve energy are eliminated from the density matrix. To see that the resonance condition eliminates such terms, consider an example of a GUG sequence. Choosing $G(0,-1)U_2G(0,0)$, the possible matrix elements in a simplified two state system (with the upper state labelled c) would be

$$\begin{aligned}
&\langle\langle ac^\dagger|G(0,-1)|ac^\dagger\rangle\rangle\langle\langle ac^\dagger|U_2|aa^\dagger\rangle\rangle\langle\langle aa^\dagger|G(0,0)|aa^\dagger\rangle\rangle \\
&\langle\langle ac^\dagger|G(0,-1)|ac^\dagger\rangle\rangle\langle\langle ac^\dagger|U_2|cc^\dagger\rangle\rangle\langle\langle cc^\dagger|G(0,0)|cc^\dagger\rangle\rangle \\
&\langle\langle ca^\dagger|G(0,-1)|ca^\dagger\rangle\rangle\langle\langle ca^\dagger|U_2|aa^\dagger\rangle\rangle\langle\langle aa^\dagger|G(0,0)|aa^\dagger\rangle\rangle \\
&\langle\langle ca^\dagger|G(0,-1)|ca^\dagger\rangle\rangle\langle\langle ca^\dagger|U_2|cc^\dagger\rangle\rangle\langle\langle cc^\dagger|G(0,0)|cc^\dagger\rangle\rangle
\end{aligned} \tag{5.3}$$

The resonance condition allows only the first two matrix elements. As mentioned in Chapter 4, the expressions for the interaction Hamiltonian (Eq. 4.9) and the harmonics number expansion of the density matrix (Eq. 4.4) show that the reduction in the harmonics number n_2 caused by the U_2 operator in Equations 5.3 indicates a stimulated emission process.

Using the expression for the interaction Hamiltonian (Eq. 4.9) the matrix elements of the interaction operator, U, can be calculated.

$$\begin{aligned}
\langle\langle ac^{\dagger}|U|aa^{\dagger}\rangle\rangle &= -h^{-1}\langle a|H_i|c\rangle \\
\langle\langle ac^{\dagger}|U|cc^{\dagger}\rangle\rangle &= h^{-1}\langle a|H_i|c\rangle \\
\langle\langle ca^{\dagger}|U|aa^{\dagger}\rangle\rangle &= h^{-1}\langle c|H_i|a\rangle \\
\langle\langle ca^{\dagger}|U|cc^{\dagger}\rangle\rangle &= -h^{-1}\langle c|H_i|a\rangle
\end{aligned} \tag{5.4}$$

It can be seen that both allowed terms correspond to downward transitions, as expected for a stimulated emission process. In contrast, the matrix elements of U in the two disallowed terms represent upward transitions.

The two possible harmonics number vectors in the even space are (0,0) and (1,-1). Because atomic populations are in the even space, the presence of the latter component indicates that the population may oscillate at the frequency difference between the two fields. This effect has been used to explain the presence of a hole in pump-probe studies of a homogeneously broadened transition. Boyd and Mukamel (1984) have shown that it is important to include all possible time orderings of pump and probe field interactions. The diagrammatic representation of the solution used here shows that these terms are included in this technique. The second term in Eq. 4.22 (corresponding to the upper half of the diagram Fig. 4.2) includes paths with at least one pump interaction, U_2, occurring after a probe interaction. Terms oscillating at the difference frequency are only present in this half of the diagram.

Equation 5.4 shows that, in a simplified level system, the matrix elements of the U interaction operator are Rabi frequencies. Using an irreducible tensor basis for the extended level system with hyperfine structure and Zeeman degeneracy introduces a number of scale factors into these matrix elements. Equations 4.33, 4.34 and 4.35 show the scale factors. The factor involving the reduced matrix element of the dipole operator may be termed the "reduced Rabi frequency" and it is this factor that is used as a parameter in the theoretical calculations. It excludes all variations due to hyperfine structure and tensor order.

It is well known that optical pumping between lower states allows saturated absorption and polarisation spectroscopy to be carried out at much lower pump intensities than would be expected if saturation effects alone were responsible. The calculations show the same effect. Reduced Rabi frequencies of the order of the natural width of the transition were used for some comparisons with experiment. Since all the scale factor combinations for this level system are less than one, all individual elements of the irreducible tensor representation are driven by small effective Rabi frequencies.

The current theoretical treatment differs from many others in the calculation of the signal from the density matrix, as well as in the technique for initially calculating the density matrix. Most treatments express the observed signal in terms of components of the susceptibility tensor

(or equivalently the refractive index and absorption coefficient), making some approximations about which components may be ignored (see for example Wieman and Hansch 1976, Kaftandjian et al 1979, Nakayama 1981b, 1985). Such treatments require a different expression for each possible configuration of laser polarisation in the two types of experiment. Nakayama (1985) gives a summary of the various combinations.

The use of an operator to treat the action of the analyser (as described in Chapter 4 and Appendix C) is more versatile than previous techniques. No assumptions are made about the analyser being close to the crossed position as is common (although not essential) in other techniques. In addition, saturated absorption, where an analyser is not used, may be treated with the same formalism using a unit operator. Thus the same computer code is used for all types of experiment by entering appropriate representations of the analyser.

It was found necessary to reduce the versatility of this technique for computational efficiency. The polarisation of the field transmitted by the analyser is independent of the incident field. The transmitted field may thus be expressed as a complex amplitude, reducing the computer time and storage requirements of subsequent calculations.

This simplification may not be applied to saturated absorption calculations since an analyser is not used. However, since the reduction in computer time was essential, it was applied by using an analyser aligned parallel to the polarisation of the probe field. If the lasers were polarised in the same direction, no change to the polarisation of the probe field would occur. In this instance, the calculations are expected to give the correct results. However, if the two polarisations were different, some discrepancies may occur. Comparisons with experiment are therefore restricted to the standard arrangement, i.e. parallel polarisations.

Because the signal field and the probe field must be added to calculate the signal (Eq. 4.40), it is important that the signal field be calculated in the same units as the probe field. Appendix B shows the calculation of the reduced matrix element of the dipole operator. It is expressed in terms of the upper level lifetime in order to scale the signal field correctly.

The relative importance of the quadratic and linear terms in the signal can only be predicted if the signal field is scaled correctly. The derivation of the signal field from the density matrix using Equations 4.23 and 4.26 shows that, in addition to various fundamental constants and the lifetime of the upper level, the number density of the atomic medium is involved in scaling the signal field. In order to compare theory and experiment, the number density must be known or

treated as an adjustable parameter.

Calculation of the Doppler broadened signal field from its Doppler free counterpart as described in Chapter 4 is only valid if the individual velocity sub-groups can be assumed to behave independently. In a low density vapour such as that used in these experiments, there is no collisional interaction between atoms as they pass through the laser beams. The density is also low enough to preclude significant absorption of spontaneously emitted photons by other atoms. Since neither collisional nor radiative coupling between atoms is significant, the assumption of independent velocity sub-groups is valid.

However, Eq. 4.37 does not correctly describe the Doppler effect in the presence of residual Doppler broadening due to slight misalignment between the pump and probe beams. It is derived under the assumption that, for any velocity sub-group, the Doppler shifts of the pump and probe beams are equal in magnitude, with the possible sign difference being accounted for by ε. However angular displacement of the beams invalidates this assumption. The Doppler broadened signal is due to the weighted sum of contributions from all velocity sub-groups and is therefore expressed as an integral over the three-dimensional velocity space. Because the Doppler shift depends only on the velocity component in the direction of the laser beam, the three-dimensional integral collapses to a single dimension and may be expressed in terms of the Doppler shift as in Eq. 4.37.

If the beams are not parallel a second spatial dimension is introduced and the velocity integral collapses to a two-dimensional integral. Integration along the ±45° lines of Figs. 3.3 or 3.4 that is implied by Eq. 4.37 must be changed into integration over the whole plane. Significant contributions to the integral would be expected from ±45° strips of width determined by the residual Doppler broadening.

Chapter 3 gives a description of the relationship between features in the Doppler broadened profiles and the positions of resonances in the Doppler free case. It is a straight forward matter to determine which resonances contribute to the signal at a particular combination of pump and probe detunings. However, calculation of the signal from the Doppler free signal is not as simple.

In the case of saturated absorption where the linear term in the signal (Eq. 4.40) is dominant, the signal calculated for a Doppler free experiment can be used to estimate the relative amplitudes of features in the Doppler broadened profiles. Since the signal is linearly related to the signal field, the operations involved in calculating the signal (Eq. 4.40) may be taken inside the Doppler integral (Eq. 4.37). This means that the Doppler broadened profile can be obtained from the Doppler free profile by adding signal values using the techniques of Chapter 3.

The ability to do this is useful in generating calculated sets of Doppler broadened profiles for comparison with experiment. By examining the relative sizes of certain peaks in Doppler free profiles it is possible to estimate the quality of agreement between theory and experiment without completing a full Doppler broadened calculation. Since the Doppler free version requires much less computer time than the full calculation, it is possible to adjust parameters to optimise the agreement. Repeated generation of the Doppler broadened profiles for this purpose would be impractical.

The above procedure is not valid for the quadratic term in the expression for the signal. The full Doppler broadening calculation must be applied to the signal field before it is used to calculate the signal. The difference between the two techniques is similar to the difference between adding amplitudes (signal field) or intensities (signal) in describing interference. The latter ignores interferences between the signal fields generated by different velocity sub-groups. These interferences have an important influence on the profiles. Since they are effectively ignored if the Doppler free profiles are used to predict the Doppler broadened results, optimisation of the agreement is not possible.

5.2 Saturated absorption

To test the accuracy of the theoretical model, full Doppler broadened calculations were done for a number of pump and probe polarisations and compared with corresponding

experimental profiles. Starting with the simplest case of saturated absorption with a relatively low intensity pump beam and both lasers linearly polarised in the same direction, Figure 5.1 compares theory (on the overlay page) with experiment. In this figure (and others like it), plots of the two types of profile are adjusted to equalise the offsets of the zero levels. The scaling of the vertical axes is arranged to make the amplitudes of the two entire data sets equal. Thus the dependence of the size of the profiles on the pump detuning is retained. Figure 5.2 shows a more detailed comparison for one pump detuning.

As mentioned above it was possible to adjust certain parameters to optimise the fit using the Doppler free calculations. The adjustable parameters were the pump Rabi frequency and the ground state relaxation time. Because entrances to the vapour cell used in the experiment were too small, it was not possible directly to measure the pump intensity in the interaction region. The intensity was therefore measured outside the cell and reasonable estimates of the scattering by polarisers and windows in the beam were used to derive the intensity at the interaction region. This value was used to calculate the first estimate for the pump Rabi frequency. In a similar fashion, the first estimate for the ground state relaxation time was derived from the propagation time of atoms moving through the laser beams at the mean thermal speed.

Because of the large amounts of computer time required to generate each Doppler broadened profile, parameter optimisation was carried out using Doppler-free profiles. The pump Rabi frequency and ground state relaxation time were adjusted from the first estimate until the relative sizes of the peaks contributing to the principal resonance (ac and ad) and crossover resonances (Cad and Dac) in the vicinity of zero pump detuning matched the experimental values. Adjustment of the two parameters had distinguishable effects on the profiles so it was possible to optimise them independently.

This process was valid because the linear term of the signal (Eq. 4.40) is used in saturated absorption and there were no extra peaks due to A.C. Stark splitting because of the small pump Rabi frequency. The experimental Doppler width was used in the Doppler broadening calculations with no attempt made at optimisation.

There is good agreement between the two sets of profiles across the range of pump and probe laser detunings. The signs and general form of the profiles are correct, in particular the signs of the crossover resonances and the change in sign of the peak on line II (see Fig. 3.3) with increasing pump detuning. There are some minor inaccuracies in the amplitudes of some peaks, especially the "Λ system" and "N system" crossovers.

The Rabi frequency used in the calculation agrees reasonably well with the experimental Rabi frequency measured from the pump power and pump beam size in the interaction region. The experimental profiles actually represent an average over the range of Rabi frequencies in the interaction region. The quoted experimental Rabi frequency is derived from the estimated pump power per unit area, assumed to be constant over a circle of radius equal to the measured 1/e intensity radius and restricted to that circle. It is unlikely that this averaging technique matches the averaging in the profiles, but it should give a reasonable estimate of the Rabi frequency. In contrast, the theoretical calculations are restricted to a single Rabi frequency so the agreement with the experimental value cannot be expected to be perfect.

5.3 Polarisation spectroscopy: linearly polarised pump

Figure 5.3 compares theory and experiment for polarisation spectroscopy with linearly polarised pump and probe beams, with an angle of 45° between the two polarisations. The analyser is crossed in this case. The pump intensity was higher for these profiles as indicated by the increased power broadening. Again, the general form of the profiles is correctly predicted by the theory. In particular the total absence of line IV, VI and VII crossovers and the reduction in the size of the principal resonance with increasing pump detuning.

However, the discrepancies are more severe, with some noticeable differences in amplitude. Since the power broadening in the theoretical profiles appears to be more severe, it is possible that the Rabi frequency used in the calculations was too high. With a crossed analyser, the quadratic term in the signal calculation is used so it was not possible to optimise the fit before the Doppler calculation was done. The experimental Rabi frequency was therefore used in the calculations.

A similar arrangement of pump and probe polarisations with the analyser rotated by 2.5° is shown in Fig. 5.4. The same parameters were used in the calculation of the signal field for the two cases of polarisation spectroscopy. It was only necessary to redo the calculation of the signal from the signal field to generate the necessary data for Fig. 5.4.

Again, the general trends are correctly predicted. As the analyser is rotated in the positive direction the principal resonance changes sign and the "Λ system" and "N system" crossovers increase in amplitude. As in the crossed analyser case, there are some discrepancies in the amplitudes of certain peaks, especially the D$\underline{a}$c crossover on line III. In addition, the negative going dip corresponding to the principal resonance is deeper in the theoretical profiles than in the experiment. With the analyser rotated away from the crossed orientation, the signal contains contributions from both the quadratic and linear terms. The relative importance of these two terms depends on the

analyser orientation and the number density of the vapour.

Because it was only necessary to redo the calculation of the signal from the theoretical data for the previous comparison, it was possible to do some adjustment of the number density to optimise the fit. The initial number density used was calculated from the relative absorption of the vapour but the fit was improved by reducing this value. However it appears from the comparison that the final value used had been reduced too much. This would account for the overestimated depth of the dip.

5.4 Polarisation spectroscopy: circularly polarised pump

Because the circularly polarised pump beam causes changes in the Q tensor component of ± 1, the matrix representations of the Liouville space operators are not restricted to $Q = 0$ elements as is the case for a linearly polarised pump. The increased size of the matrices means that the calculations require more than four times as much computer time as the linearly polarised case. A total of more than eight hours of computer time would have been required so these calculations were not attempted.

5.5 Possible reasons for discrepancies

Although the agreement between theory and experiment demonstrated in this chapter is reasonable, there are discrepancies in some details. These discrepancies may be due to approximations in the theory and computational restrictions, or they may arise from limitations in the

experiment.

The most obvious major approximation made in the theory was the steady state assumption. In order to evaluate the integral in Eq. 4.12, it was necessary to set the lower limit of integration to $-\infty$. This limit represents the start of the interaction between the atoms and the laser fields. If there is sufficient time from the start of the interaction for the atomic system to evolve to a steady state, this will be a valid approximation. To evaluate the validity of this approximation, it is necessary to compare the characteristic times involved in the evolution with the time limits imposed by the experimental arrangement. Since the interaction starts when an atom enters the laser beams, the time limit imposed by the experiment is the time taken to propagate through the beams.

The characteristic times of the evolution are the optical pumping and Rabi flopping times induced by the pump laser and the relaxation times for the atomic populations and coherences. The smallest pump laser Rabi frequency used in the experiment was of the same order as the natural width of the transition. For these laser intensities the optical pumping rate was also of the same order. Since the probe interaction is weak, only one probe photon absorption process occurs during the interaction time. The only characteristic time involved in the probe interaction is therefore the natural lifetime of the upper level.

The rms value of any Cartesian component of velocity in a thermal vapour of sodium atoms at 200°C is approximately 400 m/s so the average transit time across the 0.2 mm diameter laser beams is approximately 0.5 μs. Since this is 30 times longer than the lifetime of the excited state of the D_1 transition, it is reasonable to assume that the interaction time is long compared with the characteristic evolution times described above. The same assumption can be made about the decay times of the upper level populations and coherences and the optical coherences between upper and lower levels.

This assumption is not valid, however, for lower level populations and coherences. In the absence of collisions, the only decay channel for these elements of the density matrix is propagation of the atoms out of the interaction region. Atoms that leave the laser beams remove population and coherence from the atomic ensemble and are replaced by atoms with a thermal population distribution entering the interaction region. Since components of the density matrix would be expected to reach steady state only after several decay times, the steady state assumption cannot be satisfied for the lower level.

Nevertheless, a lifetime for the lower level population and coherence was included in the calculation. It was necessary to adjust this lifetime to achieve the agreement between theory and experiment shown in Fig. 5.1. The value used in all calculations was 2 μs, four times the value

calculated above from the average value of a velocity component.

Because the steady state assumption is violated as mentioned above, calculated variation of the profiles with lower level lifetime would not be expected to be completely accurate. The calculation of the transit time was based on the diameter of the probe laser beam since the signal is generated within this volume. However, since optical pumping and Rabi nutation are induced by the pump field, the larger diameter of the pump laser waist may be more appropriate. If this value (0.86 mm) is used, the propagation time matches the ground state lifetime used in the theoretical calculations more closely.

Rinneberg et al (1980) investigated the influence of propagation time (and magnetic field) on the amplitude of a particular crossover resonance in saturated absorption of the D_1 line of sodium. Because of the assumption of low pump intensity, they were able to integrate rate equations for the density matrix over the interaction time of the atoms. They showed that as the transit time increased the combined intensity of the Cad and Dac crossovers approached zero. No other features in the profiles were examined.

A further approximation is the neglect of what may be termed probe propagation effects. The theoretical treatment calculates the effects on the probe polarisation and intensity due to a single probe photon interaction with the

medium. The probe beam is then assumed to continue through the vapour without interacting further.

However, if the optical depth of the atomic medium is large enough, it is possible that further interactions could occur as the beam propagates through the vapour. The polarisation and amplitude of the probe field involved in these subsequent interactions would be different from that of the incident beam. Since the probe beam itself contributes to the evolution of the atomic density matrix, calculations performed using the incident probe field would be incorrect. The pump laser is not expected to be affected in the same way since it is more intense and is assumed to saturate the vapour.

By dividing the length of the interaction region into a number of "slices" and using the modified probe field from one slice as the initial probe field for the next, this effect could be included in the current theoretical treatment. However, this would require yet more computer time since the matrix representing U_1, the probe field interaction operator, depends on the probe field polarisation and amplitude. Thus the elements of this matrix would have to be modified for each probe detuning to account for the changing probe field. This refinement to the calculations was not attempted.

Since the interaction is assumed to be linear in the probe field, changes in the amplitude of the probe field due to the propagation effects will not distort the profile. If the pump and probe lasers have parallel linear polarisation (as in the saturated absorption profiles presented in Fig. 5.1), the polarisation of the probe beam will not be affected by the interaction. Propagation effects are therefore not expected to distort this sort of profile.

However, if the two lasers have different polarisations this is no longer the case. It is possible that this is a contributing factor to the poorer agreement for the polarisation spectroscopy profiles than for saturated absorption. Since the peak absorption of a weak probe by the vapour is only 20%, the probability of two interactions with the vapour in the absence of the pump field is less than 4%. The effects of the pump beam are unlikely to increase this probability so probe propagation effects can be assumed to be insignificant.

Residual Doppler broadening was also neglected in the theoretical treatment since, as indicated earlier in this chapter, a two-dimensional velocity integral would have been necessary. This would have made the (already substantial) computer resource requirements of the Doppler integration intolerable.

As a result of this approximation, there is a broadening of the experimental profiles that is not included in the theoretical calculations. This is unlikely to be significant because it would be masked by pump power broadening in all but the lowest Rabi frequency profiles. The mechanism for power broadening in Doppler broadened systems is superficially similar to the residual Doppler broadening effect. Large pump Rabi frequencies cause A.C. Stark splitting of the Doppler-free profiles which generates signals at probe frequencies away from the normal resonances. This creates significant contributions to the Doppler integral at combinations of pump and probe detunings slightly displaced from the ±45° lines described in Chapter 3. This is similar to the residual Doppler broadening effect which includes contributions from strips parallel to the ±45° lines.

As mentioned above, it was not possible to optimise the fit of the polarisation spectroscopy profiles by adjusting the pump Rabi frequency. This may be an additional reason for the discrepancies for this sort of profile as the Rabi frequency has a major influence on the relative sizes of the peaks as well as the degree of power broadening.

Experimental limitations also contribute to the uncertainty in the Rabi frequency. Because of the Gaussian intensity profile of the laser beams and the need slightly to misalign the two beams, the pump intensity varies over approximately 80% of its peak value within the interaction

region. The experimental profiles therefore represent an average over this range of Rabi frequencies, leading to possible distortions of the amplitudes of the peaks. This effect could also mask Autler-Townes splitting.

It would be possible to include the Gaussian profile effects in the theoretical calculations (see, for example, Fisk 1985, Fisk et al 1986a). However, since this would require repeating the calculations for a range of different Rabi frequencies, the computer time requirements would be prohibitive.

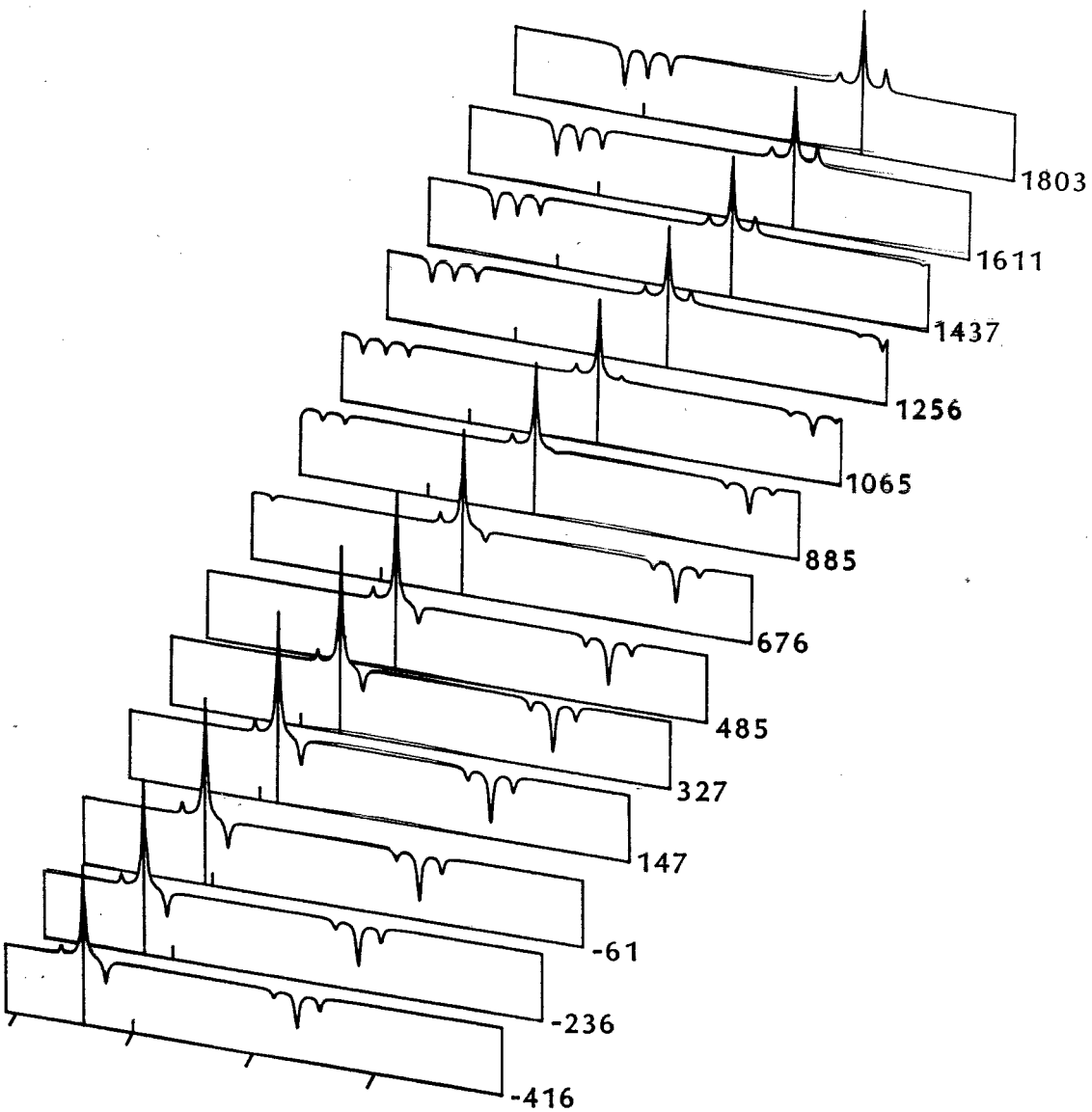
1803
1611
1437
1256
1065
885
676
485
327
147
-61
-236
-416

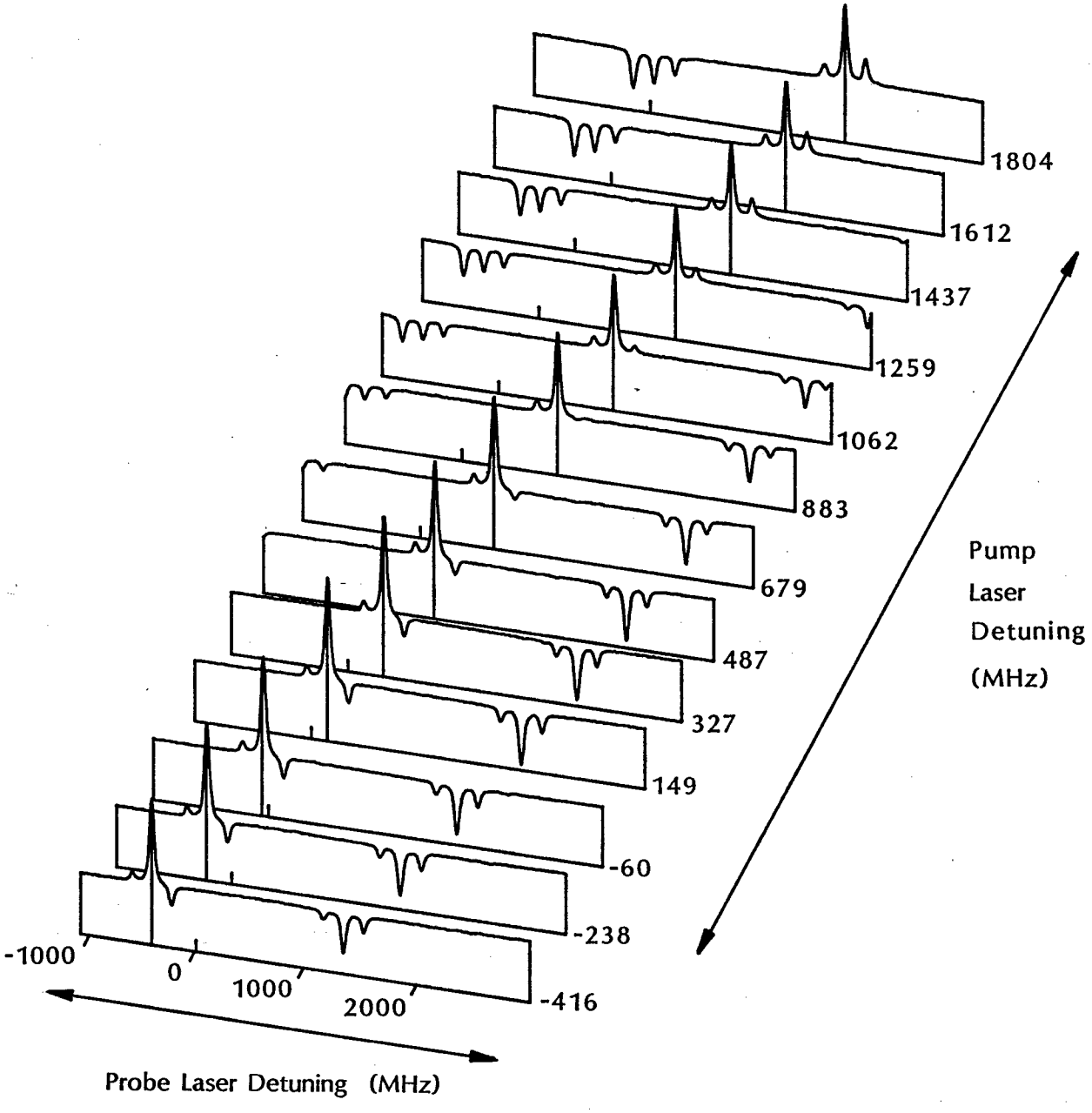

Figure 5.1 Comparison of theory (overlay sheet) and experiment for co-propagating saturated absorption profiles: parallel linear polarisations. The Rabi frequencies were : theoretical 5 MHz, experimental 10 MHz. The small vertical tic marks on the baseline of each profile indicate the position of zero probe laser detuning. The longer lines from each baseline to the profile indicate the positions of equal pump and probe detuning.

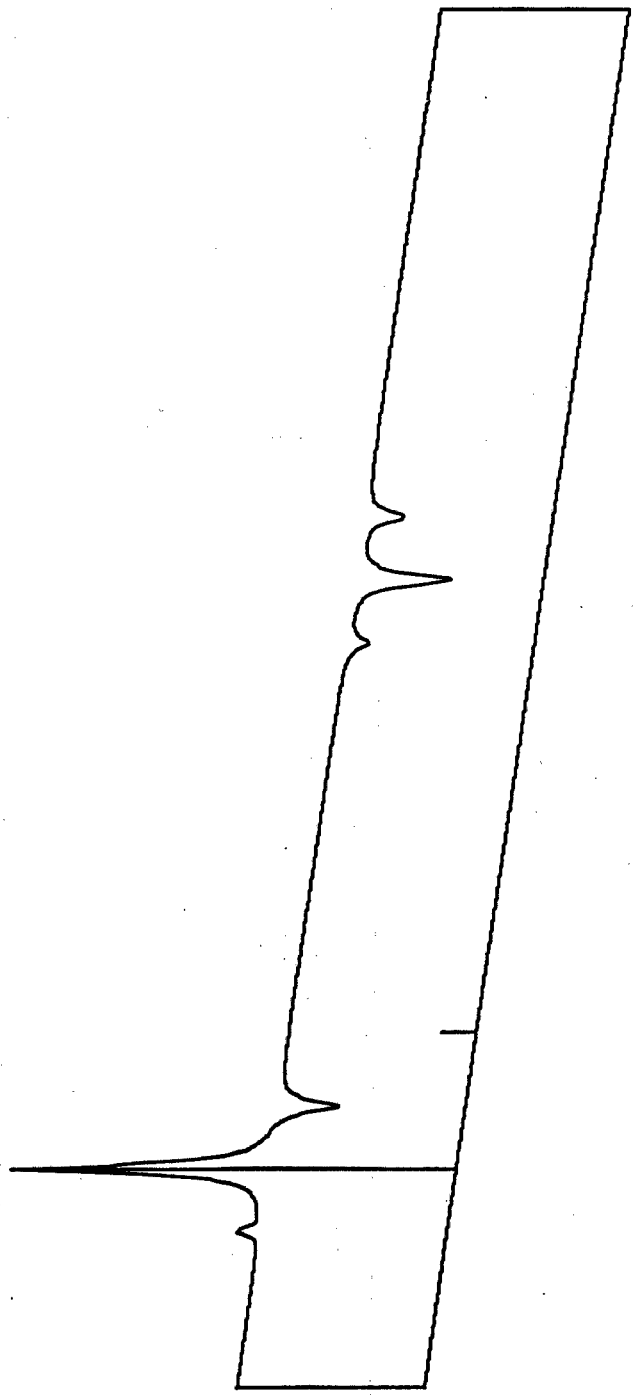

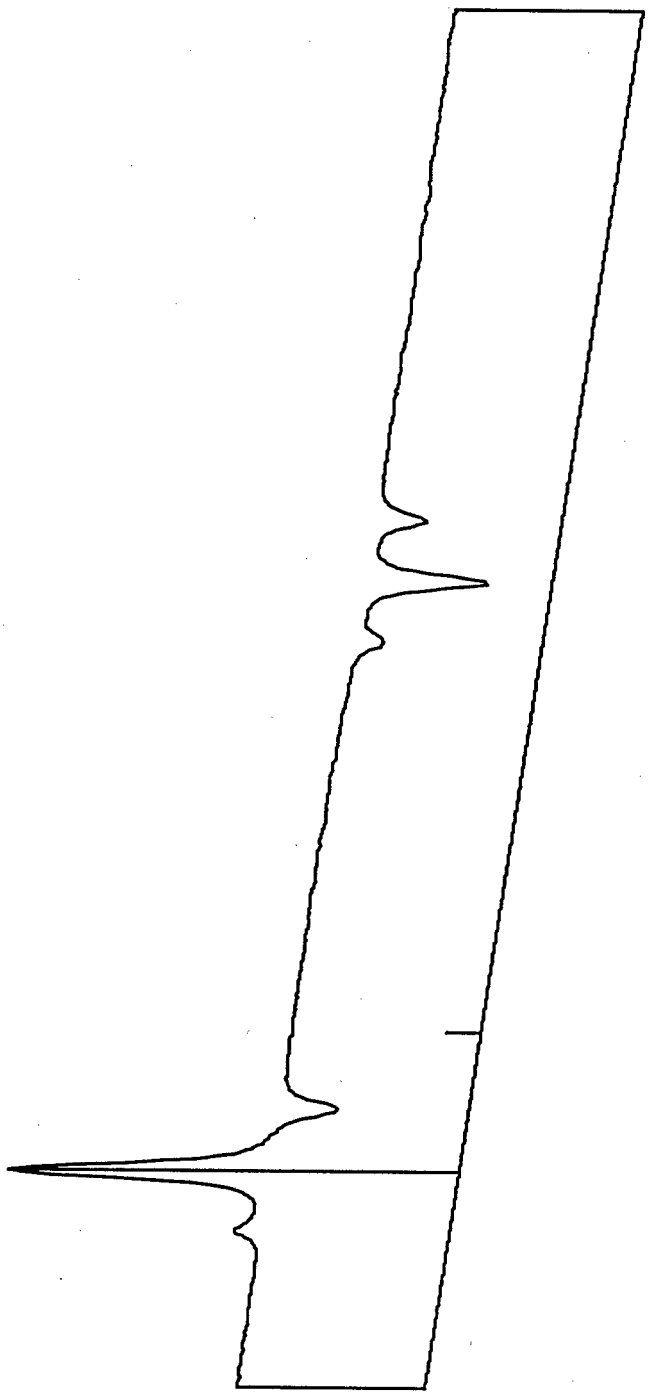

Figure 5.2 Expanded scale detail of Figure 5.1 for a pump detuning of -416 MHz, i.e. the "front" slice.

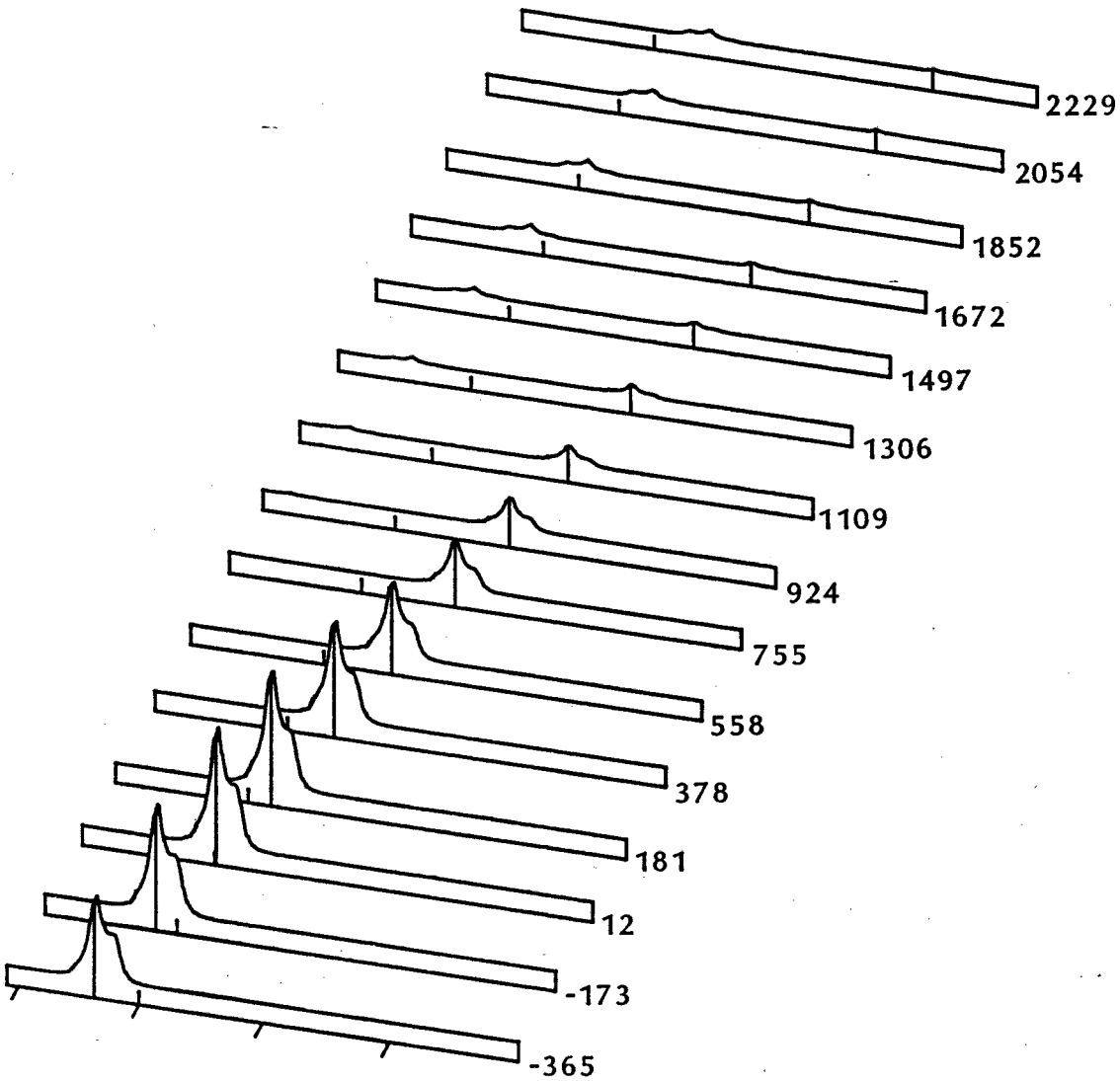
2229
2054
1852
1672
1497
1306
1109
924
755
558
378
181
12
-173
-365

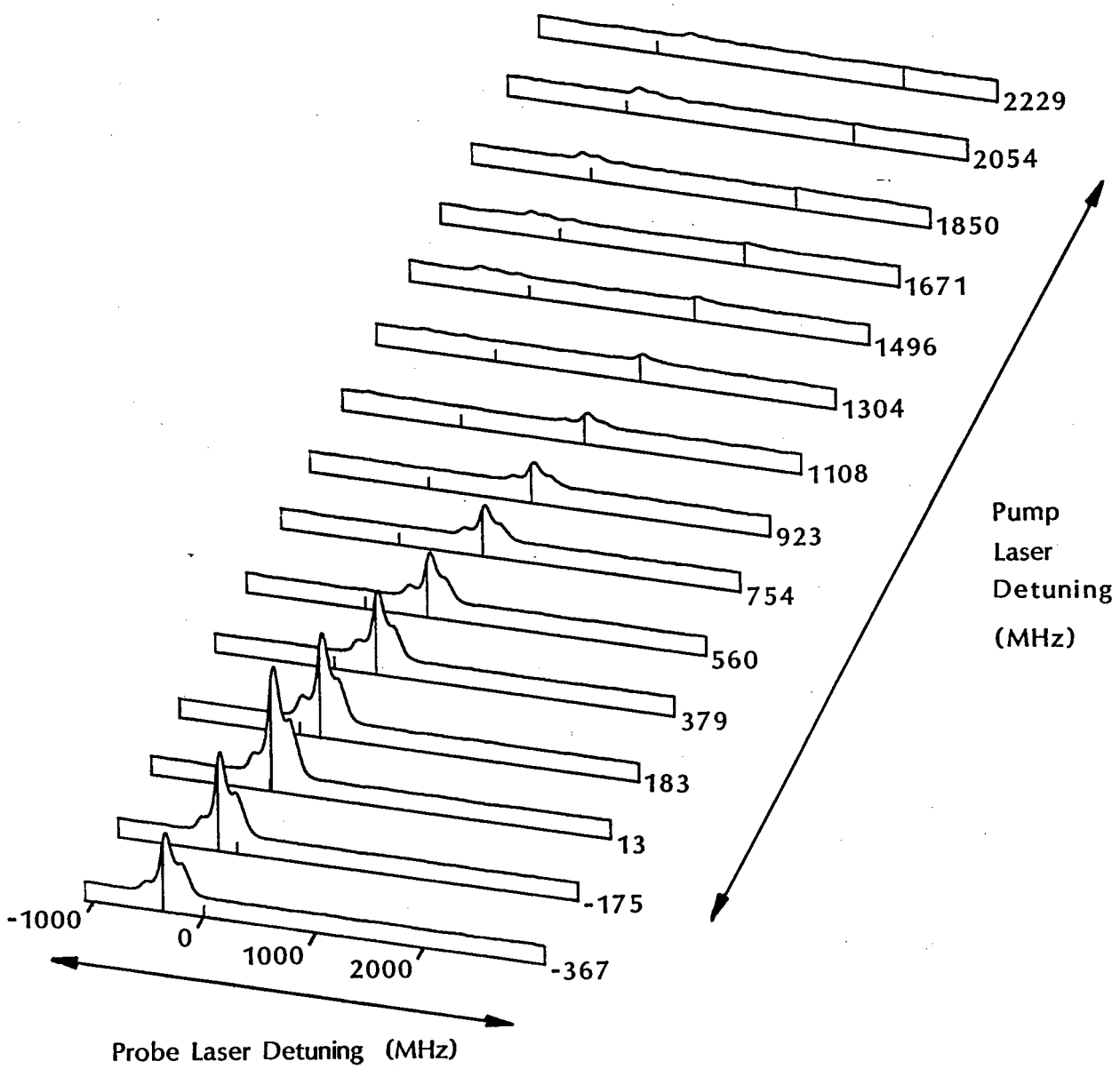

Figure 5.3 Comparison of theory (overlay sheet) and experiment for co-propagating polarisation spectroscopy: linearly polarised pump. The probe was linearly polarised at 45° to the pump and the analyser was in the crossed position. The Rabi frequencies were : theoretical 30 MHz, experimental 28 MHz. The small vertical tic marks on the baseline of each profile indicate the position of zero probe laser detuning. The longer lines from each baseline to the profile indicate the positions of equal pump and probe detuning.

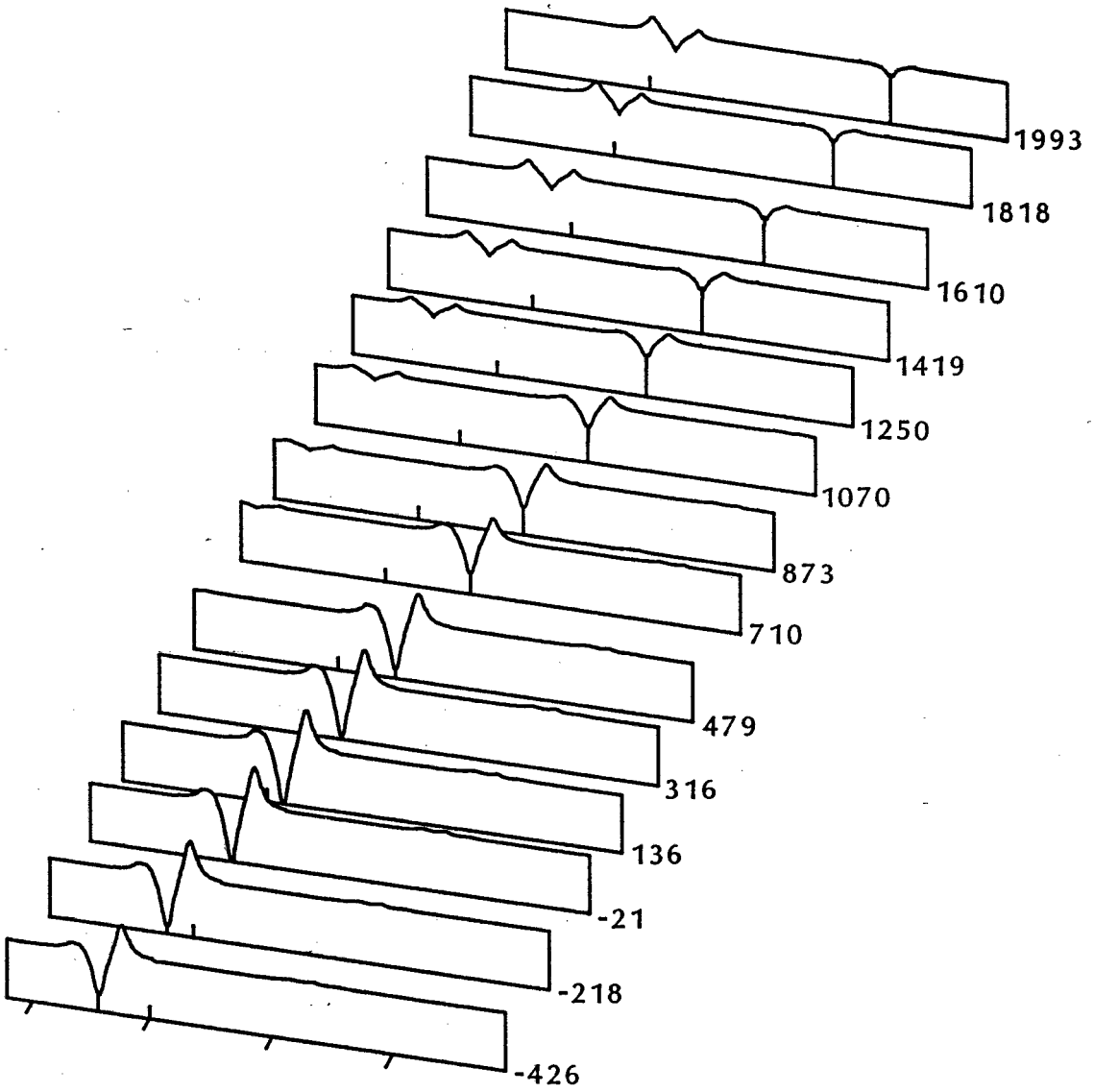
1993
1818
1610
1419
1250
1070
873
710
479
316
136
-21
-218
-426

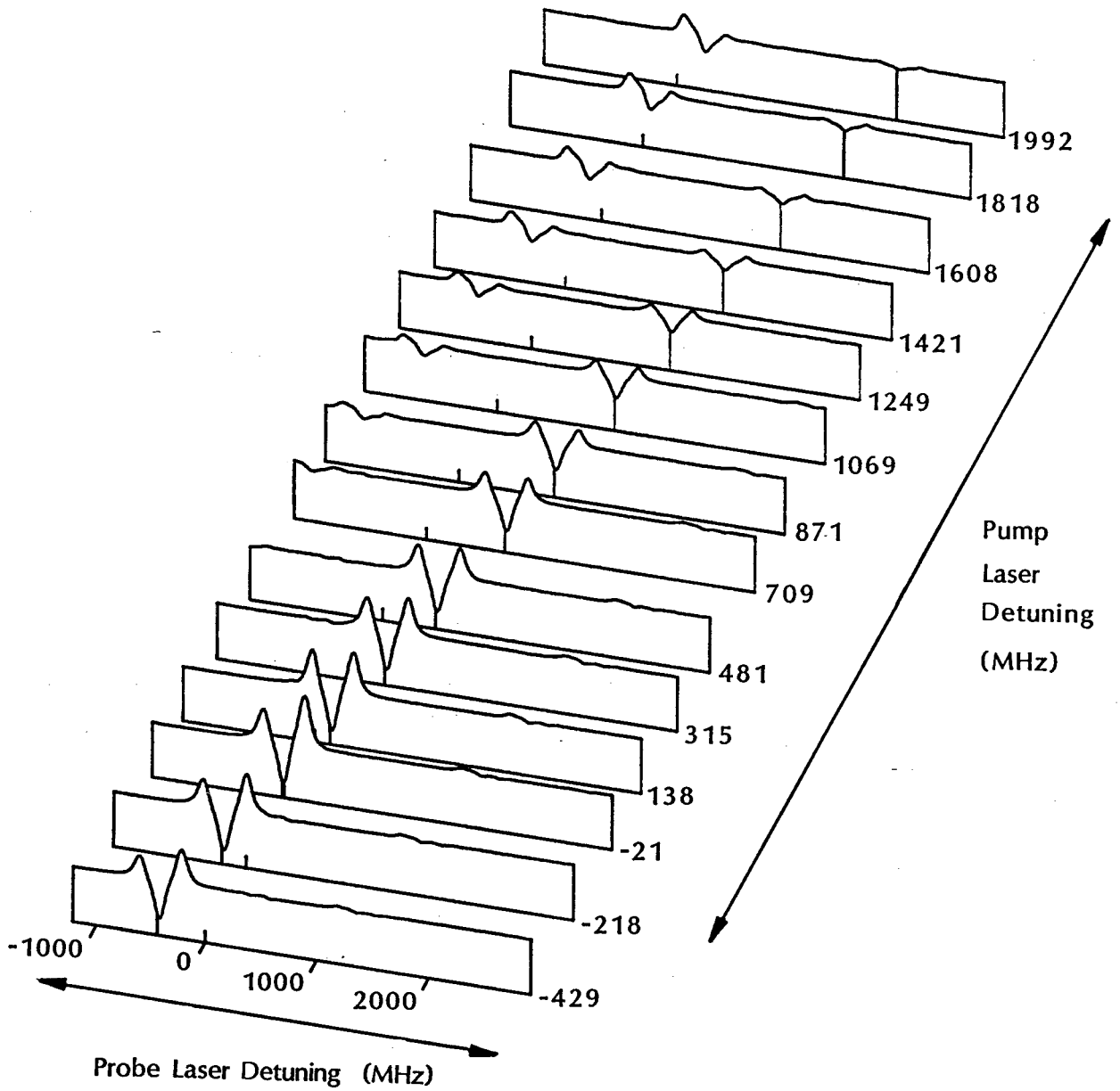

Figure 5.4 Comparison of theory (overlay sheet) and experiment for co-propagating polarisation spectroscopy: linearly polarised pump. The probe was linearly polarised at 45° to the pump and the analyser was rotated by 2.5° from the crossed position. The Rabi frequencies were : theoretical 30 MHz, experimental 28 MHz. The small vertical tic marks on the baseline of each profile indicate the position of zero probe laser detuning. The longer lines from each baseline to the profile indicate the positions of equal pump and probe detuning.

Chapter 6. Conclusion

To conclude, the validity of the theoretical treatment will be considered in the light of the experimental and theoretical material presented in the bulk of the thesis. Before doing so, the material will be summarised and some important points discussed.

6.1 Summary of the work

Good agreement between theoretical and experimental profiles is shown in Chapter 5. The positioning of features in the Doppler broadened profiles was correctly predicted. In addition, the amplitudes and signs of the features and the power broadening were reproduced by the theory.

Some discrepancies, principally at higher pump Rabi frequencies, were of course found. These could, at least in part, be due to incorrectly chosen Rabi frequencies. Because the quadratic term in the signal is used, no optimisation of the Rabi frequency is possible for polarisation spectroscopy profiles. Although it can be done in the case of saturated absorption, individual peaks are not resolved because of power broadening at high pump Rabi frequencies. It is therefore difficult to optimise the fit by adjusting the relative sizes of peaks. At lower intensities, the agreement between theory and experiment was substantially better.

The theoretical treatment allows only a single probe interaction during the evolution of the density matrix. This was identified as a possible source of discrepancy if the optical depth of the medium is too high. Changes in the probe polarisation due to an interaction early in the propagation alter the field driving the evolution at later stages, whereas the calculations are carried out assuming the initial probe polarisation. Because the polarisation of the field is important in this mechanism, only polarisation spectroscopy profiles are affected.

These propagation effects could, in principle, be included in the theoretical calculation. However, this would entail a significant increase in computer time and was not attempted. They could also be investigated experimentally by varying the number density of the medium, although large reductions from the densities used here would cause a deteriorating signal to noise ratio.

A major assumption made in the development of the theoretical treatment was the steady state assumption, and this assumption was shown to be violated in the experiment. The duration of the interaction between the atoms and fields is determined by the time taken for the atoms to propagate through the laser fields. Since the only decay mechanism for lower level populations and coherences is the propagation of atoms out of the interaction region, lower level relaxation cannot be involved in the evolution of these quantities. Because evolution to the steady state would be expected to

take several relaxation times, lower level coherences and populations cannot be assumed to reach the steady state during the interaction time. Thus the steady state assumption is violated.

It is difficult to assess the influence of this assumption on the agreement between theory and experiment. Lower level relaxation was included in the theoretical model and a value consistent with the transit time was used. By varying the focus size of the laser beams, it would be possible to investigate the influence of the transit time on the experimental results. However, reliable theoretical calculations of this variation could only be gained by using a different solution technique.

Theoretical considerations of the mechanism for generating the signal in a polarisation spectroscopy experiment show the importance of the number density of the medium in determining the relative contributions of the quadratic and linear terms to the signal. This raises the possibility of using polarisation spectroscopy to measure the number density since the two terms can be readily distinguished experimentally. Fig. 3.9, for example, shows that they have opposite sign if the analyser is rotated in the positive direction. It should be possible, using minimal pump intensities and therefore a simplified theory, to calculate the number density from the variation of the profile with analyser orientation.

6.2 Conclusions drawn

The reasonable agreement between theory and experiment demonstrated in Chapter 5 shows that it is possible to model the non-linear interaction between an atom with an extended level system and radiation fields. The additional complication of the Doppler effect can also be treated. The degree of agreement is sufficient to show that the most important physical mechanisms have been included in the theory.

The solution of the Liouville equation was found in terms of an expression involving operators in Liouville space. After choosing an appropriate basis for the extended level system, this expression was reduced to a matrix equation that was evaluated by computer. By making as much use as possible of the symmetries in the matrices, an efficient computer solution was written.

Although this theoretical technique has the advantage of allowing an efficient calculation for the extended level system, it suffers from the disadvantage that the influence of the violated steady state assumption is difficult to determine. However, since the agreement with experiment is reasonable, it does not appear to have a major effect.

The Doppler effect imposed some substantial additional computational difficulties. Since the Doppler free calculations were done entirely by computer, it was not possible to perform the Doppler integration analytically.

The Fourier transform technique devised to evaluate the Doppler integral was quite efficient, but it required extremely large amounts of storage. This was due to the large Doppler width (which determined the range of pump and probe detunings required) relative to the widths of Doppler free features (which determined the sampling frequency required). The sampling frequency used was a compromise between the conflicting requirements of minimising virtual memory and disc storage space and obtaining the best numerical representation of the Doppler free solution.

Although the system can be modelled reasonably accurately, the CPU time and disc storage figures quoted in Appendix C show that the numerical calculations are only marginally feasible within the computing facilities available to an average user. This means that optimisation of various parameters is not possible. Consequently, it is not possible to distinguish between inherent limitations in the model and inaccurately chosen parameters as the source of discrepancies in the theoretical calculations.

In contrast, the Doppler free calculations (the results of which have not been presented here) are efficient and require reasonable disc storage. There is a wealth of interesting effects in the Doppler free profiles. The effects of optical pumping can be readily seen in the variation of the amplitudes of features with pump laser Rabi frequency at the lower end of the range. At higher Rabi frequencies, A.C. Stark splitting occurs. The presence of

"I system", "V system", "Λ system" and "N system" resonances with various degrees of Zeeman degeneracy allows the influence of these complications on the splitting to be investigated.

Similarly, Doppler free experimental investigations of the same transition would be worthwhile. Using the smaller interaction region of an atomic beam would reduce the range of Rabi frequencies due to the Gaussian intensity profile of the laser beams. With atomic motion restricted to being perpendicular to the laser beams (and possibly incorporating velocity selection), the influence of the interaction time could be studied by varying the diameter of the laser beams.

To summarise this work, it can be stated that despite some small limitations on the agreement between theory and experiment, the ability to model the non-linear interaction of an extended Doppler broadened atomic system with radiation fields has been demonstrated. However, the potential exists for some interesting work with a Doppler free experiment and the theoretical treatment developed here.

Appendix A. Experimental Details

The sodium atoms were prepared in a heated ultra-high vacuum cell with a separately heated sidearm containing a small quantity of sodium. Figure A.1 shows details of the sodium cell and the heating. The main cell was a stainless steel cylinder 10 cm in diameter and 10 cm in length. Conflat flanges were used for vacuum seals to the turbo-molecular pump, the sidearm and an ionisation gauge (not shown in Fig. A.1), while Viton O-rings were used for the window vacuum seals. The heating for the main cell was provided by a hot oil bath sealed onto the vacuum cell with a silicone rubber compound. The oil bath was constructed as a cylinder in two halves to allow it to be sealed onto the ports of the main cell. Removable end plates were sealed onto the window clamping tubes with Viton O-rings. Five heating elements, made from bifilar windings, immersed in the oil dissipated approximately 240 W to heat the cell to approximately 200°C. The clamps for the main cell windows were also in contact with the oil, keeping the windows hot. The windows were therefore kept free of sodium condensation without using a buffer gas in the cell.

The sodium was contained in a small side arm to the main cell. A separate heating circuit, again using bifilar windings was used to heat this side arm to approximately 180°C. Since the sidearm was cooler than the cell walls, the sodium density was determined by the temperature of the arm. The background pressure in the cell was maintained at

10^{-6} Torr while the cell was at operating temperature.

A set of three Helmholtz coils surrounded the main cell and heating bath and were used to cancel stray magnetic fields inside the cell. Constant current power supplies with sufficient current resolution were not available, so constant voltage supplies were substituted. The current flowing through each coil was measured from the voltage drop across a standard resistor in series with each coil. The resistances were low enough to avoid heating of the resistor by the power dissipated by the current. By monitoring the voltage across these resistors it was possible to ensure that the current through the coils was constant during a set of laser scans.

The current through the coils was set using a fluxgate magnetometer to measure the magnetic field inside the cell. It was possible to reduce the fields over a cubic region of approximately 3 cm x 3 cm x 3 cm to 1 mG, and the field over the whole region of interaction of the two laser beams could be reduced to less than 10 mG (including the residual effects of the heating elements).

A separate high vacuum chamber for the polarising optics was sealed onto the main cell and evacuated to 10^{-2} Torr using a backing pump. The polarisers were mounted in rotatable sections of the chamber. Angular position adjustment of the polarisers was provided by lever arms attached to the rotatable sections. A fine thread screw was used to move each arm relative to a fixed mounting plate. On

the section holding the probe beam analyser, the screw was replaced by a micrometer. The relationship between angle and micrometer reading was derived from the geometry of the system. With this arrangement it was possible to measure the angular position of the analyser to within ±0.1 degrees. Two small right angle prisms were used to reflect the laser beams from the side entry windows into the main cell.

The pump and probe laser fields were produced by commercial cw dye lasers (Coherent 699-21 and Spectra Physics 380D). Active stabilisation ensured that the frequency jitter of the lasers was less than 3 MHz, which is sufficiently small compared with the natural width of the sodium D_1 transition (10 MHz) to cause little degradation to the resolution of the experiment.

The laser beams were both focussed to a waist in the centre of the vacuum cell. The pump beam waist was larger than the probe, in an attempt to reduce the variation in pump intensity over the region of interaction between the two beams. The beams were as close to overlapping as possible while maintaining a spatial separation at the prisms. Because the probe laser was very weak, it was necessary to use a photomultiplier tube to measure its intensity after passing through the analyser. The pump laser was more intense so a spatial filter was placed in front of the photomultiplier to reduce the effects of scattered pump radiation. The intensity of the pump beam was stabilised using a feedback circuit driving an electro-optic modulator,

and the pump intensity was recorded from the photodiode in the electronics (Channel 1, Figure 2.2). The intensity of the probe laser was recorded (Channel 4, Figure 2.2) from a signal provided by the control electronics of the probe laser.

A secondary saturated absorption experiment was set up to allow the frequencies of both beams to be recorded during a scan. After the probe beam for the primary experiment had been separated from the output of the laser, the rest of the beam was divided into a pump and probe beam for a standard saturated absorption experiment in a small glass sodium cell. During a scan of the probe frequency, this saturated absorption signal (Channel 3, Figure 2.2) was recorded simultaneously with the primary signal. The resolution of this secondary experiment (limited by pressure broadening and velocity changing collisions inside the glass cell) was sufficient to resolve the excited state hyperfine structure.

Subsidiary beams were derived from both the pump and probe lasers and mixed on a high speed photodiode, producing a beat signal. The beat was amplified by a radio frequency amplifier tuned to 30 MHz, producing a strong signal whenever the separation of the two laser frequencies was 30 MHz. This signal was also recorded during probe laser frequency scans (Channel 5, Figure 2.2), resulting in two narrow peaks equally spaced about the pump laser frequency. Using these two auxiliary experiments it was possible to measure both pump and probe frequencies during a scan to within 10 MHz.

In addition, a 300 MHz free spectral range etalon was used to produce regularly spaced peaks during the probe frequency scan as a frequency calibration (Channel 0, Figure 2.2).

The pump beam was chopped at approximately 800 Hz with a mechanical chopper and the probe intensity signal was processed with a lock-in amplifier. This ensured that the linear Doppler-broadened absorption of the probe beam by the sodium vapour was not recorded.

All six signals of interest were recorded by a six-channel analogue to digital convertor system controlled by a micro-computer. The computer also synchronised the laser scans and the data storage process. A typical series of measurements involved a probe laser frequency scan of 100 seconds duration for each of a number of different pump laser detunings, with 1000 ADC cycles for each channel during each scan.

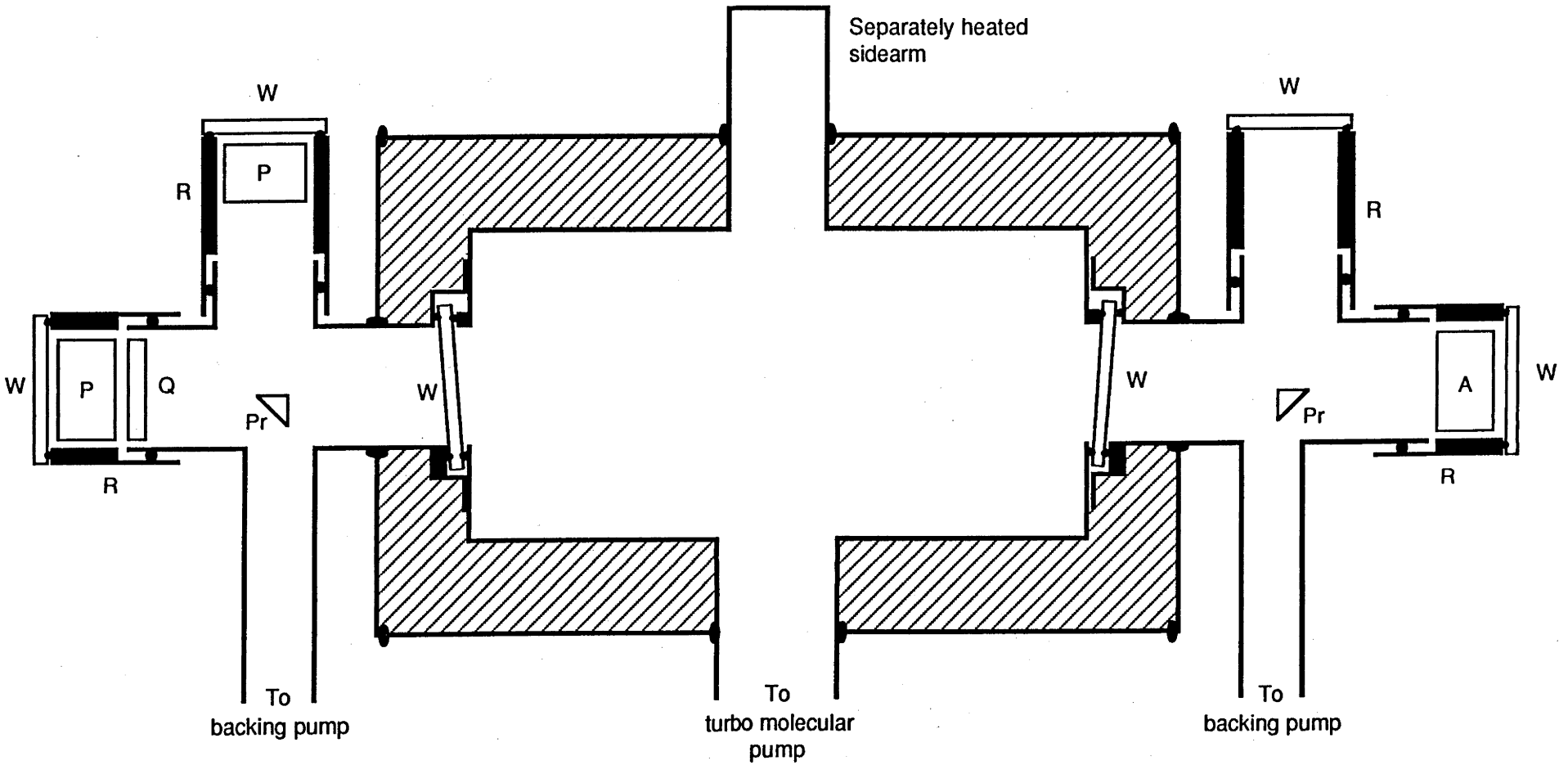

Figure A.1 Schematic diagram of the sodium cell. A cross section through the sodium cell, the oil heating bath (shaded region) and the polariser vacuum compartment is shown. O-ring seals are shown as round dots and silicone rubber seals are shown as black ellipses. Abbreviations used: W, window; P, polariser; Q, quarter-wave plate; Pr, prism; R, rotatable section; A, analyser.

Appendix B. The Interaction Operator and the Dipole Vector

Expressions for the matrix elements of the interaction operators, U_η, in the irreducible tensor representation are derived in this appendix. The vector representing the electric dipole is also derived.

B.1 Matrix elements of the interaction operator

U is related to the interaction Hamiltonian, H_i, (Eq. 4.9) in Hilbert space by

$$\begin{aligned} U|X>> &= \hbar^{-1} \left[H_i, X\right] \\ &= \frac{-1}{2\hbar} \left[\underset{\sim}{\mu}, X\right] . \sum_\eta \left(\underset{\sim}{E}_\eta^{(+)} + \underset{\sim}{E}_\eta^{(-)}\right) \end{aligned} \tag{B.1}$$

where the complex exponential parts of the fields have been omitted. It has already been shown that the interaction operator, U_η, causes a change of ± 1 unit in n_η, the harmonics number corresponding to field η. It is not necessary to consider the field part of the interaction operator further since the effect on the harmonics number basis is a complete description of the time dependent field part. Equation B.1 represents the atomic part of the interaction operator. For the purpose of evaluating matrix elements of U, the Liouville space irreducible tensor basis elements will be substituted for the ket $|X>>$.

The field amplitude vectors must be retained in the atomic part of the interaction operator because the field polarisations determine the Zeeman transitions that are excited. The amplitudes are incorporated into the Rabi frequency and determine the strength of the interaction.

To evaluate the matrix elements of U, the definition of the irreducible tensor elements (Eq. 4.27) is first used to express the commutator bracket in terms of matrix elements of the dipole operator on the Zeeman basis, $|i,m_i>$, in Hilbert space. Expanding the electric dipole vector in terms of the spherical basis vectors (Eq. 4.28) and applying the Wigner-Eckart theorem, all dependence on the angular momentum projection quantum number, m, is expressed by Clebsch-Gordan coefficients.

$$<xm_x|\underset{\sim}{\mu}|ym_y> = \sum_q <xm_x|\mu_q|ym_y> \underset{\sim}{e}^*_q$$
$$= \frac{<x\|\mu\|y>}{(2F_x+1)^{1/2}} \sum_q <F_y,1,m_y,q|F_x,m_x> \underset{\sim}{e}^*_q \qquad (B.2)$$

where $<x\|\mu\|y> = \mu_{xy}$ is a reduced matrix element of the dipole operator.

The inverse of Eq. 4.27 is then used to convert the expression back to the irreducible tensor basis.

The next step is to evaluate the dot product of the resulting vector with the electric field vector. Separation of the field into positive and negative frequency parts does not fix the phase of the field. Since the phase of the field is arbitrary, the positive frequency component, $\underset{\sim}{E}_\eta^{(+)}$, can be chosen to be real. Since the negative frequency part is the complex conjugate of $\underset{\sim}{E}_\eta^{(+)}$, the two components are equal and will be designated $\underset{\sim}{E}_\eta$. The field vector is expanded on the spherical basis and the dot product with the $\underset{\sim}{e}_q^*$ from Eq. B.2 is taken.

$$\underset{\sim}{E}_\eta \cdot \underset{\sim}{e}_q^* = \left(E_\eta \sum_p \varepsilon_p^{(\eta)} \underset{\sim}{e}_p^*\right) \cdot \underset{\sim}{e}_q^* = (-1)^q E_\eta \, \varepsilon_{-q}^{(\eta)} \qquad (B.3)$$

where the field has been separated into an amplitude, E_η, and a unit "polarisation vector", $\underset{\sim}{\varepsilon}^{(\eta)}$.

Combining Eq. B.3 with the expression for the commutator bracket in the irreducible tensor representation gives the action of the operator U_η on an element of the irreducible tensor basis. Taking the inner product with another element of the basis gives a matrix element of the operator.

$$\begin{aligned} \langle\langle if^\dagger; K', Q' | U_\eta | kg^\dagger; K, Q \rangle\rangle = {} & S(F_k, F_g, F_f, K, K', Q, Q') \frac{\mu_{gf} E_\eta}{\hbar} \varepsilon^{(\eta)}_{Q-Q'} \delta_{ki} \\ & - S(F_g, F_k, F_i, K, K', Q, Q') \frac{\mu_{ik} E_\eta}{\hbar} \varepsilon^{(\eta)}_{Q-Q'} \delta_{fg} \end{aligned} \qquad (B.4)$$

The combinations of Clebsch-Gordan coefficients have been absorbed into the scaling functions S. These functions can

be concisely written in terms of a six-j symbol

$$S(F_x,F_y,F_z,K,K',Q,Q') = (-1)^{K}(-1)^{Q-Q'}(-1)^{F_x+F_y}(2K'+1)^{1/2} <1,K',Q'-Q,-Q'|K,-Q> \begin{Bmatrix} 1 & K' & K \\ F_x & F_y & F_z \end{Bmatrix} \quad (B.5)$$

The scaling functions express the influence of Zeeman degeneracy (through the irreducible tensor components K and Q) on the interaction operator. In a similar fashion, it is possible to separate the influence of hyperfine structure out of the reduced matrix element of the dipole operator. Since the nuclear and electronic angular momenta (I and J respectively) are coupled to form the total angular momentum, F, of the levels of the hyperfine structure, Sobel'man's treatment (Sobel'man 1972, Section 14.5) of reduced matrix elements can be applied. The reduced matrix elements in Eq. B.4 become part of a "scaled Rabi frequency", $\beta_{xy}^{(\eta)}$

$$\beta_{xy}^{(\eta)} = \hbar^{-1}\mu_{xy}E_{\eta} = -\hbar^{-1}(-1)^{J_x+I+F_y}(2F_x+1)^{1/2}(2F_y+1)^{1/2}\begin{Bmatrix} 1 & F_y & F_x \\ I & J_x & J_y \end{Bmatrix} <J_x\|\mu\|J_y>E_{\eta} \quad (B.6)$$

All levels involved in the D_1 transition of sodium have the same electronic angular momentum quantum number, J. It is therefore possible to define a "reduced Rabi frequency" $\beta_{xy}^{(\eta)}$

$$\beta_{xy}^{(\eta)} = \hbar^{-1}\langle J_x \| \mu \| J_y \rangle E_\eta \qquad (B.7)$$

which is determined only by the amplitude of the field and the strength of the D_1 transition. This parameter is therefore equivalent to the Rabi frequency quoted in Chapter 1 for two state systems.

B.2 The electric dipole vector

The representation of the electric dipole bra, $\langle\langle \underset{\sim}{\mu} |$, is derived in a fashion similar to the interaction operator matrix elements. It is first expanded in terms of Liouville space basis vectors

$$\langle\langle \underset{\sim}{\mu} | = \sum_{x,y,K,Q} \langle\langle \underset{\sim}{\mu} | xy^\dagger;K,Q \rangle\rangle \langle\langle xy^\dagger;K,Q | \qquad (B.8)$$

and the irreducible tensor vectors are then converted back to the Zeeman basis, $|x,m_x(y,m_y)^\dagger\rangle\rangle$. The permutation property of the trace in the definition of the Liouville space inner product (Eq. 4.3) is used to express the coefficients in the expansion in terms of matrix elements of the Hilbert space dipole operator. The Wigner-Eckart theorem is then applied.

The resulting expansion is given by

$$\langle\langle \underset{\sim}{\mu} | = \frac{1}{\sqrt{3}} \sum_{x,y,Q} (-1)^{F_y - F_x} \mu_{yx} \underset{\sim}{e}_Q \langle\langle xy^\dagger; 1, Q | \qquad (B.9)$$

where μ_{yx} is a reduced matrix element of the dipole operator and could be rescaled to account for hyperfine structure as described above.

Equation B.9 shows that $\langle\langle \underset{\sim}{\mu} |$ is both a Liouville space state and a vector. Once expressed in this form it is a simple matter to calculate the Liouville space inner product with the density matrix (Eq. 4.23) to evaluate the atomic polarisation induced by the laser fields.

In order correctly to scale the signal field that is calculated from the atomic polarisation, the reduced dipole matrix element must be calculated in appropriate units. This can be done by expressing it in terms of the upper level lifetime of the transition, a quantity which is well known. From the expression for the Einstein A coefficients in terms of the dipole operator (see, for example, Corney 1977, Chap. 4.5), the upper level lifetime can be obtained.

$$\tau_u^{-1} = \frac{2}{9} \frac{\omega^3}{\varepsilon_0 h c^3} \langle J_u \| \mu \| J_l \rangle^2 \sum_l (2F_l + 1) \begin{Bmatrix} 1 & F_l & F_u \\ I & J_u & J_l \end{Bmatrix}^2 \qquad (B.10)$$

where subscripts u and l indicate upper and lower levels respectively. The weighted sum over the lower level of six-j

symbols has the value 1/2 for the D_1 transition of sodium. Since the two upper level lifetimes are equal, Eq. B.10 can be used to derive the reduced matrix element in the dipole vector (Eq. B.9). This is not necessary in the matrix elements of the interaction operator since the dipole moment is incorporated into the reduced Rabi frequency.

Appendix C. Computer Programme

This appendix describes the computer programmes that were written to implement the theoretical treatment given in Chapter 4. Special attention is paid to the symmetries that were used to enhance the speed of the calculations. Section C.1 is devoted to the calculation of the Doppler free signal field, while Section C.2 describes the programme that calculated the Doppler broadened signal.

Because the computer calculations were an integral part of the theoretical solution and comparison with experimental results, performance figures are given for the programmes. If the computer time requirements are considered to be prohibitive, the model cannot be considered a satisfactory description of the extended level system since it is difficult to predict the results without the computer calculations. The figures given show that, although they are acceptable, the Doppler broadening calculations place severe demands on computing resources.

C.1 Doppler free calculation

The solution of the Liouville equation derived in Chapter 4 gives a simple expression for the component of the density matrix oscillating at the probe frequency (Eq. 4.22). Despite the simplicity of this equation, it is a major computational task to evaluate it efficiently. This is because the components of the equation are large matrices representing operators on the Liouville space basis. In

order to optimise the execution speed of the programme, symmetries inherent in the operators were used to minimise the amount of calculation required.

Expressions for the matrix elements of the operators were given in Chapter 4. The combined atomic and harmonics number Liouville space was divided into even and odd parts as described in Chapter 4. The Green's function operators, $G(\underset{\sim}{n}.\underset{\sim}{\omega})$, are restricted to one of the two sub-spaces while the interaction operators, U_{η}, transfer a Liouville space state from one sub-space to the other. Thus the size of a Green's function matrix is restricted to the number of basis vectors in the appropriate sub-space. Similarly, the U operators are implemented as non-square matrices of appropriate dimensions.

Selection rules manifest in the definition of the matrix elements of the interaction operator (Eqs. 4.33, 4.34 and 4.35) can be used to determine which elements are zero. These elements need not be calculated. The six-j symbol in the scaling function S (Eq. 4.34) restricts the change in the K index of the irreducible tensor representation, while the Q index is restricted by the element of the polarisation vector in Eq. 4.33. In the case of a π polarised field, the Q index does not change and, since the entire interaction starts with the equilibrium density matrix, Q is zero for all components of the density matrix. The sizes of the matrices can thus be further reduced in this case.

To calculate a profile, the programme performs a loop over the probe detuning, repeatedly calculating the signal field. Since the interaction operator is independent of detuning, the U matrix is calculated outside this loop. The detuning dependence of the evolution is contained in the Green's functions. By using symmetries in the interaction operator and the diagonal nature of odd Green's functions, it is also possible to do a significant proportion of the calculation of UGU terms outside the probe detuning loop.

Figure 4.2 shows that the X units in the density matrix are independent of probe detuning since $n_1 = 0$ in all Green's functions of the lower path. This matrix is also calculated outside the probe detuning loop. Although it must be recalculated for each pump detuning, the simplifications to the calculation of UGU terms may again be applied.

The final simplification used takes advantage of the restricted range of the Q index necessary for the inner product with the dipole vector in calculating the atomic polarisation (Eq. 4.23). Because the dipole is a vector, Eq. 4.36 shows that only $|Q| \leq 1$ Liouville space elements of the density matrix are necessary. Along with the resonance condition applied to the Green's function at the left hand end of the diagram, this restricts the elements that are necessary in the final multiplication by an interaction operator in each path of the diagram.

The Doppler free version of the programme calculates the signal field as a function of probe detuning for a number of different pump detunings using the above simplifications. The signal is derived from the signal field according to Equation 4.40 (ignoring the "D" superscripts) and stored for later examination. This programme thus calculates the signal expected in a Doppler-free experiment, taking 13 seconds of CPU time on a VAX 8700 mainframe for 120 values of probe detuning with a π polarised pump beam. For a σ polarised pump beam it requires 60 seconds.

C.2 Doppler broadened calculation

As described in Chapter 4, the Doppler free signal field is converted to the Doppler broadened field using a Fourier transform technique (Eq. 4.37). Because a two dimensional fast Fourier transform is used, it is necessary that the Doppler free signal field be calculated over a two dimensional sampling grid of pump and probe detunings. A version of the Doppler free programme described above was written to calculate and store the field over this range.

The sampling frequency required was determined by the widths of features in the Doppler free signal field. It is necessary to use a frequency higher than the Nyquist frequency in order to obtain a reasonable discreet representation of the function.

In order to avoid edge effects in the calculation of the convolution (Eq. 4.37), the field must be known over detuning ranges of the order of the Doppler width. However, it was not necessary to calculate the signal field over this large region because it approaches the linear response to the probe field at large pump laser detunings. The signal field was therefore only calculated over four smaller regions in the vicinity of the Doppler free resonances. The linear response at large pump detunings was treated analytically.

The four data sets were combined into one extended two dimensional array for the Fourier transform calculations. However, before this was done, the effect of the analyser was calculated. Calculation of the Doppler broadened signal field would have entailed two dimensional Fourier transforms of a complex vector, resulting in unrealistic disc storage requirements for the input and output data. Since the polarisation of the field transmitted by the analyser is constant, the data set can be reduced to a complex scalar (i.e. the amplitude of the transmitted field) if the effect of the analyser is included first.

Because of the large number of pump detunings needed for the two dimensional sampling grid, the CPU time requirements for the Doppler broadened calculations were substantially greater than for the Doppler free case. Calculation of the signal field over the four limited regions of pump and probe detuning required two hours of CPU time for a π polarised pump field. This figure would have been increased to eight

hours for the σ polarised case.

The Doppler broadening calculations were much less expensive however, requiring eight minutes of processor time. However, if all data was stored, the size of the output data file was four megabytes, which is 80% of the disc space allocation for a normal user at this site. The programme required eight megabytes of virtual memory which is twice the standard allocation.

Comparisons of theory and experiment such as those presented in Chapter 5 use only the portion of the calculated data corresponding to the pump detunings used in the experiment. Although this means that most of the data is not used in the comparison, it must still be calculated in order to do the Fourier transforms. Despite this apparent inefficiency, the Fourier transform technique was found to be many times faster than a numerical integration method tried earlier.

References

Agarwal 1979 Phys. Rev. A 19 923

Aminoff, Javanainen and Kaivola 1983 Phys. Rev. A 28 722

Anderson, Lawler, Anderson, Holley and Filippelli 1978 Phys. Rev. A 17 2099

Autler and Townes 1955 Phys. Rev. 100 703

Baklanov and Chebotaev 1971 Sov. Phys. JETP 33 300

Baklanov and Chebotaev 1972 Sov. Phys. JETP 34 490

Ben-Reuven 1966 Phys. Rev. 141 34

Ben-Reuven and Klein 1971 Phys. Rev. A 4 753

Borde, Hall, Kunasz and Hummer 1976 Phys. Rev. A 14 236

Boyd and Mukamel 1984 Phys. Rev. A 29 1973

Cahuzac and Vetter 1976 Phys. Rev. A 14 270

Carmichael and Walls 1976 J. Phys. B. 9 1199

Cohen-Tannoudji 1975 in "Proceedings of the Second International Conference on Laser Spectroscopy" edited by Haroche, Pebay-Peyroula, Hansch and Harris, Springer-Verlag Berlin.

Cohen-Tannoudji and Reynaud 1977a J. Phys. B 10 345

Cohen-Tannoudji and Reynaud 1977b J. Physique Lett. 38 L173

Colomb and Dumont 1977 Opt. Comm. 21 143

Cooper, Ballagh and Burnett 1980 Phys. Rev. A 22 535

Corney 1977 "Atomic and Laser Spectroscopy" Clarendon, Oxford

Dalton 1982 J. Phys. A 15 2157

Delsart and Keller 1976 J. Phys. B 9 2769

Delsart and Keller 1977 in "Proceedings of the Third International Conference on Laser Spectroscopy" edited by Hall and Carlsten, Springer-Verlag, Berlin.

Delsart and Keller 1978a J. Physique 39 350

Delsart and Keller 1978b J. Appl. Phys. 49 3662

Delsart and Keller 1980 J. Phys. B 13 241

Delsart, Keller and Kaftandjian 1981 J. Physique 42 529

Dienes 1968a Phys. Rev. 174 400

Dienes 1968b Phys. Rev. 174 414

Ducloy 1973 Phys. Rev. A 8 1844

Ducloy and Dumont 1970 J. Physique 31 419

Feld and Javan 1969 Phys. Rev. 177 540

Feldman and Feld 1970 Phys. Rev. A 1 1375

Feneuille and Schweighofer 1975 J. Physique 36 781

Feuillade and Berman 1984 Phys. Rev. A 29 1236

Fisk 1985 "The Dynamic Stark Effect in a J=0→1→0 Three Level System" Ph.D. Thesis, ANU, unpublished.

Fisk, Bachor and Sandeman 1986a Phys. Rev. A 33 2418

Fisk, Bachor and Sandeman 1986b Phys. Rev. A 33 2424

Fisk, Bachor and Sandeman 1986c Phys. Rev. A 34 4762

Gawlik and Series 1979 in "Proceedings of the Fourth International Conference on Laser Spectroscopy" edited by Walther and Rothe, Springer-Verlag, Berlin

Gray and Stroud 1978 Opt. Comm. 25 359

Grove, Wu and Ezekiel 1977 Phys. Rev. A 15 227

Haken 1981 "Light Volume I: Waves, Photons, Atoms" North-Holland, Amsterdam

Hansch and Toschek 1970 Z. Physik 236 213

Haroche and Hartman 1972 Phys. Rev. A 6 1280

Hartig, Rasmussen, Schieder and Walther 1976 Z. Physik A 278 205

Hassan and Bullough 1975 J. Phys. B. 8 L147

Hecht and Zajac 1974 "Optics" Addison-Wesley, Reading

Holt 1972 Phys. Rev. Letts. 29 1138

Kaftandjian, Talin and Klein 1979 J. Physique 40 1037

Keller and Delsart 1977 Opt. Comm. 20 147

Khosrofian and Garetz 1983 Appl. Opt. 22 3406

Kimble and Mandel 1976 Phys. Rev. A 13 2123

Klein, Giraud and Ben-Reuven 1974 Phys. Rev. A 10 682

Kogelnik and Li 1966 Appl. Opt. 5 1550

Levenson 1982 "Introduction to Nonlinear Laser Spectroscopy" Academic Press, New York

Letokhov 1976 in "High Resolution Laser Spectroscopy" edited by Shimoda, Springer-Verlag, Berlin.

Messiah 1961 "Quantum Mechanics" vols. I and II, North Holland, Amsterdam.

Mollow 1969 Phys. Rev. 188 1969

Mollow 1970 Phys. Rev. A 2 76

Mollow 1972a Phys. Rev. A 5 1522

Mollow 1972b Phys. Rev. A 5 2217

Murnick, Feld, Burns, Kuhl and Pappas 1979 in "Proceedings of the Fourth International Conference on Laser Spectroscopy" edited by Walther and Rothe, Springer-Verlag, Berlin.

Nakayama 1981a J. Phys. Soc. Jpn. 50 606

Nakayama 1981b J. Phys. Soc, Jpn. 50 609

Nakayama 1984a J. Phys. Soc. Jpn. 53 3351

Nakayama 1984b Opt. Comm. 50 19

Nakayama 1985 J.O.S.A. B 2 1431

Nakayama, Series and Gawlick 1980 Opt. Comm. 34 382

Newstein 1968 Phys. Rev. 167 89

Omont 1977 Prog. Quantum Electron. 5 69

Pappas, Burns, Hinshelwood, Feld and Murnick 1980 Phys. Rev. A 21 1955

Picque and Pinard 1976 J. Phys. B 9 L77

Pinard, Aminoff and Laloe 1979 Phys. Rev. A 19 2366

Rabin and Ben-Reuven 1979 Phys. Rev. A 19 1697

Rinneberg, Huhle, Matthias and Timmermann 1980 Z. Physik A 295 17

Roach 1982 "Green's Functions" 2nd edition, Cambridge University Press, Cambridge.

Sargent 1976 Phys. Rev. A 14 524

Sargent, Toschek and Danielmeyer 1976a Appl. Phys. 11 55

Sargent and Toschek 1976b Appl. Phys. 11 107

Schabert, Keil and Toschek 1975a Opt. Comm. 13 265

Schabert, Keil and Toschek 1975b Appl. Phys. 6 181

Schlossberg and Javan 1966 Phys. Rev. 150 267

Schuda, Stroud and Hercher 1974 J. Phys. B 7 L198

Shirley 1973 Phys. Rev. A 8 347

Shore 1978 Phys. Rev. A 17 1739

Skribanowitz, Kelly and Feld 1972 Phys. Rev. A 6 2302

Smithers and Freedhoff 1975 J. Phys. B 8 2911

Sobel'man 1972 "Introduction to the Theory of Atomic Spectra" Pergamon, Oxford.

Stenholm and Lamb 1969 Phys. Rev. 181 618

Stert and Fischer 1978 Appl. Phys. 17 151

Stroud 1971 Phys. Rev. A 3 1044

Walther 1975, in "Proceedings of the Second International Conference on Laser Spectroscopy" edited by Haroche, Pebay-Peyroula, Hansch and Harris, Springer-Verlag, Berlin.

Whitley and Stroud 1976 Phys. Rev. A 14 1498

Wieman and Hansch 1976 Phys. Rev. Letts. 36 1170

Wu, Ezekiel, Ducloy and Mollow 1977 Phys. Rev. Letts. 38 1077

Wu, Grove and Ezekiel 1975 Phys. Rev. Letts. 35 1426